TECHNISCHE UNIVERSITÄT MÜNCHEN

MAX-PLANCK-GESELLSCHAFT

TECHNICAL UNIVERSITY OF MUNICH &
MAX PLANCK INSTITUTE OF PSYCHIATRY

Simultaneous Functional Magnetic Resonance Imaging and Electrophysiological Recordings: Practical Application And Methodological Approach

Dissertation
by
Kátia C. Andrade

[2011]

[This work was financially supported by the Capes Foundation, Ministry of Education of Brazil, Caixa Postal 365, Brasília – DF 70359-970, Brazil]

CAPES

TECHNISCHE UNIVERSITÄT MÜNCHEN

Physik Department E18

Simultaneous Functional Magnetic Resonance Imaging And Electrophysiological Recordings: Practical Application And Methodological Approach

Katia Cristine Andrade

Vollständiger Abdruck der von der
Fakultät für Physik der Technischen Universität München
zur Erlangung des akademischen Grades eines

Doktors der Naturwissenschaften (Dr. rer. nat.)
genehmigten Dissertation.

Vorsitzender: Univ.-Prof. Dr. J. Leo van Hemmen
Prüfer der Dissertation:
1. Univ.-Prof. Dr. Stephan Paul
2. apl. Prof. Dr. Sibylle Ziegler

Die Dissertation wurde am 02.03.2011 bei der Technischen Universität München eingreicht und durch die Fakultät für Physik am 21.03.2011 angenommen.

“So much sorrow and pain
Still I will not live in vain
Like good questions never asked
Is wisdom wasted on the past […]”

(Ben Harper-“Blessed to be a witness”)

CONTENTS

FIGURES

TABLES

LIST OF ABBREVIATIONS

AA	Amplitude analysis
ACC	Anterior cingulate cortex
ANOVA	Analysis of variance
AvgL	Average diagonal line
BCG	Ballistocardiogram artifact
BOLD	Blood oxygenation level dependent
CA	Cornu ammonis
CBF	Cerebral blood flow
CBV	Cerebral blood volume
$CMRO_2$	Cerebral metabolic rate of oxygen
CSF	Cerebrospinal fluid
DET	Determinism
DG	Dentate gyrus
DMN	“Default mode” network
EC	Entorhinal cortex
ECG	Electrocardiogram
EEG	Electroencephalography
emf	Electromotive force
EMG	Electromyogram
EOG	Electrooculogram
EPI	Echoplanar images
EPSP	Excitatory postsynaptic potential
ERP	Evoked related potential

FFT	Fast-Fourier transform
fMRI	Functional magnetic resonance imaging
FOV	Field of view
FWHM	Full width half maximum
GLM	General linear model
HF	Hippocampal formation
HRF	Hemodynamic response function
ICA	Independent component analysis
*i*ICA	Iterative independent component analysis
IPL	Inferior parietal lobule
ISI	Inter-stimulus interval
KC	K-complex
LAM	Laminarity
MaxL	Maximal diagonal line
MaxV	Maximal vertical line
MEG	Magnetoencephalography
MNI	Montreal neurological institute
mPFC	Medial prefrontal cortex
MR	Magnetic resonance
NMR	Nuclear magnetic resonance
NREM	Non rapid eye movement
PCC	Posterior cingulate cortex medial
PET	Positron emission tomography
PPI	Psychophysiological interactions
REM	Rapid eye movement

rf	Radiofrequency
rms	Root mean square
ROI	Region of interest
RP	Recurrence plot
RQA	Recurrence quantification analysis
RSNs	Resting-state networks
RspC	Retrosplenial cortex
S1	Sleep stage 1
S2	Sleep stage 2
SMA	Supplementary motor area
SPECT	Single-photon emission computed tomography
SPM	Statistical parametric mapping
SUB	Subiculum
SWS	Slow wave sleep
TE	Echo time
TR	Repetition time
TT	Trapping time
W	Wakefulness
WD	Wavelet denoising

ABSTRACT

The present work investigated two distinct analytical approaches to simultaneous EEG/fMRI data. In the first part, functional connectivity analysis was applied to simultaneous EEG/fMRI data to study cerebral networks and hemodynamic correlates of sleep specific EEG features as well as their functional significance during human sleep. In the second part, methodological aspects were addressed, evaluating the potential of a non-linear analysis method called recurrence quantification analysis (RQA) to extract rapidly changing dynamic features of electrophysiological data, which may be used to improve fMRI models of brain behaviour.

According to the standard model of memory consolidation, memory formation initially occurs in the hippocampus and the medial temporal lobe, where new experiences are temporarily stored. Long-term memory storage relies on off-line transfer to and consolidation in the neocortex. This information transfer between the hippocampus and the neocortex is believed to benefit from sleep. The goal of the first study was to determine spontaneous functional connectivity maps of subregions of the hippocampal formation (HF) with the rest of the brain in humans, and to evaluate their alteration throughout non rapid eye movement (NREM) sleep. We provided first evidence of changes in human hippocampal connectivity patterns from wakefulness to NREM sleep. The strongest functional connectivity between the HF, especially the subiculum output region, and neocortex was observed in sleep stage 2, while weakest connectivity was found in slow wave sleep. Increased connectivity between HF and neocortical regions in sleep stage 2 further appears associated to the presence of fast sleep spindle activity in concurrent electrophysiological recordings. This suggests an increased capacity for possible global information transfer, while

reduced long-range connectivity in slow-wave sleep may reflect a functional system optimal for segregated information reprocessing. Our data may be relevant to differentiating sleep stage specific contributions to neural plasticity as proposed in sleep dependent memory consolidation.

Simultaneous EEG/fMRI recording allow to combine the high EEG temporal resolution with the unmatched fMRI spatial resolution and the flexibility of fMRI to explore brain behaviour in various sensoric, cognitive and emotional paradigms. Today, analysis of event related potentials (ERP) is usually performed by an averaging of multiple EEG trials, in order to increase the signal-to-noise ratio. Thus, the temporal resolution of the EEG is partially lost, and averaging does not consider response changes across trials. This variability can, however, represent changes in subject's performance or fluctuations in attention, arousal, habituation or other cognitive features. In the second part of this thesis, we evaluated the potential of a nonlinear signal analysis method, recurrence quantification analysis (RQA), to improve the characterization of single trial EEG responses. This analysis showed that RQA is not significantly superior to conventional amplitude analysis. Despite equal discrimination power, RQA measures were only weakly correlated with ERP amplitudes, suggesting that additional information on single trials may be extracted by RQA. Therefore, RQA may be used as an additional tool to obtain new insights about the neurophysiology of the brain.

INTRODUCTION

Nowadays, the major techniques used to study functional brain activity are positron emission tomography (PET), single-photon emission computed tomography (SPECT), functional magnetic resonance imaging (fMRI), electroencephalography (EEG) and magnetoencephalography (MEG). EEG and MEG, different from the others, are based on electrophysiological instead of hemodynamic properties. FMRI has the advantage over PET and SPECT of a better spatial resolution in addition to the absence of potential risks associated with radioactive tracers. This allows repeated measures of brain activity across various task manipulations [1]. The fMRI temporal resolution, however, is still in the order of seconds while neuronal processes have a millisecond scale. The indirect relationship between fMRI and the neuronal electrical activity also raises the challenge of interpreting its findings [2;3]. EEG and MEG, on the other hand, have a high temporal resolution but lack spatial specificity. To overcome these limitations, many research groups attempt to combine techniques to complement each other. This is especially true for the combined use of hemodynamically based (fMRI) and electrophysiological (EEG) techniques [4]. Since physiological variables as vigilance, attention and anxiety cannot be fully reproduced in two independent sessions [5;6], the simultaneous use of EEG and fMRI has caught special attention in recent years [5;7-11].

The present work focus in two different lines of approaches to simultaneous EEG/fMRI data; therefore, the manuscript is divided in three chapters: The first chapter describes the technical basis and general principles of fMRI and EEG recordings and the challenges to combine these techniques. The second and third chapters describe the goals, background, specific methods, results and conclusion of

each of the two lines of approach. Shortly, in the first project, current analyses methods are applied to simultaneous EEG/fMRI data in order to study functional brain connectivity and hemodynamic correlates during human sleep. In the second study; more methodological aspects are addressed, evaluating the potential of a non-linear method analysis called recurrence quantification analysis (RQA) to extract rapidly changing dynamic features of electrophysiological data which may be used to better study fMRI models.

CHAPTER 1

Magnetic resonance imaging

In 1946, Bloch and Purcell independently described for the first time the physical phenomenon of nuclear magnetic resonance (NMR), where they measured the precession effect of the spin around a magnetic field [12;13]. This achievement leaded both to receive the Nobel Prize in physics in 1952. In research, NMR was a rapidly growing field in organic chemistry and biochemistry. However, the idea to use NMR to obtain spatial information of an object came just in 1973 from Lauterbur [14]. The NMR image derives from radio waves signals coming from the proton in hydrogen nuclei as a result of its interaction with external magnetic fields. The contrast in such an image is provided by differences in the signal intensity from these nuclei in various tissues, and is determined by several factors like proton density or relaxation times T_1, T_2 and T_2^*.

When protons are placed in a static magnetic field B_0, their nuclear spins will just have two possible alignments, parallel or anti-parallel to the field. Protons aligned in parallel are at lower energy level then the anti-parallels. As it is common in nature to seek for lower energy levels, a slightly exceeding amount of spins will be placed in the parallel direction. At body temperature, when the difference of energy between the states ΔE is much lower than the thermal energy, the fraction of parallel and anti-parallel spins is given by the Boltzmann distribution [15]:

$$\text{Spin excess} \approx N\frac{\Delta E}{2kT}, \qquad (1.1)$$

N is the total number of spins present in the sample, T is the absolute temperature and k the Boltzmann's constant. In NMR, ΔE is found to be proportional to the strength of the magnetic field:

$$\Delta E = \hbar \gamma B_0 , \quad (1.2)$$

$\hbar$ is the Planck's constant h divided by 2π and γ the gyromagnetic constant of the respective nucleus.

Due to the larger number of parallel spins, a net magnetization vector is created $(\vec{M})$, and it is this vector that, through some experimental manipulation, give rise to an induced current in a receiver coil, required to generate a NMR image [15].

From Faraday's law of induction, in order to induce a current in a receiver coil, it is necessary that the magnetization vector (the magnetic moment vector density due the spin population) generates a variable magnetic field nearby the coil. In the thermal equilibrium, $\vec{M}$ is constant and aligned parallel to the magnetic field. To disturb this equilibrium, energy is required to provoke transitions between the energy levels. This is achieved by irradiating the protons with radiofrequency (rf) magnetic fields. However, according to quantum theory, the transition between energy levels just happens if the amount of energy exactly matches the difference of energy between the states, in this case, ΔE. This means that the photons of the rf field should have a frequency that satisfies:

$$\Delta E = h \nu , \quad (1.3)$$

h is the Planck's constant and ν is the radio wave frequency. This leads to:

$$\nu = \frac{\gamma B_0}{2\pi} = \frac{\omega_0}{2\pi} \Rightarrow \omega_0 = \gamma B_0 , \quad (1.4)$$

ω_0 is the angular frequency of the photon, referred as “Larmor frequency”. Therefore, the resonance phenomenon is the transition of protons between the energy levels by applying a rf with angular frequency ω_0.

A classical way to describe NMR is imagining the proton as a tiny spinning charge. According to classical physics, with protons in the presence of a static magnetic field $(\vec{B})$, the magnetic field will exerted a torque $(\vec{\tau})$ that twists the proton’s magnetic moment into a parallel alignment with the field. Because of the spin, the torque will not twist the magnetic moment vector into alignment with the magnetic field but will induce precession around the magnetic field direction while maintain a constant angle.

The relationship between the magnetic moment $(\vec{\mu})$ and the spin angular moment $(\vec{L})$ is:

$$\vec{\mu} = \gamma \vec{L} . \qquad (1.5)$$

For a volume element V small enough that the external fields are approximately constant over V but still contain a large number of protons, the magnetic moment vector density due to the spin population $\vec{M}$ will be:

$$\vec{M} = \frac{1}{V} \sum_i \vec{\mu}_i \text{ ,} \qquad (1.6)$$

With $i = 1...N$ (total of spins in V). If no interaction of the protons with their environment is assumed, the equation of motion can be simply written as:

$$\vec{\tau} = \frac{d\vec{M}}{dt} = \gamma \left(\vec{M} \times \vec{B} \right). \qquad (1.7)$$

Now, suppose the configuration in **Figure 1.1** where $\vec{B}$ is a constant with module B_0 at $\hat{z}$ direction and $\vec{M}$ with module M_0 written as:

$$\vec{M} = M_0\left[\sin(\theta)\cos(\varphi)\hat{x} + \sin(\theta)\sin(\varphi)\hat{y} + \cos(\theta)\hat{z}\right]. \quad (1.8)$$

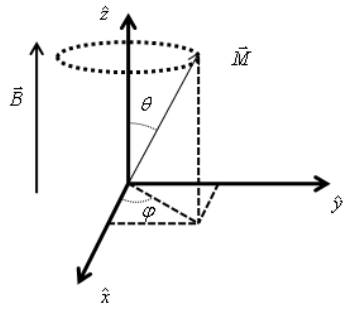

Figure 1.1 Magnetic and magnetization vectors representation. Vectors $\vec{B}$ and $\vec{M}$ in the orthogonal $(\hat{x},\hat{y},\hat{z})$ plane.

From **(1.7)**:

$$\begin{aligned}
&\cos(\theta)\cos(\varphi)\frac{d\theta}{dt} - \sin(\theta)\sin(\varphi)\frac{d\varphi}{dt} = \gamma B_0 \sin(\theta)\sin(\varphi),\\
&\cos(\theta)\sin(\varphi)\frac{d\theta}{dt} + \sin(\theta)\cos(\varphi)\frac{d\varphi}{dt} = -\gamma B_0 \sin(\theta)\cos(\varphi), \quad (1.9)\\
&\frac{d\theta}{dt} = 0.
\end{aligned}$$

The solution for **(1.9)** is:

$$\begin{aligned}
&\frac{d\varphi}{dt} = -\gamma B_0\\
&\frac{d\theta}{dt} = 0.
\end{aligned} \quad . \quad (1.10)$$

Note that $\frac{d\varphi}{dt} \equiv \omega = \omega_0$, where ω is the angular frequency $\vec{M}$ rotates around $\hat{z}$. The minus in **(1.10)** means that $\vec{M}$ rotates clockwise, with time, in the negative φ direction. Thus, when a constant magnetic field is applied, the magnetization will precess with the Larmor frequency and in a constant angle θ related to $\vec{B}$.

To produce a current in a coil, a magnetic moment needs to generate a variable magnetic field nearby the coil, thus $\frac{d\theta}{dt} \neq 0$. To accomplish this, the magnetization can be rotated away from its alignment along the $\vec{B}$ axis by applying a radiofrequency magnetic field for a short period of time (rf pulse) with the Larmor frequency. After the magnetization has been rotated into the transverse plane, it will tend to relax to equilibrium along the direction of the static field $\vec{B}$. The NMR signal corresponds to the voltage induced in a receiver coil from time-varying magnetic flux which is produced by this rotating magnetization.

The goal of imaging is to correlate a series of signal measurements with spatial locations of the various sources. Lauterbur proposed in 1973 [14] to use magnetic field gradients (spatially changing magnetic fields) to label the signal from protons according to their spatial position. If the magnetic field is dependent, for example, on its x coordinate, so is the Larmor frequency, thus it is possible to selectively excite protons belonging to a plan perpendicular to $\hat{z}$ by choosing an excitation pulse having the exact frequency corresponding to the Larmor frequency of the chosen plane (slice selection). During data acquisition, a magnetic field along the x-axis results in a precession frequency which depends on the precise localization of the respective spins. Therefore, the induced current in the receiver coil comprises a sum of different precession frequencies, which can be decomposed by a fast Fourier transformation. The x gradient is also called the read-out gradient. The y coordinate of the protons is labeled with a gradient pulse along the $\hat{y}$ direction (frequency encoding) before the acquisition of the signal. This gradient makes protons situated in different y positions present different phases. By repeating this frequency

encoding step with successively increasing y gradient strength, the signal obtained during the frequency encoding can be decomposed later on, again using Fourier transform.

So far, the interaction between spins and their environment was neglected; however, it is necessary to consider both internal magnetic and electric fields. These fields influence the magnetization, a process known as relaxation. A set of equations was proposed by Bloch to describe the temporal evolution of the magnetization that incorporates the relaxation and precession effects [12]. The relaxation back to the longitudinal orientation is characterized by a time constant T_1 and the transverse loss of phase coherence, perpendicular to the field B_0, by T_2. The transverse relaxation T_2, based on spin-spin interactions, is of special importance for fMRI. In a perfectly homogeneous magnetic field, the transverse relaxation would decay exponentially with a time constant of T_2. Local field inhomogeneities, however, disturb the phase coherence and increase the speed of this transversal relaxation process, resulting in a decay of constant T_2^* shorter than T_2. Such field inhomogeneities may be caused by external factors like an inhomogeneous magnetic field or by anatomical features, like e.g. air filled cavities close to brain tissue causing transitions in magnetic susceptibility. In the brain, these inhomogeneities may also depend on altered physiological states, as the local blood supply and the blood oxygenation are altered by neural activity [3]. Therefore, macroscopic tissue properties can be derived from T2*.

Functional magnetic resonance imaging (fMRI)

In 1990, Ogawa et al. [16;17] observed for the first time that the a specific NMR contrast is sensitive to the oxygenation level of the blood, then termed “blood oxygenation level dependent” (BOLD) contrast. Since the hemoglobin is a diamagnetic molecule when oxygenated (oxyhemoglobin) but paramagnetic when deoxygenated (deoxyhemoglobin), the presence of deoxyhemoglobin affects the local magnetic susceptibility by creating small distortions in the magnetic field and consequently, decreasing T_2*. Upon neural activation, the increases in cerebral blood flow (CBF) are about ~ 2-4 times larger than increases in cerebral metabolic rate of oxygen ($CMRO_2$). As a result, the supply of oxygen to the capillary bed is substantially increased, but only a fraction of oxygen is removed from the blood to sustain metabolism, so in total, the blood is locally more oxygenated and T_2* is increased [2]. This makes it possible to define the anatomical locus of the activation by means of fMRI. However, it is important to be aware that the BOLD signal does not directly measure neural activation but rather reflects a hemodynamical cascade of changes in CBF, $CMRO_2$ and cerebral blood volume (CBV). This neurovascular coupling produces a complex MR (magnetic resonance) signal function related to the neural response to stimuli: the hemodynamic response function (HRF) which can be used to analyze amplitude changes in the MRI images in the order of 0.5 – 3 %, see **Figure 1.2.**

FMRI studies are mostly analyzing “evoked activity”, in other words, neuronal response to brief stimuli or activity during a task performance in association to such stimuli. Several sophisticated statistical methods have been developed to identify significant signal changes which are taken as representation for changes in neural activity at that location. The first step of such an experiment is to carefully plan the

experimental paradigm to be worked on by the subject. The paradigm corresponds to the series of tasks to be performed during the fMRI measurement.

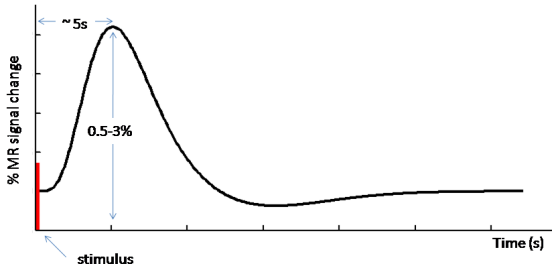

Figure 1.2. Hemodynamic response function following a hypothetical short duration stimulus (represented by the red bar). The maximum amplitude of the MR signal changes is in the order of 0.5-3% and has a delay of ~ 5 s after stimulus presentation. Graph created using SPM software version 5 (www.fil.ion.ucl.ac.uk/spm).

Currently, fMRI typically involves acquisition of a continuous series of scans with BOLD contrast images of the whole brain collected every 1 – 2 s (depending on the time of acquisition or repetition time – TR). A scan consists of several thousand data points, each of which is derived from a small cube of brain tissue or voxel (volume element). Due to the low amplitude of such evoked signals (**Figure1.3**), usually the subject has to perform the same task several times to increase the statistical power in detecting these signals. A typical example is a block-design, where the subject maintains cognitive engagement in a task altering with periods when a different condition is required. **Figure 1.3a** represents a block-design, with the subject being exposed to auditory stimulations during 30 s intercalating with silent periods of 30 s. **Figure 1.3b** shows brain regions in the auditory cortex in which the BOLD signal fits to the hypothesis of an increase during the auditory stimulation and a return to the baseline during the silent periods (red line in **Figure 1.3a**). Depending on the research question, the paradigm can be much more complex, with a design in an event-related (short periods of task intercalated with long control periods, the HRF

of a single event can be detected and analyzed in detail) or mixed fashion (a combination of events closely presented, intermingled with control condition), or a behaviorally driven one (for example, resting-state studies, to be better explained later).

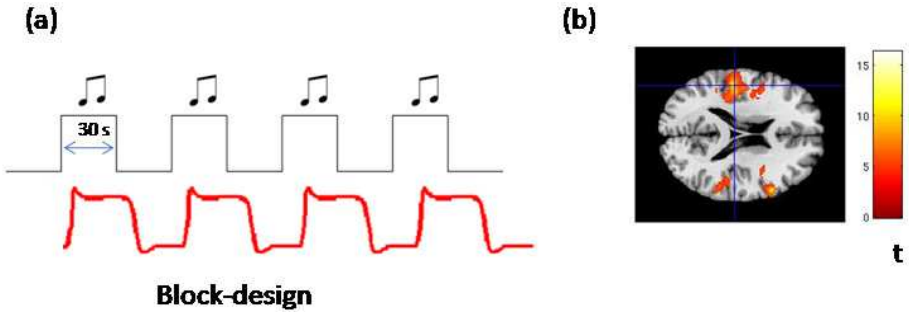

Figure 1.3. (a) Example of a block-design with 4 blocks of auditory stimulation during 30 s intercalating with 5 silent blocks of 30 s. The red line represents the expected HRF. (b) Activation in the auditory cortex in response to the task in (a) given as red cluster overlayed on an anatomical MR image. Color bar represents t-values depiction statistical significance of the derived action clusters.

Intuitively, after recording fMRI data, the first attempt would be to statistically compare the temporal signal of each voxel in the image with the expected HRF. However, during recording, the data can be corrupted by movement of the subject, heartbeat, breathing, inhomogeneities of the magnetic static field, differences in the acquisition time of the images and other factors. Therefore, before reaching a final result image as displayed in **Figure 1.3b**, many preprocessing steps are needed to eliminate artifacts and signal changes not associated with the experimental design and to maximize the sensitivity of the statistical analysis. The basic steps include slice time correction, motion correction, spatial and temporal filtering. For a group analysis a normalization process is also needed.

FMRI preprocessing

Slice time correction

The scan of a whole brain volume is not instantaneously measured. Instead, several slices are recorded two-dimensionally and then reconstructed as a three-dimensional image. Hence, each slice is recorded at a slightly different time with respect to a given stimulus which should be corrected for. One could, for example, assume different HRFs for each slices, however, the most common procedure is to interpolate the time series to “align” the slices prior to analysis. The advantage of interpolation is that inferences concerning differences in HRF amplitude between slices are less likely to be confounded by different slice acquisition times. However, this approach is limited by the Nyquist frequency ($1/2TR$) which makes the interpolation unable to contain experimental power at frequencies above this frequency [18].

Motion correction

For fMRI data analysis it is also necessary that each voxel is spatially invariant during the whole experiment. Variation of intensity in the same voxel between repeated volume acquisitions is primarily supposed due to changes in cerebral physiology. However, during the experiment, movement of the head by the subject, physiological motions related to respiration and pulsation of the blood can result in shifting the signal time-courses of neighboring voxels. Thus, when preparing the experiment, the comfort of the subject and demand of the task should be taken into account to avoid movements. Still, some methods can be applied after acquisition to minimize these movement artifacts. These methods assume that the

brain does not change in shape during the experiment and that any motion can be corrected for by rotations and translation along x, y, z axes. This is referred to as rigid body transformation with six degrees of freedom (3 rotations and 3 translations) [19]. The rotation ($\vec{R}$) and translation ($\vec{T}$) matrixes are defined based on a reference volume (usually the first one):

$$\vec{x}^{(2)} = \vec{R}\vec{x}^{(1)} + \vec{T} \qquad (1.11)$$

where $\vec{x}^{(1)}$ and $\vec{x}^{(2)}$ are the positions of the voxel vectors before and after the correction and the matrixes $\vec{R}$ and $\vec{T}$ (**Figure 1.4**) are found to be the ones to minimize the sum of squared difference between two voxels of subsequent volumes.

Abrupt motion can lead to artifacts in time series even after motion correction, thus data with motion exceeding 2 mm are usually discarded.

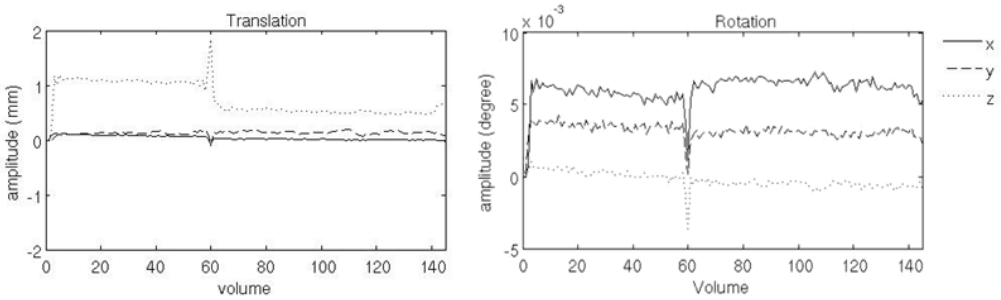

Figure 1.4. Matrixes $\vec{R}$ (rotation) and $\vec{T}$ (translation) found during the motion correction preprocessing step. Graph created using SPM software version 5 (www.fil.ion.ucl.ac.uk/spm).

Normalization

Until now, it was described how to identify activated brain areas in a single subject. In order to identify the exact anatomical location, and to generalize such individual findings to a population level and to make results from different studies comparable, it is necessary to standardize data to a normative space. The

normalization step in the statistical parametric mapping (SPM) software registers images of different subjects into the same atlas based coordinate system defined by the Montreal neurological institute (MNI) using a large series of MRI scans on healthy subjects. The registration consists of linear (accounts for major differences in head shape and position) and nonlinear transformations (accounts for smaller-scale anatomical differences). The linear transformation determines 12 affine transformations (3 translations, 3 rotation, 3 shears and 3 zooms) to match positions and sizes of images (**Figure 1.5**).

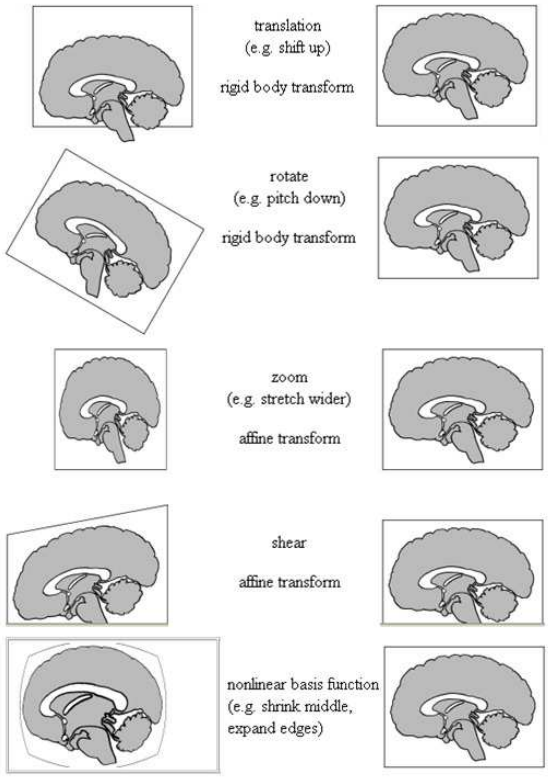

Figure 1.5. Visual representation of linear and nonlinear transformations held in the SPM software normalization step. Figure taken from [20].

In order to increase the robustness and accuracy of the approach, information about the variability of head sizes is included within a Bayesian structure. Still, given the small number of parameters, it does not allow for every feature to be matched

exactly. Warps, therefore, are modelled by linear combination of smooth discrete cosine transformation basis functions to correct gross differences in head shapes that cannot be accounted for by the affine transformation [21].

A well know and frequently used atlas is the Brodmann atlas which was created based on the cytoarchitectural organization of the human cortex by a German neurologist, Korbinian Brodmann [22]. Later on, many of the Brodmann areas could be associated with diverse cortical functions (**Figure 1.6**).

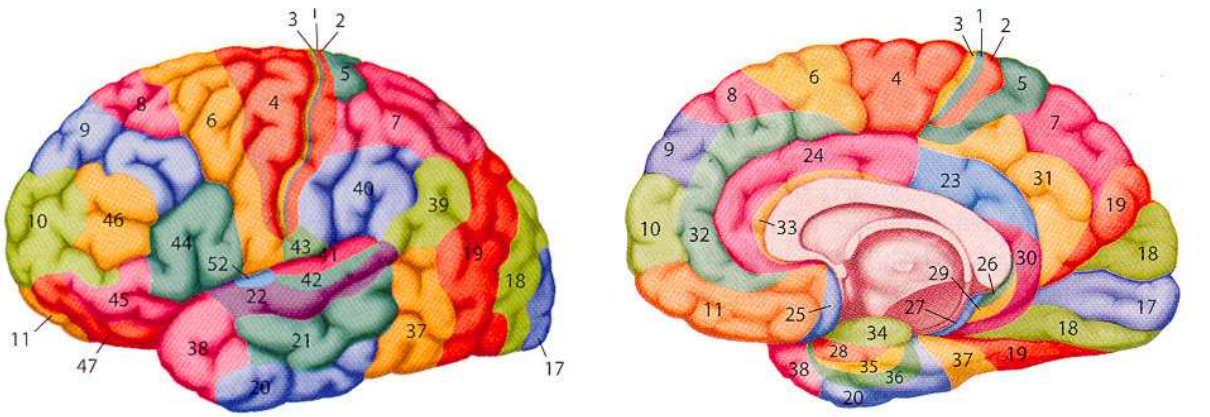

Brodmann areas and some common associated functions	
1, 2, 3 = primary sensory cortex **4** = motor cortex **5, 7** = secondary sensory cortex **6** = supplementary motor area (medial) and premotor cortex (lateral) **8** = frontal eye fields **9/46** = dorsolateral prefrontal cortex **10** = frontopolar cortex **11, 12** = orbitofrontal areas	**17** = primary visual cortex **18, 19, 20, 21, 37** = secondary visual cortex **24, 32** = anterior cingulate cortex **41** = primary auditory cortex **22, 42** = secondary auditory cortex **39** = angular gyrus, part of Wernicke's area **40** = supramarginal gyrus, part of Wernicke's area **44/45** = Broca's Area **47** = Ventrolateral prefrontal cortex

Figure 1.6. Brodmann atlas and common associated function. Figure taken from [23].

Spatial smoothing

The main goal of spatial smoothing is to suppress noise while maintaining the signal of interest. Another reason to apply spatial smoothing is that the subsequent statistical analysis requires the data to be normally distributed and spatial smoothing

of the data has a normalizing effect [19]. Individual differences in brain anatomy also become less pronounced by smoothing and hence a cross-subject analysis is more valid. The spatial smoothing is usually carried out by convolving a 3D volume with a Gaussian kernel. The smoothing filter is defined by its full width half maximum (FWHM), referring to the width of the Gaussian curve at half of its maximum.

Temporal filtering

The temporal filtering removes components of the temporal series that fluctuates faster (lowpass filter), like pulsatil rhythms and frequency above the Nyquist limit, or slower (highpass filter), like MR scanner drifts, than the predicted activation. Different from the spatial filtering that is applied in each volume separately, the temporal filtering is applied in the time series of each voxel. As statistical analyses are directly applied on the time series, this filtering should be performed after all the other preprocessing steps.

Statistical analysis

SPM has been extensively used to characterize neuroimaging data sequences. It uses the general linear model (GLM) and classical statistics, under parametric assumptions, to perform a statistical test (usually the T-statistics) at each voxel. Inferences about regionally specific effects are based on the resulting image of T-statistics (**Figure 1.3b**) [24]. The GLM describes the recorded data (y) as the combination of weighted functions representing the expected HRFs (predictors) plus an error (e):

$$y = \beta_0 + \beta_1 X_1 + \beta_2 X_2 \cdots + \beta_L X_L + e, \qquad (1.12)$$

where β_i is the weight of the predictor function X_i, β_0 represents constant factors, e.g. the baseline fMRI image intensity, and L the total number of predictor functions needed to describe the experiment. For an experiment of J recorded volumes, **Equation (1.12)** can be written in a matrix notation as:

$$\begin{pmatrix} y_1 \\ \vdots \\ y_J \end{pmatrix} = \begin{pmatrix} x_{11} & \cdots & x_{1L} \\ \vdots & \ddots & \vdots \\ x_{J1} & \cdots & x_{JL} \end{pmatrix} \begin{pmatrix} \beta_1 \\ \vdots \\ \beta_L \end{pmatrix} + \begin{pmatrix} e_1 \\ \vdots \\ e_J \end{pmatrix}$$

$$\vec{Y} = \vec{X} \times \vec{\beta} + \vec{e} \qquad (1.13)$$

$\vec{Y}$ is the column vector of observed data, $\vec{e}$ and $\vec{\beta}$ are the error and weight vectors respectively. $\vec{X}$ is the $J \times L$ matrix with each line representing one recorded volume and each column a predictor function. The predictor functions are created with the assumption that the BOLD signal changes can be estimated by convolving the HRF with the stimuli onset times. **Figure 1.7** shows a schematic representation of the GLM.

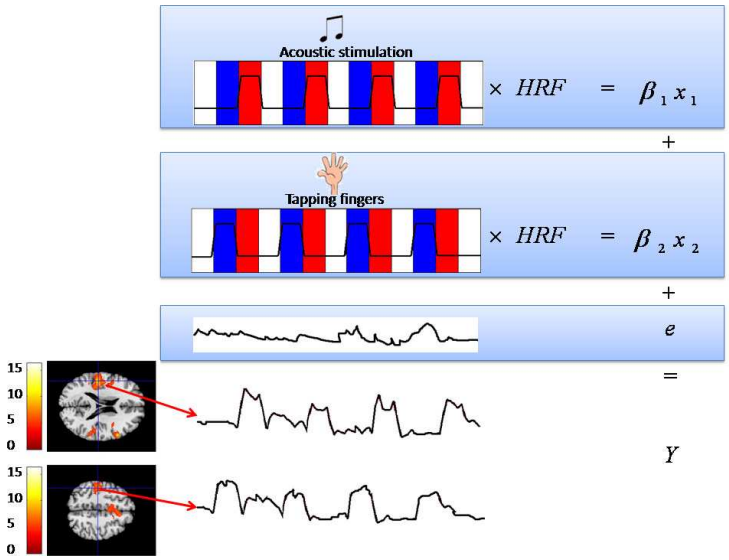

Figure 1.7. Schematic representation of the general linear model (GLM). The paradigm consisted of an auditory stimulation (red blocks) intercalated by a tapping finger task (blue blocks) and a rest period (white blocks). The prediction functions were supposed to be the two

stimuli presentation time course convolving with the HRF (x_1 and x_2). The two last time courses are examples of possible measured time course of two different voxels in the fMRI. The insert on the lower left shows typical activation maps derived by SPM showing activation in the auditory cortex associated with tone presentation (top) or in the motor cortex representing the finger taping condition (bottom).

$\vec{\beta}$ values are estimated by minimizing the residual values ($\vec{e} \to 0$), thus if $\widetilde{\beta} = \left(\widetilde{\beta}_1, \cdots, \widetilde{\beta}_L\right)$ are the estimated values and $\widetilde{Y} = \left(\widetilde{Y}_1, \cdots, \widetilde{Y}_J\right) = \vec{X}\widetilde{\beta}$ the adjusted values, then $\vec{e} = \left(e_1, \ldots, e_j\right) = Y - \widetilde{Y} = Y - \vec{X}\widetilde{\beta}$. The residual sum of squared will be $S = \sum_{j=1}^{J} e_j^2 = e^T e$, that is the sum of squared difference between the measured values and the estimated ones. Finding the minimum of $\vec{e}$ implies $\frac{\partial S}{\partial \widetilde{\beta}_l} = 0$ and this leads to $\hat{\beta} = \left(X^T X\right)^{-1} X^T Y$ (if $\left(X^T X\right)$ is invertible) where $\hat{\beta}$ is the optimized value. These simple equations can be used to implement a vast range of statistical analyses [25].

Model free analysis

More recently, another method of fMRI analysis has emerged, focusing on spontaneous fluctuations or “intrinsic activity” of the brain instead of evoked activity. The brain at rest is responsible for most of the cerebral energy consumption whereas task related increases in neuronal metabolism are usually less than 5%. The term “intrinsic activity” summarizes any ongoing neural and metabolic activity that is not directly associated with the subject performing a task. It is usually recorded when the subject is asked to relax but not fall asleep in the scanner with eyes closed (resting-state).

How can these intrinsic brain processes be analyzed [26]? One way to do this is to apply an independent component analysis (ICA). ICA performs hypothesis-free separation of input data into the linear sum of time varying modulation of maximally independent component maps. It does not need any a priori assumptions about the time course of the different component activations, e.g. whether a given component is active due to specific neuronal systems or is related to technical noise or other artifact sources [27].

It is acknowledged that the brain represents a complex network of dynamic systems, consisting of numerous functional interactions between various brain regions [28]. In this regard, fMRI can also be used to study such functional connectivity, e.g. temporal dependency of neuronal activity patterns in anatomically distinct brain regions. The evaluation of these dependencies can contribute to a better understanding of the brain's functional organization. Several approaches have been proposed to quantify functional connectivity patterns [29]. In **Chapter 2**, functional connectivity analysis is used on resting-state data to assess the connectivity of the hippocampal formation with the neocortex during different sleep stages. The time-course of a region-of-interest (ROI) is simply correlated against the time course of all other voxels and a high correlation means high functional connectivity.

Electroencephalography (EEG)

The communication processes between the 100 billion neurons in the human brain generates electrical activity, part of which can be recorded by the EEG. The first EEG data were recorded in 1924 by a German psychiatrist, Hans Berger, and reported in the essay "Electroencephalogram in Humans" in 1929 [30]. Since then, this technology has continuously improved and it still widely used to study intrinsic and evoked brain activities.

All neurons are covered by membranes that isolate and separate different concentrations of ions inside and outside the cell. Through the neuronal membrane are pore-forming proteins (ions channels) that manage the flux of specific ions in and out of the cells. Here, the electrochemical driven force is determined by the electrical potential difference across the membrane and the concentration gradient of the ions selective for the channel. In the inactive state of the cell, this force creates a potential difference across neural membrane, called membrane potential [31]. In this way, two main forms of neuronal activation can be distinguished; the fast depolarization of the neural membranes, which results in the action potential mediated by the sodium and potassium voltage-dependent ionic conductance, and the slower changes in the membrane potential due to synaptic activation, chemically mediated by several neurotransmitter systems [32]. The electrical activity as recorded in the EEG is a measure of the extracellular current flow from the summed activity of many neurons. The scalp EEG mostly reflects the activity of cortical neurons close to brain surface. Deeper structures as the hippocampus, thalamus or brainstem do not contribute directly to the EEG. Distant transmission of electrical impulses, however, has substantial effects on the surface EEG. Thalamocortical connections, for example,

are critical in the synchronization of most electrical activity, such as sleep spindles [31]. EEG scalp events can therefore (indirectly) reflect more deep-brain activity/connectivity.

Only vertically oriented dipoles are detectable with scalp electrodes. The part of the cortex that runs down the sulci, oriented orthogonal to the scalp, generate radially oriented dipoles, which are not well detected by the surface electrodes. Thus, the activities recorded by scalp electrodes are mostly generated by excitatory postsynaptic potentials (EPSP) produced in the pyramidal layer of the cerebral cortex. The pyramidal neurons are spatially aligned and perpendicular to the cortical surface and when activated, with a certain degree of synchrony, generate coherent electric/ magnetic fields that can be detected by electrodes placed at relatively small distances. [32]. **Figure 1.8** illustrates transient dipoles that lead to measurable extracellular voltage.

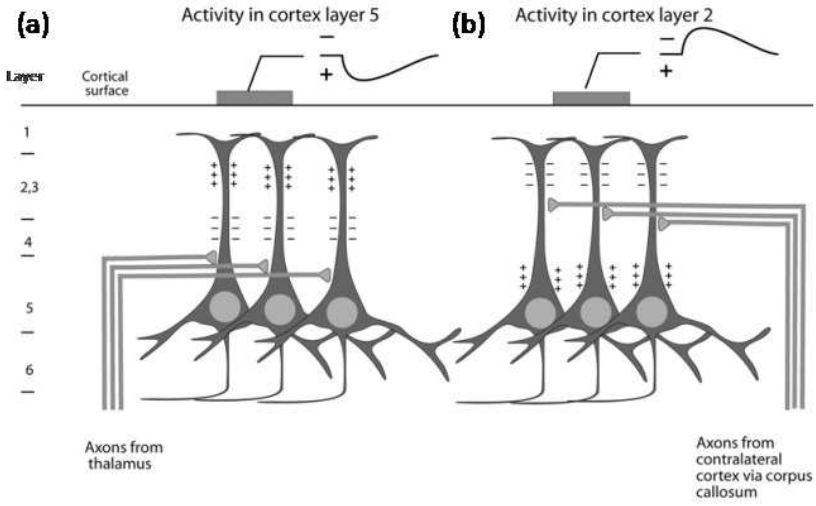

Figure 1.8 Afferent inputs into the apical (a) dendrites and (b) cell body. In both cases, the afferent stimuli lead to depolarization with current flow into the cell body. The current flow in (a) results in a source in the apical dendrite, whereas in (b), the source is located in the soma. This example thereby leads to two vertically oriented dipoles of opposing polarity that can be

detected by surface EEG. ***Figure reproduced with kind permission from Springer Science+Business Media: Basic Neurophysiology and the Cortical Basis of EEG, 2007, page 31, Gregory L. Holmes and Roustem Khazipov, figure number 6, Modified from Kandel et al., 2000 with permission [31].***

Unfortunately, EEG carries the problem that signals measured on the scalp surface do not directly indicate the location of the active neurons in the brain. Many different source configurations can generate the same distribution of potentials on the scalp. This ambiguity of the underlying static electromagnetic inverse problem has no unique mathematical solution [33]. The only way to localize the putative electric sources is to introduce a priori assumptions on the generation of the EEG signal. In the last years, many assumptions using different mathematical, biophysical, statistical, anatomical and functional constraints have been formulated and implemented in inverse solution algorithms [33]. Basically, there are two main approaches for estimating sources from observed sensor EEG: The first assumes that sensor data can be explained by a small set of equivalent current dipoles. Secondly, the source reconstruction problem has more recently been modeled by placing many dipoles in brain space and using certain constraints on the solution to make it unique. Most of these constraints are anatomical and physiological arguments, e.g., smoothness constraints and approximate location priors based on regional activity in fMRI.

EEG acquisition and preprocessing

In a typical EEG experiment, electrodes are positioned at standardized locations on the scalp, as for example defined in the international 10-20 system. The "10" and "20" refer to the distances between adjacent electrodes that are either 10%

or 20% of the total front-back or right-left distance based on reference points on the skull, respectively. This method was developed to ensure experimental reproducibility and to allow findings to be compared over time (see **Figure 1.9**).

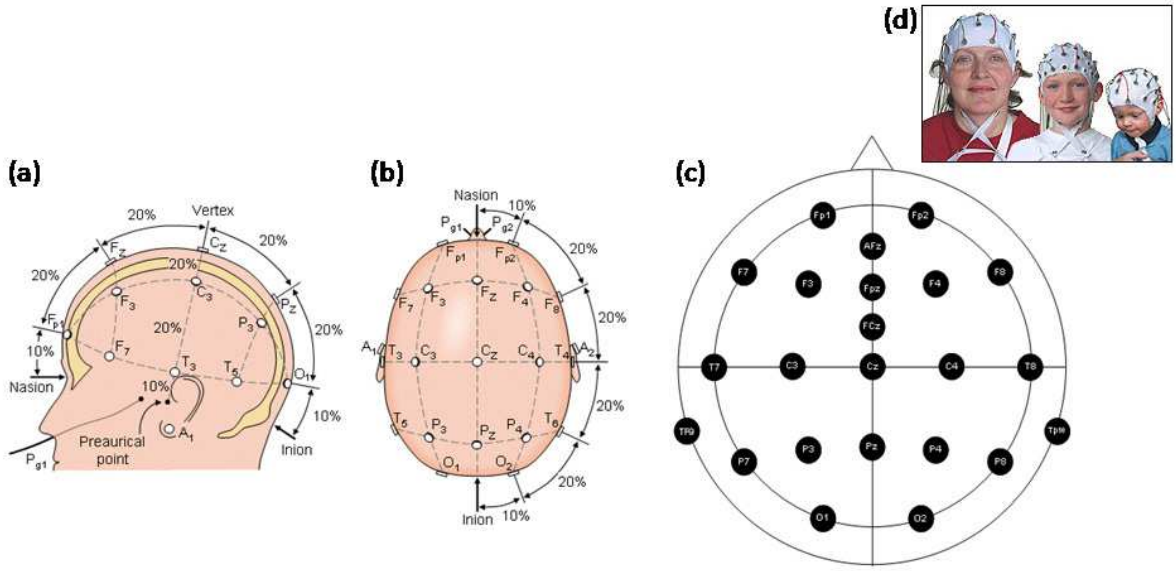

Figure 1.9. The international 10-20 system seen from (a) left and (b) above the head. A = Ear lobe, C = central, Pg = nasopharyngeal, P = parietal, F = frontal, Fp = frontal polar, O = occipital. Figure was taken from [34]. (c) Location and nomenclature of the electrodes used in the present study. AFz and FCz are the ground and reference electrode. (d) Visualization of typical caps used in EEG studies. Figure 1.9a and 1.9b were taken from [34]. Figures 1.9c and 1.9d were taken from [35].

Beside the mathematical and statistical approach used to interpret the EEG data, technically satisfactory recordings are required to ensure accurate results. EEG is more difficult to measure due to its low amplitude (in the μV range) caused by the skull's composition if compared with other noninvasive biosignal measurements such as the electrocardiogram (ECG), electromyogram (EMG) and electrooculogram (EOG). The first challenge is to thoroughly place the electrodes on the subject's head. The skin and deeper tissues between a pair of electrodes have resistive and capacitative properties. The impedance of these tissues can be decreased by

preparation of the skin using suitable abrasion underneath the electrode contacts. In a noninvasive electrical brain signal measurement, an interface material is applied between the electrode and the skin to provide optimal ionic current and to reduce contact impedance between the electrode surface and the scalp. This material is an electrolyte and can be purchased in EEG gel or paste form.

During recording, technical artifacts can often appear due to loose contact of electrodes, which results in electrical noise or baseline drifts. The baseline drift artifact can be seen as another type of electrode artifact. The power spectrum of the low frequency component increases sharply when the baseline drift occurs. An unstable impedance of the electrode is the main reason leading to such artifacts, but sweating and body movement may also add to this effect [36]. To compensate for baseline drifts, highpass filters can be applied. Other off-line correction of DC drifts artifacts was proposed by Hennighausen in 1993 [37]. The main idea of this method is to calculate the average of consecutive EEG segments and perform a regression of these values. The amplitude trend which can be explained by either a linear or non-linear regression model is then subtracted from all data points. It should not be forgotten, however, that slow drifts could also represent meaningful activity related to habituation, attention or arousal level of the subject during the experiment.

EEG recordings are contaminated by physiological artifacts as eye blinks or other eye movements, as well as by EMG and ECG activity. The movement coming from eyes or muscles cause rather large signals, which may obscure the low amplitude EEG signals coming from the brain [36]. Many of these artifacts cannot be corrected for, and the EEG segments in which they occur must be excluded from analysis. One frequently used attempt to correct for ECG and EOG artifacts is

applying ICA. Components with strong ECG and EOG related time courses are visually identified and removed from the data after an ICA back-transform.

Simultaneous EEG and fMRI recordings

EEG/fMRI simultaneous data acquisition is becoming more common and essential in both basic and clinical brain research. Cognitive neuroscience, epileptology, psychiatry and sleep research all benefit from the combination of these methods. This multimodal approach is a key tool to enhance the understanding of brain activity due to the conjunction of the good spatial resolution of fMRI and the good temporal resolution of EEG, respect and its complementary aspect covering electrophysiological and hemodynamic related changes. However, the successful combination of EEG and fMRI demands careful consideration of patient safety, as well as EEG and MR image quality.

The EEG equipment appropriated for use in the MR environment must exclude ferromagnetic material and should limit rf emission to preserve image quality. Potential sources of rf emission are active circuitry in EEG instrumentation located in the scanner room or the ingress of rf signals via conductors that breach the scanner's Faraday shield. Rf signals should be minimized at source by using low-power digital components, thereby minimizing switching currents. All active circuitry should be enclosed in conductive enclosure and all conductive signal paths breaching this enclosure should do so via inline rf filters. Normally, the EEG preamplifiers are located in the scanner room and EEG data is transmitted to a receiver in the console room via fiber optic cables, therefore eliminating the ingress of rf from outside the scanner. Regarding the instrumentation material, fortunately, this is not a significant limitation since there are a range of nonferromagnetic materials that are suitable to high-quality EEG as silver, silver chloride, gold, carbon and conductive plastic EEG electrodes [38].

The rapidly switching rf and magnetic gradient fields applied during MR data acquisition induce eddy currents in the electrodes and may result in heating of the electrode [39;40]. Several studies, however, showed that the local temperature increase is less than $1^{o}C$ in scanners of 1.5T and 4T [39;41;42], and thus within the permitted limit [39]. The interaction between the scanner (rf) and the electrode leads can result in tissue heating as well. The rf field will induce an electromotive force (emf) in any conductive loop formed by the electrode leads which is proportional to the loop area cut by the field and its rate of change. Thus, if tissue is part of this loop the emf will drive a current through it, resulting in heating. The electric component of the rf can induce a current along the extended conductor formed by an electrode lead. The magnitude of this current depends on the wire to the source of electric field in the MR transmitter coil, the resonant length of the electrode leads in relation to the rf wavelength among others [38]. Lemieux et al. [39] compared both sources of heating and found that the first one is stronger, but that a current-limiting resistor of 12 Ω in the scalp electrode leads could limit contact currents to acceptable levels. This additional resistance is small compared with typical input impedance of an EEG amplifier (around 10 MΩ) and does not degrade EEG signal quality significantly [38].

In the so performed EEG recording, the fMRI recording, including switching of magnetic field gradients and transmission of rf pulses, induces several different types of artifacts in the EEG, basically the gradient and the cardiac pulse-related artifacts. The amplitude of the gradient artifact is in the range of 10000 μV (~100 times higher than normal EEG) and can reach speeds of 20000 μV/ms (500 times faster than spontaneous EEG), see **Figure 1.10**. The most frequently applied method to correct this technical artifact comes from the assumption that two acquisition of the same

slice or volume will generate precisely the same artifact in the EEG data, thus the artifact can be easily modeled in a template and subtracted from the raw EEG [43].

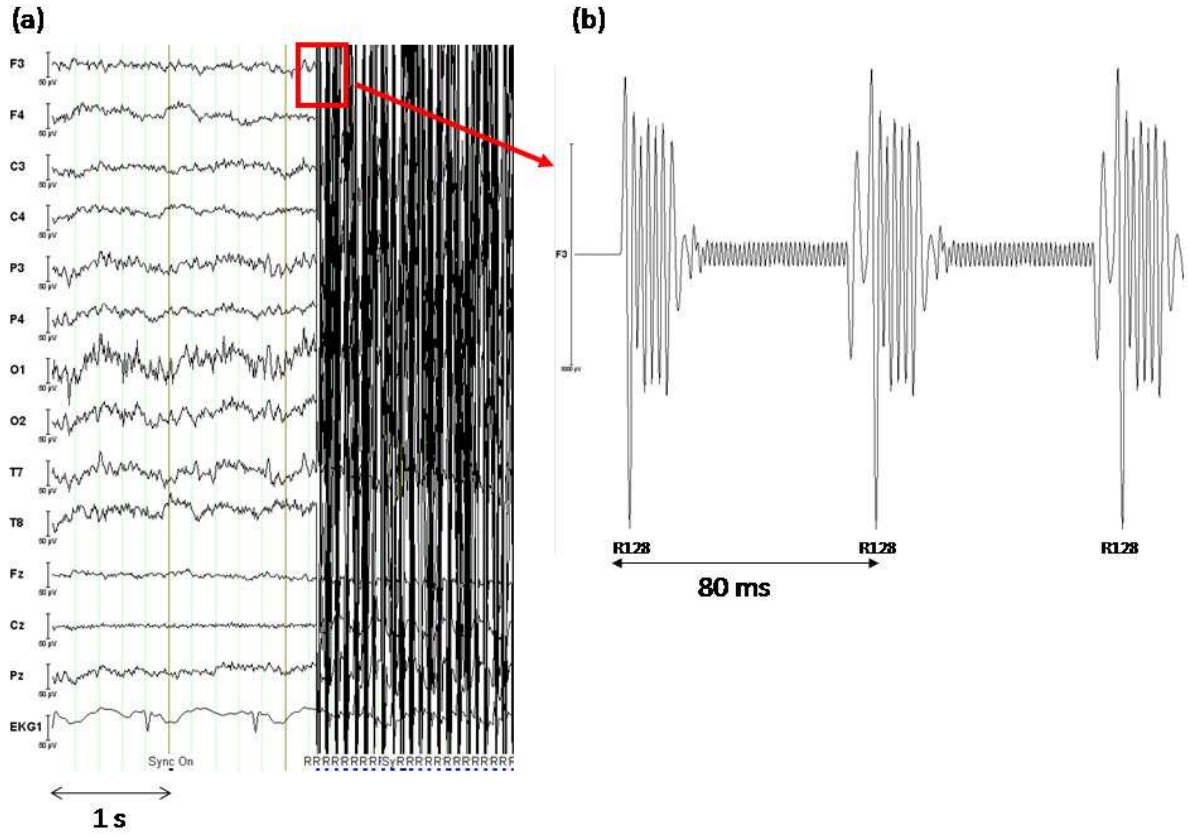

Figure 1.10 Example of gradient artifact in a concurrent EEG recording. (a) shows one ECG (EKG1) and 13 EEG (F3, F4, C3, C4, P3, P4, O1, O2, T7, T8, Fz, Cz, Pz) channels. The ECG was downscaled by a factor 20. (b) shows a zoom of the red box in (a) with strong gradient induced artifact shadowing the underlying EEG. Time and amplitude are displayed for each. The marker R128 is automatically delivered by the MR scanner and defines the exact time at which a new slice acquisition starts. Note the high similarity of the gradient induced artifacts in (b).

The amplitude range covered and sampling rate of the EEG recorded inside a MR scanner should be high (e.g. ± 16V, 5000Hz for BrainAmpMR) in order to detect and correct the very fast artifacts introduced by the scanning procedures. Creation of precise artifact templates in the EEG is much improved by exact knowledge on slice acquisition starts. During recording, the scanner used in **Chapter 2** and **3** (1.5 Tesla

Signa Echospeed, General Electric, Milwaukee, Wisconsin, USA) gave a TTL signal output at the exact time it started a new slice acquisition. These signals were entered and saved as markers in the EEG recording and can later be used to build a correction template across all consecutive volumes (marker R128 in **Figure 1.10**). Another prerequisite to a good template construction is that the onset of each fMRI volume to be acquired coincides with the exact time point at which an EEG data point is being sampled. Otherwise, there would be a temporal misalignment between the two acquisition systems that invariably will lead to a massively increased variance or error in the gradient correction template [43]. In order to achieve synchronicity between an fMRI sequence and the regular sampling pattern of the concurrent EEG, the repetition time TR of the fMRI sequence must be a multiple of the EEG sampling interval and the internal clocks of both systems, EEG and MRI, must be phase locked. Luckily, nowadays, commercial EEG recorders are equipped with synchronization hardware that embraces this last issue [44]. Finally, after an optimal data acquisition, a template based on an average of several imaging artifact waveforms is calculated over a number of epochs and eventually subtracted from the EEG [45]. As the high sampling rate is no longer necessary after gradient artifact correction, and in order to decrease data size, the corrected data is down-sampled at this point. In the software Brain Vision Analyzer, this down-sampling is performed by using a Hanning window to calculate a weighted average for the data points. After subtraction of the averaged artifact curve, low-pass and band-rejection filters may be used to remove further artifacts.

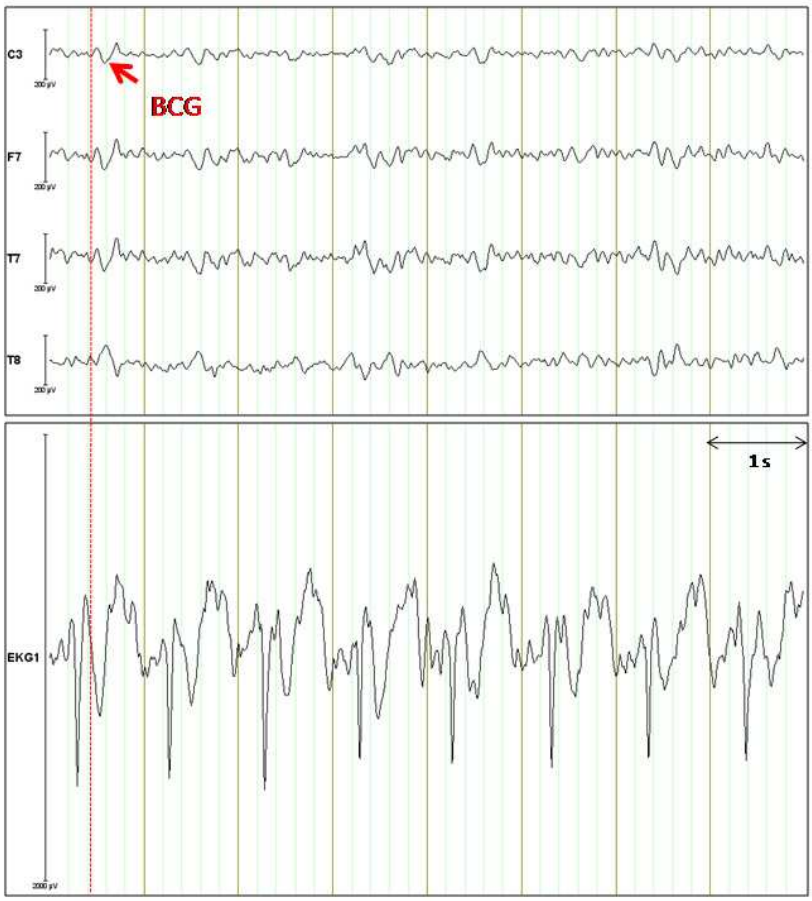

Figure 1.11 Example of BCG artifact in a concurrent EEG recording. The figure shows one ECG (EKG1) and 4 (C3, F7, T7, T8) EEG channel. Note that the amplitude resolution of the EEG electrodes is different from the ECG. The red line helps to see that the BCG is slightly delayed with respect to the ECG.

Another challenge is posed by the ballistocardiogram (BCG) artifact, produced by cardiac pulse-related movements of the scalp electrodes inside the static magnetic field. These movements might result from acceleration and abrupt directional change in blood flow in the aortic arch during each heart beat [46]. Scalp movement may also occur due the expansion and contraction of the scalp arteries [47]. In an EEG channel, this artifact peak normally occurs slightly after the QRS complex (delayed by ~ 200 ms) [47], see **Figure 1.11**. While gradient artifacts are highly predictable, BCG artifacts display much greater variability due to their

physiological origin. The amplitude of the BCG can exceed 200 μV obscuring completely the neural activity detected by EEG. Furthermore, it covers a substantial frequency range coinciding directly with neural signals that are of interest, making the use of filters to remove this artifact many times impractically [48]. Allen et al. [47] introduced a method based on averaged artifact subtraction, which is characterized by a subtraction of a mean BCG artifact template calculated for each electrode during the previous 10 s. More recently, methods based on ICA were successfully used to solve this problem [49;50]. As already mentioned, the strength of ICA is that it makes no assumption about the mixing process of the different noise sources, except that this occurs linearly. This method consists in recovering unobserved statistically independent signals or “sources” from several observed mixtures or different combination of the “source signals” [51].

CHAPTER 2

Sleep spindles and hippocampal functional connectivity in human NREM sleep

Introduction

Sleep

Sleep disturbances have a great impact on quality of life, morbidity/mortality, public health and productivity [52] and can manifest in many psychiatric disorders like depression and schizophrenia, among others [53-55]. During the last years, neuroimaging has proven a valuable non-invasive tool to detect anatomical, functional and metabolic changes associated with sleep disturbances. The beginning of sleep research, however, is much older and is closely connected with the invention of the EEG. Using EEG, in 1937, Loomis showed for the first time that sleep was not homogeneous during the whole night but constitutes of different sleep stages [56]. Today, these sleep stages are scored according to the Rechtschaffen and Kales [57] criteria based on EEG, EOG and EMG recordings. The main states of vigilance are wakefulness, rapid eye movement (REM) sleep and NREM sleep. NREM sleep is further subdivided into stages 1, 2, 3 and 4 with slow wave sleep (SWS) comprising stages 3 and 4, see **Figure 2.1**. The rhythmic neuronal activity changes in sleep are accompanied by changes in information processing and state of consciousness. The transition from being fully awake to being clearly asleep is of great importance to understand clinically relevant changes in alertness and sustained attention and is associated with well-established EEG changes [58]. The EEG pattern associated with each behavioral state is quantified by the power of specific rhythms in certain frequency bands. Sleep stage 1 (S1) is characterized by a decrease in high

frequency oscillations and a dominance of (slower) theta rhythms (4-8 Hz) in the EEG and by lower EMG levels as compared with wakefulness and the appearance of slow eye movements [59;60]. Behaviorally, it includes: a decrease sensory perception and a partial cessation of responses to external stimuli [7;61;62]. S1 seems to be associated with decreased activity in the frontal and parietal cortices, and in the thalamus [10]. The thalamus plays a critical role in processing, integrating, correlating, and relaying sensory and motor information The thalamocortical network modulates the flow of sensory and motor information to and from the cerebral cortex [62]. Starting in early NREM sleep S1, the thalamocortical neurons undergo progressive hyperpolarization leading to a reduced synaptic responsiveness and interruption of the bidirectional flow of information. This has been further linked to sleep spindles (**Figure 2.1b**) [62-66] during deeper NREM sleep stages. Sleep spindles are waxing – and – waning 11 - 15 Hz oscillations and can be subdivided in slow (11 - 13 Hz) and fast (13 - 15 Hz) spindles, predominant in frontal and centro-parietal areas, respectively [64]. Sleep spindles are most prevalent during sleep stage S2, which is also associated with a low level of consciousness. S2 is also characterized by the presence of a sharp negative wave followed by a slower positive wave pattern, called K-complex (KC), see **Figure 2.1b**. KCs can appear spontaneously or be evoked by external stimuli. SWS is associated with the deepest level of unconsciousness and lowest energy metabolism and is dominated by a high amplitude EEG with frequencies lower than 4 Hz [59;67;68]. REM sleep, also called paradoxical sleep, shows an EEG resembling wakefulness or S1 sleep, and is further characterized by atonia of voluntary muscles (e.g. not affecting heart or respiratory muscles, and in addition eye muscles) as reflected by lowest chin EMG level as well

as by rapid eye movements (**Figure 2.1c**) [57;69]. Awaking from this state of high cortical activity goes along with higher incidences of vivid dream reports [63;67].

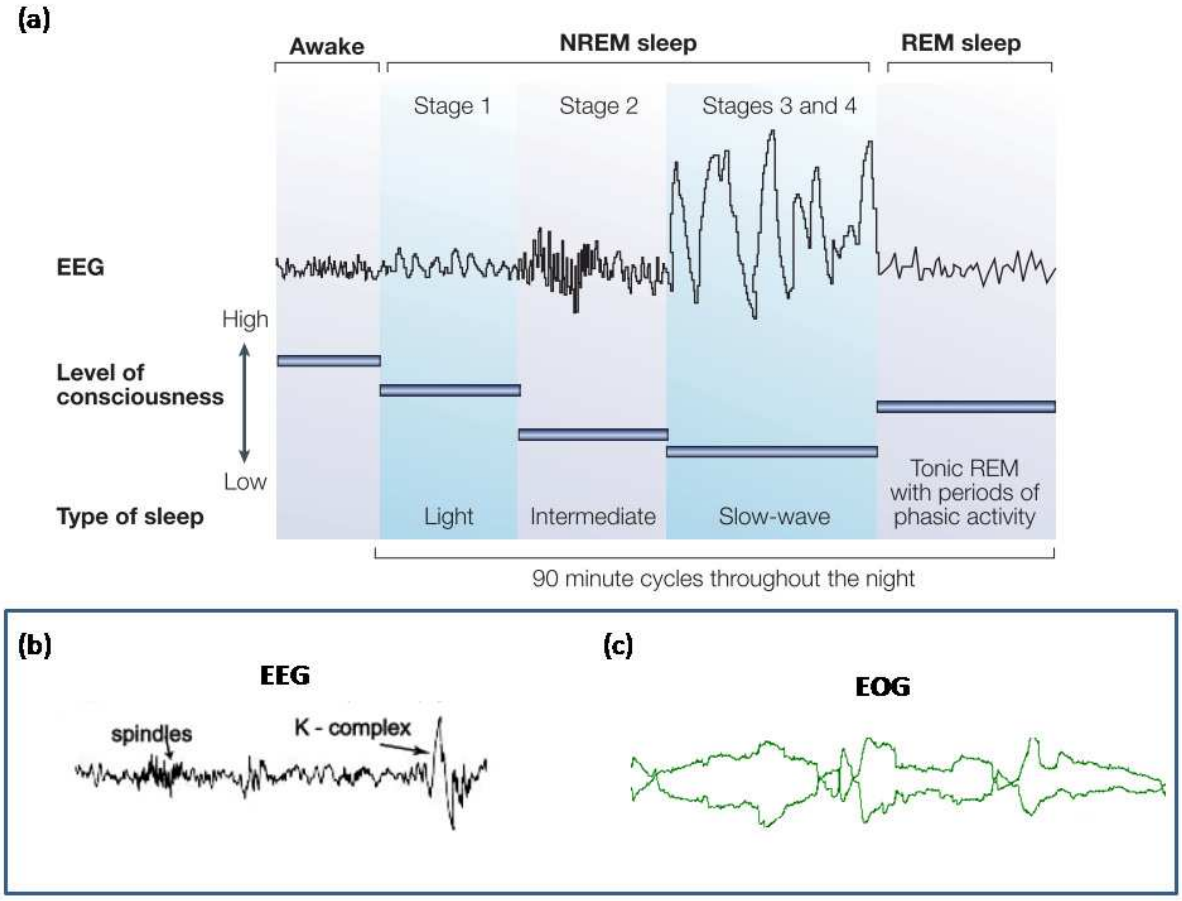

Figure 2.1. Relationship between human sleep, level of consciousness and EEG patterns. (a) Stages of sleep are characterized by differences in the frequency and amplitude of EEG waves. Wakefulness is characterized by a desynchronized high-frequency EEG. Stage 1 comprises light sleep with low-amplitude waveforms and slightly decreased frequency. Stage 2 is characterized by sleep spindles (higher-frequency waves around 11 Hz – 15 Hz) and K-complexes (graphically represented in (b)). Stages 3 and 4 comprise SWS with high-amplitude low-frequency waves. These four stages constitute NREM sleep. Another sleep stage is the REM sleep, which is associated with theta activity (4.5-7.5 Hz) and, as its name implies, is characterized by rapid eye movements (graphically represented in (c) by two horizontal EOG channels of the left and right eye). REM is also associated with low-amplitude sawtooth waves (not shown) and a higher level of consciousness. *Figure 2.1 (a) was reproduced by permission from Macmillan Publishers Ltd: Nature Reviews [67], copyright (2004).* Figure 2.1 (b) was reproduced from [59]

There are many theories which try to explain functions and the purpose of sleep. The main theories are: conservation of energy, restoration of tissue and

growth, thermoregulation, regulation of emotions, neuronal maturation, and memory and learning [59;70;71]. A full discussion of these theories goes beyond the scope of this thesis.

Memory and Hippocampus

Among the many functions attributed to sleep, its role in the memory consolidation is of particular importance as sleep may be required to redistribute and reactivate recent memory traces in the absence of interfering external inputs [71-74]. Whereas memory encoding and memory retrieval is bound to wakefulness, sleep has been postulated to promote memory consolidation. Consolidation refers to the process that transforms new and labile memories collected during wakefulness into a more stable cortical representation, making them integrated in networks of pre-existing long-term memories [75]. Human memory can be subdivided in declarative and nondeclarative memory. Declarative memory summarizes memories that are consciously accessible, such as fact and events (knowing “what”, e.g. “what is the capital of Brazil?”). Current neuronal models show the importance of the temporal lobe, including the hippocampus, in declarative memory formation. Nondeclarative memory includes the knowing “how” (procedural memory), for example actions, habits and skills (e.g. how to ride a bike); it is less dependent on medial temporal lobe structures [76]. Several studies support the idea that declarative, hippocampus-dependent memory is particularly strengthened by SWS, whereas nondeclarative, procedural memories benefit to a greater extent from REM sleep [77-79]. However, controversial results were also reported in which SWS can also improve nondeclarative, as well as REM sleep can improve declarative memory [80-82]. S2 has been associated with both kinds of memory consolidation [83-85]. Schabus et al. [86] measured spindle activity during S2 following a declarative memory task and a

control task. They found that increased S2 spindle activity was related to an increase in recall performance, reflecting memory consolidation. It is important to note that most memory tasks are neither purely declarative nor only procedural, and that both systems interact during sleep-dependent memory consolidation.

According to the standard model of memory consolidation at the systems-level, active cerebral communication transfers new memories, initially encoded in the hippocampus, into long-term memory representations stored in the neocortex [87-91]. Thus, remote memories are based on neocortical networks and can be retrieved independently of the hippocampus [92]. The (re-)activation of the hippocampus is reflected by hippocampal ripple activity that during sleep is found synchronized to sleep spindles [93; 94]. Thus, the hippocampus has been proposed to orchestrate the reactivation of memory traces and their reinstatement in cortical circuits [95]. The hippocampal-cortical system includes the hippocampal formation as well as its widespread cortical targets. The hippocampal formation (HF) consists of the Cornu ammonis (CA), dentate gyrus (DG), and subiculum (SUB) that are forming as a loop-like structure and are receiving and projecting information to the neocortex. This information flow is passing through the adjacent entorhinal cortex (EC) [96], see **Figure 2.2**. Next to the function of the HF related to memory processes, it has also been associated with spatial encoding, inhibition and anxiety [98;99]. Less clear is the precise connectivity of the hippocampus with the neocortex, not only anatomically but also in terms of effective functional connections. In this context, most knowledge stems from animal models [100;101].

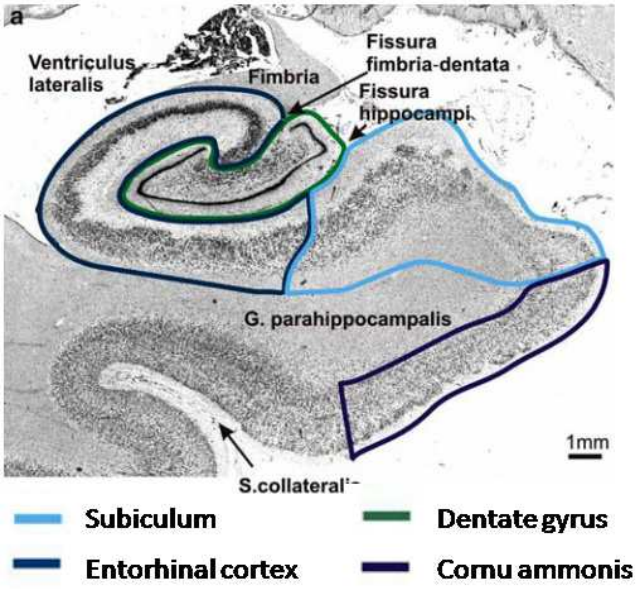

Figure 2.2. Cytoarchitecture of the mesial temporal lobe at the level of the body of the hippocampus. The hippocampal subregions and entorhinal cortex are displayed with different colors. ***Reproduced with kind permission from Springer Science+Business Media: Cytoarchitectonic mapping of the human amygdala, hippocampal region and entorhinal cortex: intersubject variability and probability maps, 2010, 2005, pag 345, K. Amunts et al, Fig. 2 [97].***

Resting-state

In fMRI, spontaneous signal fluctuations have recently been used to study functional cerebral connectivity [102]. Such signal fluctuations are organized in distinct functional resting-state networks (RSNs). As mentioned in **Chapter 1**, they are usually recorded in subjects asked to relax but not fall asleep in the scanner, with eyes closed. **Figure 2.3** exemplifies some of these RSNs.

Among the various RSNs, the “default mode” network (DMN) received particular attention, being linked to self-referential processes in humans, such as autobiographical memory and future envisioning [104]. During wakefulness it consists of subsystems in which the hippocampal formation and the lateral temporal cortex are involved in memory collection and building of associations, flexible use of this information to construct mental simulations, and integration of these processes

[96;104]. Also the posterior nodes of the DMN (posterior cingulate, precuneus, and inferior parietal lobules) correspond to regions involved in memory recollection [105].

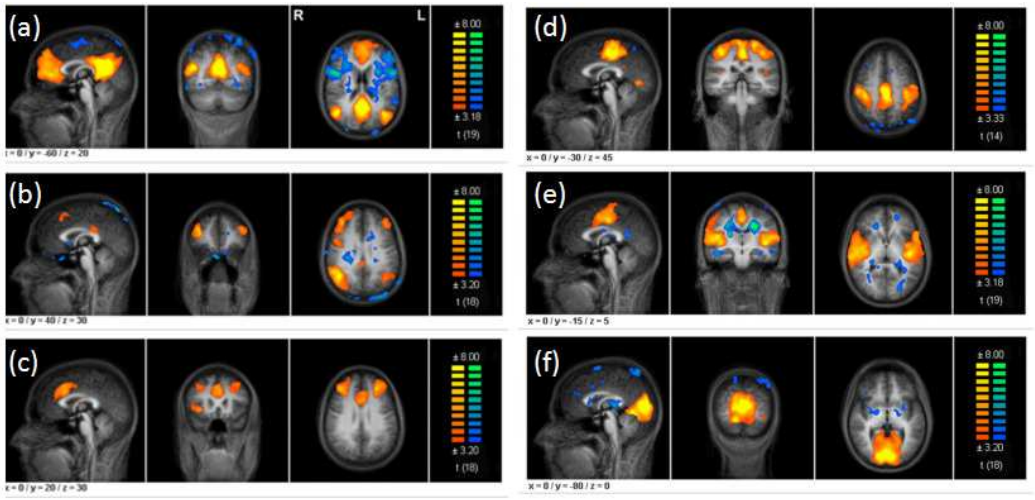

Figure 2.3. Different resting-state networks: RSNs were identified using ICA that decomposed the individual's fMRI into 30 statistically independent components (ICs), each delineating groups of voxels that exhibited synchronous temporal fluctuations. (a) "Default mode", (b) frontoparietal control, (c) frontal attention, (d) somato-motor, (e) auditory and (f) occipital visual network. Color bar depicts T-values. *RSNs taken with permission from Jann K, Kottlow M, Dierks T, Boesch C, Koenig T (2010) Topographic Electrophysiological Signatures of fMRI Resting State Networks. PLoS ONE 5(9): e12945, Fig 1 [103].*

Preserved DMN connectivity was reported in light sleep [106;107], while the DMN showed disintegration in slow wave sleep [107;108]. More subtle network changes, like a reduced contribution of the HF to the DMN, have also been shown at sleep onset [108]. However, as these studies focused on the DMN as a whole entity, it remains unclear if the HF builds up alternative functional connectivities with brain areas outside the DMN throughout the course of sleep.

Objective and hypotheses

The main goal of this work was to investigate the functional connectivity of the hippocampal subregions (CA, DG and SUB) to all other brain regions for wakefulness (W), and the NREM sleep stages 1 (S1), 2 (S2) and slow wave sleep (SWS), by means of simultaneous EEG/fMRI data collected during sleep.

The a priori hypotheses were:

1. The HF shows strongest functional connectivity to the major DMN nodes in wakefulness.

2. In stable sleep stages (S2 and SWS), different functional connectivity should be revealed. Based on the assumption of increased hippocampus-to-neocortex transfer, frontal and temporal brain regions should be more involved.

3. Functional connectivity changes during sleep are postulated to be associated with spindle activity as derived from concurrent EEG recordings, based on the assumed relation of hippocampal ripple and sleep spindle.

4. Regarding the role of hippocampal subregions (dentate gyrus and cornu ammonis) and the subiculum, we hypothesize especially enhanced functional connectivity of the hippocampal output region, the subiculum, during sleep.

Methods

Subjects

The study protocol was in accordance with the Declaration of Helsinki and was approved by the ethical review board of Ludwig-Maximilians University, Munich, Germany. Participants provided their written informed consent after the procedure had been fully explained and were reimbursed for their participation. Subjects underwent a general medical and structured psychiatric interview, clinical MRI and EEG to exclude clinical conditions that could interfere with the study protocol. Combined fMRI/polysomnography was obtained from 25 healthy adults (13 men, mean [SD] age 24.7 [3.2] years, 12 women, 24.8 [2.5] years). Participants were instructed to follow a regular sleep-wake-schedule with bedtimes between 23:00 and 08:00 hrs during the week prior to the experiment, documented by sleep diaries. Participants were asked to get up about three hours earlier on the experimental day to increase the probability of falling asleep in the MRI scanner. Wrist actigraphy during the night and day before the experiment was employed to control subjects' adherence to the sleep restriction. Simultaneous EEG/fMRI experiments started around 9:00 pm. After EEG montage and positioning in the MRI scanner subjects were informed that no further active participation was required during the following 2-3 hours, and that they could fall asleep.

FMRI and EEG acquisition

Simultaneous polysomnography comprised 19 EEG electrodes placed according to the international standard 10/20 system, electrooculogram, submental electromyography and an electrocardiogram (sampling rate 5 kHz; EasyCAP

modified for sleep, Herrsching, Germany; VisionRecorder Version 1.03, BrainProducts, Gilching, Germany). For noise protection subjects wore ear plugs and headphones. FMRI was carried out at 1.5 Tesla (Signa LX, GE, Milwaukee, USA) using an 8-channel head coil.

One fMRI run consisted of 800 functional whole brain images (EPI; repetition time 2000 ms; echo time 40 ms; flip angle 90°; 64 × 64 matrix, in-plane resolution 3.4 × 3.4 mm^2; slices 25; slice thickness 3 mm; gap 1 mm; oriented along AC-PC) acquired over 26.7 minutes. This time restriction originated in a scanner software limitation to continuous acquisition of 20000 slices at maximum. To allow for vigilance monitoring during the recording session, the sleep stages were determined online using the real-time gradient EEG artifact correction of the Vision Recorder (Version 1.03.0003) and Vision RecView (Version 1.0) software (Brain Products, Gilching, Germany). If the subject was not able to fall asleep, only reached light NREM sleep stages or showed an early and rapid transition to S2 and SWS during the first run, acquisition was repeated to increase the probability of recording the missing sleep stages. In total, 40 fMRI runs of each 26.7 minutes length were acquired from 25 subjects.

Sleep stage rating

EEG preprocessing was performed using Brain Vision Analyzer software 1.05 (Brain Products, Gilching, Germany). Correction of MRI related EEG artifact was performed by subtraction of an adaptive template based on artifact averages of 8 consecutives MRI volumes. Independent component analysis was applied for removal of ECG and EOG artifacts. Components with strong ECG and EOG related time courses were visually identified and removed (see **Chapter 1** for more details

about EEG artifact correction). Data were resampled to 250 Hz, re-referenced against linked mastoids and filtered (0.1 Hz to 30 Hz). Sleep stage scoring following Rechtschaffen and Kales [57] criteria of all 40 fMRI runs was performed in 20 second windows. The hypnograms of the 40 recorded 26.7-minute sessions were then screened for intervals consisting of 5 minutes of one specific, stable sleep stage (due to some waxing and waning of sleep defined by presence of more than 85% throughout the epoch), without arousals or movement artifacts in either EEG or fMRI. This resulted in 93 epochs of the following vigilance stages: wakefulness (W: 27), sleep stage 1 (S1: 24), sleep stage 2 (S2: 24), and slow wave sleep (SW: 18).

FMRI analysis

1. Preprocessing: All fMRI analyses were performed in 64-bit Linux workstations using SPM, version 5 (www.fil.ion.ucl.ac.uk/spm), and in-house scripts programmed in IDL version 6.3 (www.ittvis.com) and Matlab version 2008B (The MathWorks, Natick, USA). The fMRI preprocessing steps consisted of: 1) slice time correction to account for different acquisition times between slices; 2) realignment using rigid body transformation to correct for head motion. Data with head movements more than 2 mm were excluded; 3) spatial normalization of the images to a standard EPI template in MNI space (SPM5 distribution) and interpolation to a voxel resolution of 2 × 2 × 2 mm^3 using 5th degree splines (see **Chapter 1** for fMRI preprocessing details).

2. Removal of artificial signals: To remove artificial components and signal contributions of non-neural origin from the time courses, spatially normalized and unsmoothed images were residualized by multiple regression analysis in the GLM framework against the following regressors: (i-vi) six parameters derived from the

motion correction step (matrixes $\vec{R}$ and $\vec{T}$), (vii-xii) their respective first order derivatives, (xiii-xiv) the averaged time series of the white matter and CSF voxels, (xv-xvi) and their respective first order derivatives. They resultant in residual images contained signal fluctuations not explained by regressors i–xvi. They were temporally (lowpass filter of 0.1 Hz in FSL 3.2 (www.fmrib.ox.ac.uk/fsl)) and spatially (isotropic Gaussian kernel, full width half maximum of 6 mm) filtered and afterwards used for extraction of region-based time courses.

The 0.1 Hz lowpass filtering was used to restrict analysis to the typical frequency range generally used to study resting-state network fluctuations due to the expected functional connectivity of the hippocampus and DMN. Such restriction may shadow possible higher frequency contributions to spontaneous signal fluctuation. To test for the effect of lowpass filtering, the analysis has also been performed without filtering (results not shown), leading to the same quantitative results. However, physiological noise contributes much more to the later analysis, and therefore the lowpass filtered data was in the focus of this work.

3. Fixed effects model: For each subject and sleep stage, data were regressed to the corresponding hippocampal time courses. Subregions of the hippocampal formation were defined from probabilistic cytoarchitectonic maps as previously described [97] (**Figure 2.4**) and implemented in the SPM anatomy toolbox [109]. Time courses were calculated as the mean signal of all voxels inside the specific region, and extracted using the Marsbar toolbox [110] for SPM. The following hippocampal subregions were used: Cornu ammonis (CA), dentate gyrus (DG), and subiculum (SUB). For every subject and sleep stage, each time course of the bilateral subregion was regressed on the residual fMRI images in three separate fixed effects analyses.

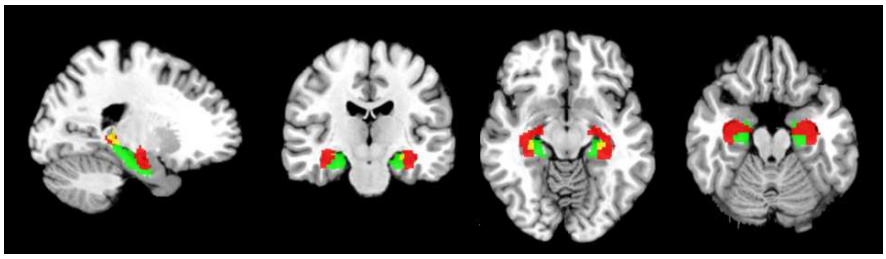

Figure 2.4. Probabilistic cytoarchitectonic maps of the hippocampal subregions and subiculum as previously described in [97]. Red - cornu ammonis, yellow - dentate gyrus and green – subiculum.

4. Random effects model: For analysing sleep stage influences, a second level random effects analysis was performed using a two-factorial design (factor *subregion*: three subregions, factor *sleep*: wakefulness and three NREM sleep stages). A map of the HF functional connectivity during wakefulness was generated by a t-test against zero combining all subregions. Effects of factor *sleep* and of factor *subregion* were tested using analysis of variance (ANOVA). Directed t-tests were performed in addition to explore the direction of the effects (W vs S1, W vs S2, W vs SWS, S1 vs S2, S1 vs SWS, and S2 vs SWS). Finally, specific subregional contributions were identified per sleep stage by contrasting each subregion against the two other subregions combined.

The functional connectivity map collected during wakefulness was thresholded at $p_{FWE}<10^{-6}$, extent > 150 voxels. For the main effects of factors *sleep* and *subregion*, for the bidirectional sleep stage comparison as well as for the subregional analyses, an uncorrected threshold was set at $p<0.001$, with varying cluster extent in order to ensure significance of the resulting clusters under consideration of non-stationary smoothness ($p_{FWE,cluster}<0.05$) [111].

Sleep spindle analysis

Analysis of sleep spindles and related fMRI activation was based on the procedures described in Schabus et al. [64]. In the EEG data of the selected epochs in sleep stage 2, occurrence of slow and fast sleep spindles was determined after band-pass filtering of 11 - 13 Hz (0.0145 s, 48 dB/oct) and 13 - 15 Hz (0.0122 s, 48 dB/oct), respectively. The root mean square (rms) of the filtered signal was calculated in time windows of 200 ms. For slow spindles, EEG data collected at electrode Fz were used, as slow spindles are known to be strongest over frontal brain regions, while for fast spindles (with parietal dominance) Pz was used [112]. For both spindle types, the 20% highest rms amplitudes were classified as spindles. Finally, onset of the classified spindles were used to construct the event regressor and later convolved with the three basis canonical function (hemodynamic response function, its time and dispersion derivatives). As in Schabus et al. [64] the power fluctuation in the EEG delta band (0.5 – 4 Hz) was added as a covariate, as spindles are modulated by slow-waves. For this purpose, we extracted the delta power from Fz per fMRI volume using Fast-Fourier Transform (FFT, resolution = 0.5 Hz, Hanning window 10%), and convolved it with the hemodynamic response function. For each subject, the event regressors of fast and slow spindles convolved with the three basis canonical functions along with delta power were regressed against the residual fMRI images in a fixed effects model.

Second level analysis was performed using the individual t-contrasts of each of the three canonical basis functions as well as of the two spindle types as factors. The error covariance was not assumed independent between regressors and a correction for non-sphericity was applied [113]. The resulting maps were collected at $p_{uncorr} < 0.001$, extent > 135 voxels, signifying $p_{FWE,cluster} < 0.05$ [111].

Psychophysiological interaction analysis

Psychophysiological interactions (PPI), refers to a method relating the functional coupling between one area and the rest of the brain to results of psychological tests. Here, as external variable an electrophysiological, not psychophysiological means was applied, however recorded simultaneously and using the same methodological approach. PPIs between the EEG spindle data and the BOLD signal time courses of the three HF subregions were evaluated in order to test if changes in HF functional connectivity had an interaction with increased spindle activity. PPIs were performed for CA, DG and SUB in three distinct analyses. For each subregion, first, the neuronal representation of the signal time course of the subregion was approximated by deconvoluting the HRF from it. Second, the neural representation of the fMRI signal time course was convolved with the individual event regressor containing the onset time points of spindles (also one analysis for each spindle type, slow and fast spindle) and afterwards convolved with the HRF. The regressor which resulted from this transformation and the two original regressors before the convolution (fMRI signal time course of the subregion and HRF folded event regressor containing the onset time points of spindles) were entered in a fixed effect analysis. Analysis was performed on the residualized data as described above. Data were thresholded at $p_{uncorr}<10^{-4}$, extent $k>150$, $p_{FWE,cluster} < 0.005$.

Results

Subjects adhered to the experimental guidelines and sleep restriction, as shown by sleep diaries and wrist actigraphy. Sleep latency (time until first appearance of S2), only considering the first attempt of the subject to fall asleep, was 6.7 ± 4.9 minutes. Over all 40 fMRI runs, the average time spent in W, S1, S2 and SWS were 6.8 ± 5.2 minutes, 5.9 ± 4.2 minutes, 10.0 ± 5.4 minutes and 4.8 ± 5.8 minutes, respectively. Eventually, a closer inspection of hypnograms identified 93 epochs (27, 24, 24 and 18 epochs of W, S1, S2 and SWS of 15, 18, 10 and 11 subjects) of each five contiguous minutes with a single dominating vigilance stage, i.e. less than 14 % of time spent in flanking sleep stages and without arousals. Assignment of all 5-minute epochs to subjects and runs including a description of the prevalence of the different sleep stages per run is detailed elsewhere [114]. Occurrence of REM sleep was not observed, which is not unexpected as data were obtained only from the initial part of the sleep cycle and REM sleep is suppressed in the noisy MR environment [63]. During later processing, one data set acquired during S1 was found to be corrupted and excluded.

Sleep stage and HF functional connectivity

Figure 2.5a shows the functional connectivity map for HF during wakefulness. HF is functionally connected, amongst others, to the major nodes of the DMN, namely the posterior cingulate cortex/retrosplenial cortex (PCC/RspC), medial prefrontal cortex (mPFC), bilateral inferior parietal lobule (IPL) and bilateral middle and superior temporal gyrus, as well as the thalamus (**Table A2.1**, **Appendix A2**). The HF formation is most strongly connected to the DMN during wakefulness, with

gradually decreasing functional connectivity with the DMN in NREM sleep stages, as illustrated in **Figure 2.5b** for the DMN core regions.

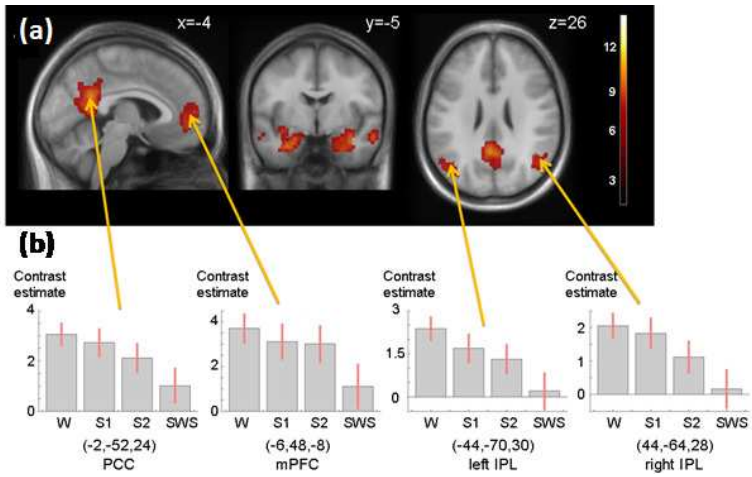

Figure 2.5. (a) Extension of the HF network during wakefulness. Positive functional connectivity of DMN nodes and the HF is shown ($p_{FWE}<10^{-6}$, extent>150 voxel). Color coding indicates T-values. MNI coordinates of each slice are given. (b) Contrast estimates ± SD, deviations extracted at the peak voxel of the indicated cluster and separated for each sleep stage (wakefulness: W; sleep stages 1 and 2: S1/S2; slow wave sleep: SWS), are shown. MNI coordinates (x,y,z) of the cluster peak voxel are provided. PCC: Posterior cingulate gyrus; mPFC: Medial prefrontal gyrus; IPL: Inferior parietal lobule.

To further examine sleep stage specific alterations in HF functional connectivity, an F-test was performed on the factor *sleep* (**Figure 2.6**).

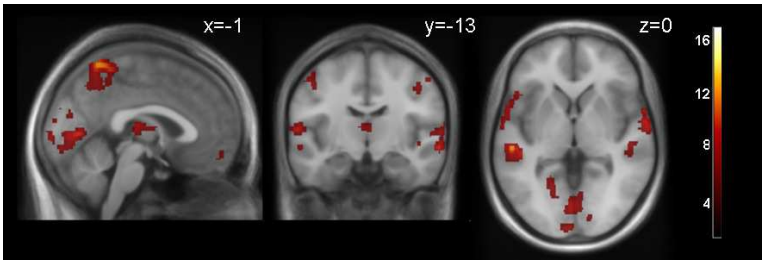

Figure 2.6. Results of the full-factorial design employing factors *sleep stage* and *subregion*. F-test showing the main effect of *sleep*. Data are thresholded at $p_{FWE,cluster}<0.05$ using a collection threshold of p<0.001. Note that the HF has not been masked out. MNI coordinates of each slice are given. Color bar depicts t-values.

Figure 2.7 Shows the directed t-tests performed to explore the direction of the changes comparing wakefulness against all NREM sleep stages, as well as for the comparison between S2 and SWS (**Table A2.2**, **Appendix A2**). Comparing wakefulness with S1, only the thalamus showed higher functional connectivity with the HF during wakefulness. During S1, functional connectivity of the HF was generally found to be stronger in the middle and superior temporal gyrus, occipital cortex and inferior parietal lobule (**Figure 2.7a**). During S2, HF functional connectivity to the lateral temporal and the occipital cortex further increased as compared with wakefulness, while no differences in thalamic connectivity were visible. In addition, during S2 functional connectivity of the HF with the cingulate cortex and superior temporal gyrus were higher compared to wakefulness (**Figure 2.7b**). In the comparison between wakefulness and SWS (**Figure 2.7c**), functional connectivity of the bilateral IPL, PCC and mPFC with the HF was stronger in wakefulness, indicating a sleep stage dependent decrease in the integration of the HF to the DMN. No regions exhibited stronger functional connectivity with the HF during SWS than wakefulness. The comparison between S2 and SWS (**Figure 2.7d**) revealed stronger HF connectivity to occipital, lateral temporal and inferior frontal regions in S2. No clusters were detected that showed higher functional connectivity during SWS compared with S2.

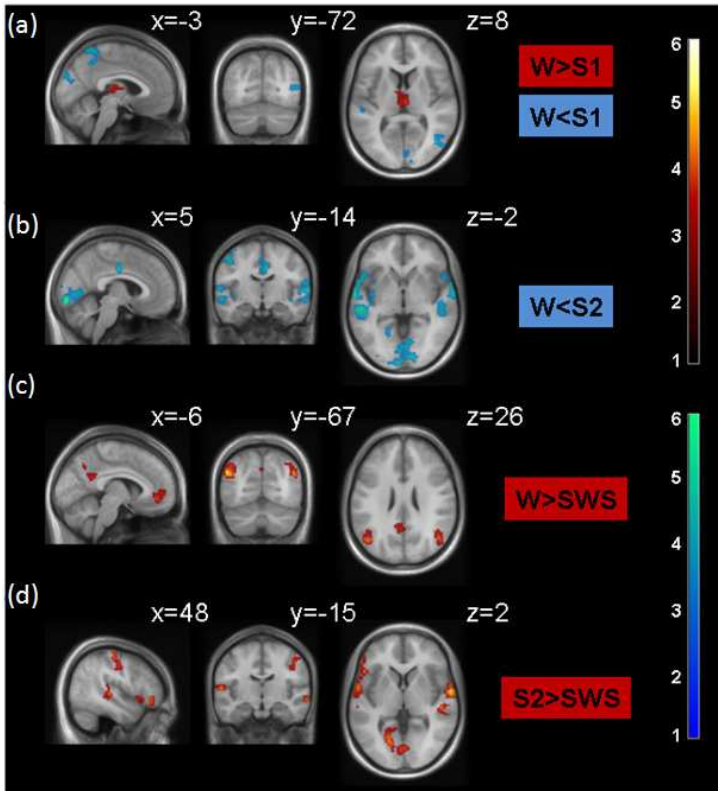

Figure 2.7. Comparison of HF functional connectivity across sleep stages. Wakefulness: W; sleep stages 1 and 2: S1/S2; slow wave sleep: SWS. Data are thresholded at $p_{uncorr}<0.001$, with a variable voxel extent, resulting in $p_{FWE,cluster}<0.05$ (see Table A2.2, appendix A2). Color coding indicates t-values. The HF has been masked out to avoid display of autocorrelations. MNI coordinates of each slice are given.

Subregions analysis

We further tested specific functional connectivity of three HF subregions across sleep stages. An F-test on the main effect of *subregion* revealed wide-spread differences in functional connectivity among subregions (**Figure 2.8**).

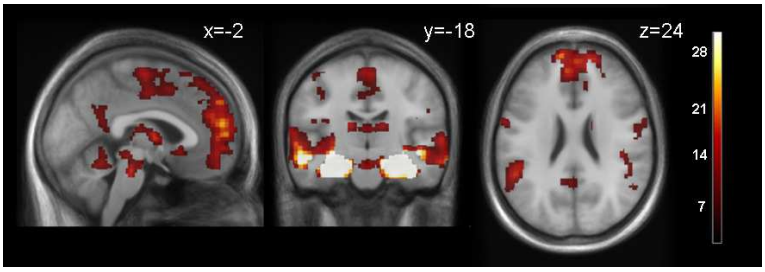

Figure 2.8. Results of the full-factorial design employing factor *sleep stage* and *subregion*. F-test showing main effects of *subregion*. Data are thresholded at $p_{FWE,cluster}<0.05$ using a

collection threshold of p<0.001. Note that the HF has not been masked out. MNI coordinates of each slice are given. Color bars depict t-values.

Post-hoc t-tests (**Figures 2.9** and **Table A2.3**, **Appendix A2**) showed that during wakefulness, functional connectivity of the CA was most robust to the IPL, the midline nodes of the DMN, and the thalamus. The functional connectivity with the lateral temporal cortex appears to be strongest for the CA in wakefulness and all NREM sleep stages. In S1, CA showed unique functional connectivity to the primary motor cortex. In sleep stage S2, SUB revealed strongest functional connectivity to the anterior cingulate cortex (ACC)/mPFC. Finally, in SWS, the DG showed unique functional connectivity to the occipital cortex, while SUB was most connected with the motor cortex.

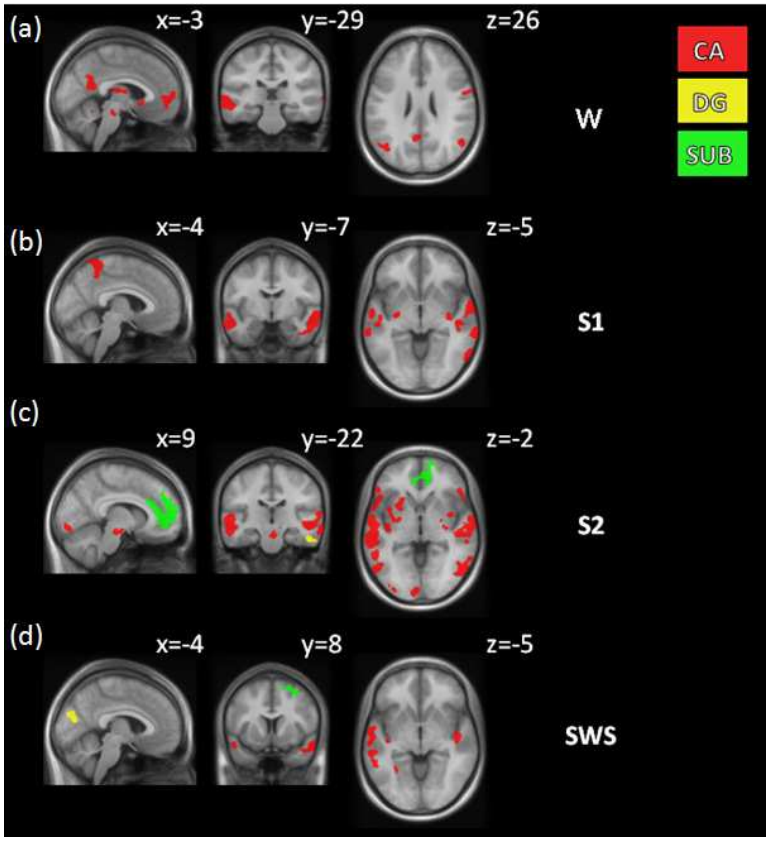

Figure 2.9. Comparison of subregional HF functional connectivity contribution within sleep stages. For each sleep stage, strongest contributions of each hippocampal subregion are depicted (yellow: dentate gyrus (DG), red: cornu ammonis (CA), green: subiculum (SUB)). (a)

Wakefulness (W); (b) sleep stage 1 (S1); (c) sleep stage 2 (S2); (d) slow wave sleep (SWS). Data are thresholded at $p_{FWE,cluster}$<0.05 using a collection threshold of p<0.001 (see Table A2.3, appendix A2). The HF has been masked out to avoid display of autocorrelations. MNI coordinates of each slice are given.

Sleep spindles

Further, Activation maps related to sleep spindle activity in sleep stage 2, differentiating between slow and fast spindles were generated. The basic pattern reported by Schabus and colleagues [64] for fast spindles, with major clusters in the right thalamus, insula, lateral temporal cortex, cingulate cortex and motor areas could be reproduced (**Figure 2.10** and **Table A2.4**, **Appendix A2**). Notably, no spindle specific activation was found in the HF, in accordance with the previous report. However, we observed a strong overlap between the HF functional connectivity map (contrast S2>W; **Figure 2.7**) and the network associated with fast spindles. Neither significant positive or negative correlations with slow spindles, nor negative correlations with fast spindles were observed.

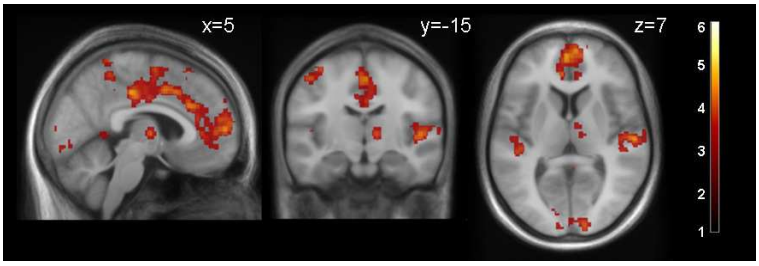

Figure 2.10. Activity related to fast sleep spindles in S2 ($p_{FWE,cluster}$ < 0.05, collection threshold p<0.001). Color bar depicts T-values. Note that the HF is not part of the spindle network. MNI coordinates of each slice are given.

In order to investigate if observed increases in hippocampal functional connectivity during S2 compared with wakefulness are associated with spindle activity in the EEG data, PPI analyses separately for the three hippocampal

subregions within S2 were performed. Functional connectivity of the subiculum increased in parallel with EEG spindle activity (**Figure 2.11, Table A2.5, Appendix A2**) in a network comprising the cingulate cortex, lateral temporal cortex, motor cortex, SMA, and insular cortex. Spatially similar, yet less strong spindle-associated functional connectivity increases were found for the CA and DG bound network (**Table A2.6** and **A2.7**, **Appendix A2**).

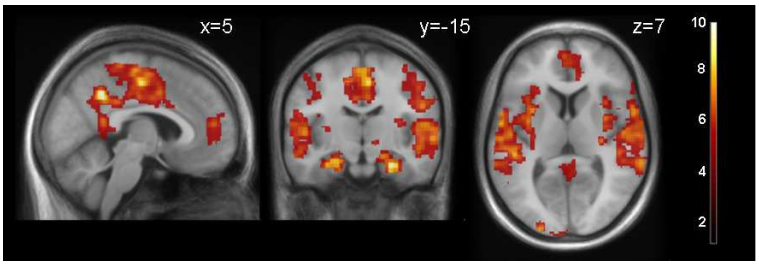

Figure 2.11. PPI analysis for the interaction *spindles x SUB* (hot colors, $p_{uncorr}<10^{-4}$, extent>150 voxel). Color coding indicates t-values. MNI coordinates of each slice are given.

Discussion

The present data demonstrate altered functional connectivity of the hippocampal formation across NREM sleep stages compared with the waking state. The previously reported integration of the hippocampal formation into the DMN during wakefulness was confirmed. During sleep stage 2, the HF was more strongly connected with the temporal, insular, occipital and cingulate cortices than during wakefulness or slow wave sleep. Spindle related activity overlapped with the HF connectivity map (contrasting sleep stage 2 with wakefulness). Especially the connectivity pattern of the subiculum to frontal, lateral temporal, and motor cortical regions and to the insula showed a strong interaction with occurrence of sleep spindles.

HF connectivity to the DMN in wakefulness and sleep

Contribution of the HF to the DMN has been reported earlier [104;105]. Possible functions of the DMN include internal mentation and autobiographic memory retrieval: In a meta-analysis of autobiographical memory tasks, the HF, mPFC and RspC have been found to be robustly co-activated [115]. Similarly, episodic memory retrieval is related to activation in the lateral posterior parietal cortex and the precuneus extending into PCC/RspC [116]. Burianova et al. [117] showed that a common neural network including major DMN nodes underlies the retrieval of declarative memories during wakefulness, independent of specific memory content. Recently, Andrews-Hanna et al. [118] showed that the DMN is comprised of two interacting subsystems, linked by a common midline core (PCC; mPFC). One of these subsystems, the medial temporal lobe subsystem, which includes the HF and

the IPL, is particularly engaged during construction of mental scenes based on memory. Taken together, these reports showed that the functional connectivity of the hippocampus and the DMN conjointly constitute a network pivotal for episodic memory retrieval during wakefulness.

Only a trend for reduced coupling of the HF to the DMN in light sleep stages was observed. In contrast, slow wave sleep was characterized by a robust decrease in functional coupling between the HF and the DMN. This breakdown of functional connectivity between the HF and DMN occurred in all core nodes of the DMN (PCC, mPFC, bilateral IPL). Reduced connectivity between the anterior and the posterior DMN nodes in SWS have been reported before [107;108], although the posterior nodes (PCC, IPL) seemed to increase their connectivity [107]. Here, these findings were extended by demonstrating that the breakdown of connectivity within the DMN also comprises the HF. Reduced functional connectivity of the hippocampus to core DMN nodes (PCC, IPL) has also been reported for subjects under anaesthesia [119], which may point towards a common neural basis for behavioural similarities during these stages.

HF connectivity to neocortex generally higher in S2 than in SW

The present data showed that functional connectivity of HF with neocortical regions was higher in S2 than in SWS or wakefulness. This indicates functionally distinct processes during sleep: increased connectivity between HF and neocortical regions in S2 suggests an increased capacity for possible information transfer, whereas decreased connectivity between these regions in SWS suggests a functional system optimal for segregated reprocessing. These findings may be relevant for the memory consolidation hypothesis of sleep [75;76], and may inform during which NREM sleep stages memory transfer and reprocessing could occur.

Several studies stress the relevance of SWS for memory consolidation [73;78;85;120;121]. However, there are reports that S2 may in fact play an equally important role [86;93;122-124]. Furthermore, some data on the relevance of sleep EEG macro-structure for memory consolidation are derived from animal models, in which NREM sleep is usually not divided into substages [125]. Hence it is not unambiguously clear, how, within NREM sleep, S2 and SWS differentially relate to the hippocampal-neocortical dialogue proposed to underlie sleep-related memory consolidation. Functional connectivity analyses may help to dissect such sleep stage specific contributions.

The analysis of subregional contributions to the HF network revealed that the CA region is driving the functional connectivity with the core DMN nodes (PCC/RspC, IPL, mPFC) during wakefulness and to the lateral temporal cortex in all sleep stages. In contrast, mPFC functional connectivity is dominated by the subiculum in S2. In a series of elegant fMRI studies, sleep has been shown to alter the hippocampal-neocortical interplay, e.g. with the mPFC, underlying memory retrieval [92;126-131]. The classical model of memory consolidation suggests that information is propagating from the neocortex to the hippocampus in the waking state while being reversed in sleep, e.g. [90], however, a recent study showed more bidirectional coupling with increased influence of neocortical regions onto the HF towards deeper sleep stages [132]. The present data don’t allow commenting on the direction of such information propagation due to intrinsic limitations of functional connectivity analysis. Still, the strong involvement of the subiculum as the major hippocampal output region in S2 may suggest a hippocampal-to-neocortical information transfer.

Increased HF connectivity in S2 interacts with sleep spindles

The data reveal that the connectivity between HF and neocortex showed a strong interaction with fast sleep spindles, which was most pronounced for functional connectivity between the subiculum and the lateral temporal, insular, cingulate and medial prefrontal cortices. Interestingly there was no significant activation of the HF in direct association with occurrence of either fast or slow spindles (**Figure 2.10**) in accordance with Schabus et al. [64]. This suggests that spindle activity may enhance functional connectivity between the HF and neocortical regions, but that it is not the sole cause of such connectivity. Temporal coupling between spindles, hippocampal ripples and slow-oscillations has been described before in that during the up-state of cortical slow oscillations, both spindle activity and hippocampal high-frequency ripple activity were increased [133;134]. The coordinated spindle–ripple events have been suggested to provide a mechanism for information transfer between hippocampus and neocortex [94;133;135], which could explain that sleep spindles, most pronounced in S2 but also occurring in SWS [112] are related to memory consolidation [86;122;123;136-138]. At the same time, sleep spindles have been shown to reflect thalamus-driven cortical inhibition, which may signify a different or double functionality [65;66].

Connectivity between the thalamus and HF was reduced in S1. This thalamic cluster was located in the nonspecific midline nucleus, known to send input to the hippocampal formation [139;140]. The finding of reduced HF/thalamus functional connectivity is in line with earlier observations of thalamic deactivation at sleep onset [10] and with generally reduced thalamic functional connectivity to most cortical brain regions in S1 [114].

Limitations

While the present data provided evidence for generally increased HF functional connectivity in S2 and a relation of the hippocampal functional network and sleep spindles, one cannot conclusively state a direct link to memory related processes. Future studies will need to compare HF functional connectivity in S2 with successful post-sleep memory recall after intervention, as has been demonstrated in wakefulness [88;92]. Alternative functional interpretations, such as synaptic downscaling [70;141] should also be considered in future experiments.

Conclusion

The present analysis revealed important reorganization of the spontaneous HF connectivity during NREM sleep. Especially during sleep stage 2 and linked to sleep spindle activity, synchronous activation with lateral temporal, cingulate and frontal regions arises which may represent coordinated neural activity within the memory network. As fMRI functional connectivity allows tracking of memory transfer in wakefulness, these altered functional connectivity patterns likely reflect differences in information processing, and possibly in sleep specific plasticity processes.

CHAPTER 3

Recurrence quantification analysis allows for single-trial stimulus differentiation in evoked potential studies

Introduction

Event related potential (ERP) studies investigate specific deflections in electroencephalographic recordings associated with a given stimulus. For example, an auditory oddball experiment consists of a sequential presentation of tones in which frequent tones (presented at one pitch) are interspersed with rarely occurring 'odd' tones (also referred to as rare tones, presented at a different, e. g. a higher pitch) (**Figure 3.1**). This experiment typically elicits the ERP components N100, P200 and P300. N (negative) or P (positive) describes the observed polarity of the evoked signal, and the number the typical time of its occurrence after the stimulus onset. The P300 deflection represents aspects of cognitive processing such as attention, novelty detection and memory updating and has been extensively described in the literature [142-144]. The P300 amplitude as obtained from averaged individual ERPs is inversely proportional to the frequency of the tones' appearance [142;145] which allows for differentiation of the neural response to frequent and rare tones. The N100 and P200 deflections are related to perceptual processing and are dependent on the subject's attention level [146;147]. N100/P200 are further reflecting physical tone characteristics like pitch and loudness.

ERPs are usually lower in amplitude compared with the EEG background signal. Therefore, ERPs are usually averaged over several trials to reduce the contribution of random EEG background activity, and to increase the signal-to-noise ratio.

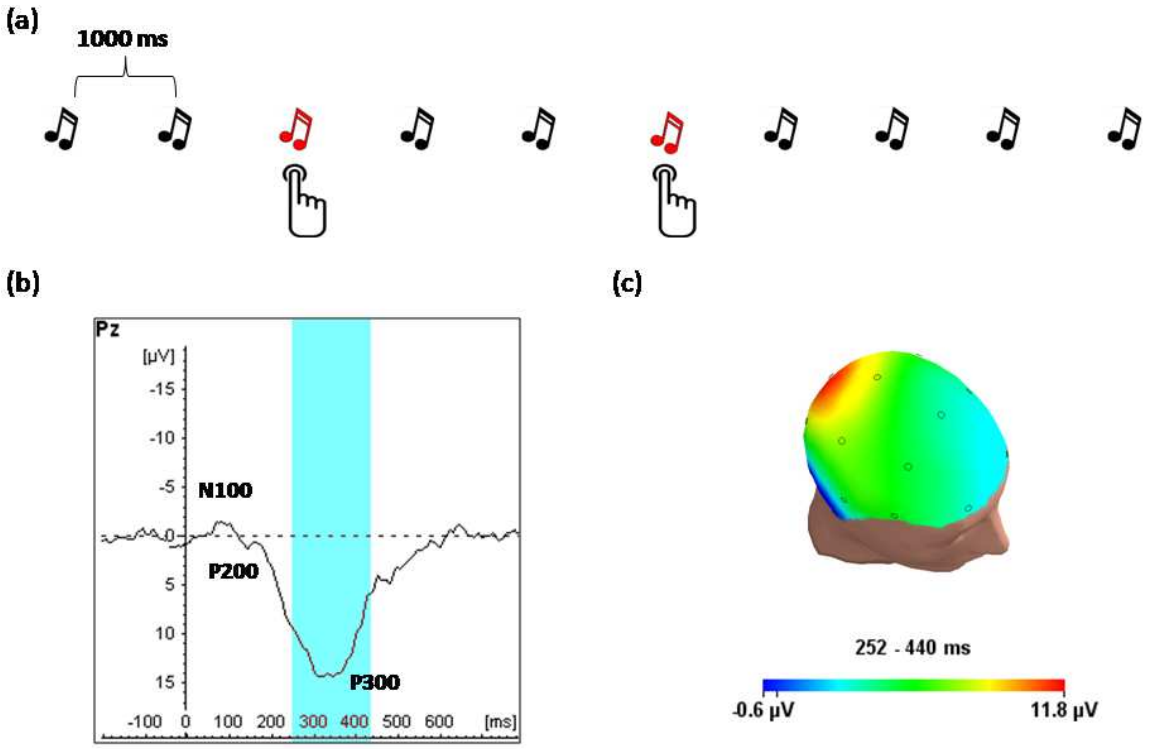

Figure 3.1. Active auditory oddball experiment. (a) Frequent tones (black) intercalated by rare (red) tones with inter-stimulus interval (ISI) of 1000 ms. The subject was asked to press a response button every time he detected a rare tone. (b) ERP response to rare tone displaying N100, P200 and P300 peaks. (c) Topographic map from the blue time window in (b).

Such averaging intrinsically assumes that the electrophysiological responses are similar for all stimuli with the same physical characteristics, i.e. that all ERPs are stationary. This assumption, however, does not necessarily hold true for physiological data. Individual responses to stimuli depend on levels of attention, habituation, vigilance and other factors [145;148-151] and averaging does not account for such potentially meaningful trial-by-trial variance. Furthermore, averaging methods collapse single events which are gathered over an extended period of time (several minutes). This may affect, for example, simultaneous ERP/fMRI analyses, in which correlation of each single ERP with its corresponding fMRI volume is required.

Therefore, particularly for event-related fMRI analysis, methods are sought that allow for a robust quantification of the electrophysiological response to a single trial.

Several research groups have reported advanced methods to detect minute changes in the ERP of a single trial. Bénar et al. [152] were able to track the P300 response changes in an EEG/fMRI oddball experiment applying narrow filters in the EEG data. Similarly, independent component analysis (ICA) and wavelet denoising have been proposed to improve trial-by-trial analysis [153-157]. However, all these approaches have their specific advantages and limitations, and no standard method for single trial analysis has yet been established [158].

Recurrence quantification analysis (RQA) is a method able to detect linear and nonlinear signal changes proposed by Zbilut and Webber [159]. It does not require any specific assumptions about the statistical properties of the data. In contrast to other non-linear methods, RQA can also be applied to relatively short non-stationary time series [160]. Carrubba et al. [161-163] compared the classical method of time averaging and recurrence analysis to detect magnetic evoked potential. They reported that these potentials were better detected by RQA than by the averaging method. Schinkel et al. [164] investigated ERP response to semantic mismatch, known to evoke a N400 deflection: On a trial-by-trial level, they compared the sensitivity of the ERP amplitude analysis with RQA and showed that RQA was more sensitive in detecting semantic mismatch. Marwan and Meinke [165] demonstrated that RQA could also be used to analyze single-trial ERPs in an auditory oddball paradigm, however, no group analyses were presented.

The MR induced artifacts in the EEG, caused by the static magnetic field and by rapidly switching magnetic field gradient, make the potential combination of single-

trial EEG and fMRI even more challenging (**Chapter 1**). Until now no work was done to probe RQA in simultaneous EEG/fMRI.

Objective

The goal of this study was to test the reliability of RQA to characterize single trial ERPs recorded under normal experimental conditions as well as under the influence of MR artifacts, and to compare the results with ERP amplitude analysis. Furthermore, we set out to extend previous reports from an individual subject level to the level of group analysis, allowing for statistical testing.

Approach

A classical auditory oddball experiment was used to compare the performance of RQA with the performance of amplitude analysis of ERPs. Specifically, RQA was compared to standard ERP amplitude analysis with respect to their potential to distinguish between frequent and rare tones. Second, these methods were compared with respect to their power to distinguish between frequent tones positioned before and after a rare tone, as the appearance of a rare tone may change the context of the experimental background. Last, for a preparation of combined fMRI/EEG analysis, the robustness of RQA and amplitude analysis towards experimental noise in the raw data was investigated. For this purpose, EEG data were recorded under standard laboratory conditions as well as during MRI acquisition.

Methods

Subjects

Eleven right-handed healthy subjects (7 men, 4 women; mean age 27.8 ± 2.8 years) were recruited by public advertisements. They underwent a diagnostic interview to exclude any neurological, psychiatric or medical condition which could prohibit participation in the study, and to exclude any contraindication for MRI. The study protocol followed the guidelines of the Declaration of Helsinki and was approved by the local ethical committee. All subjects gave their written informed consent and were paid for their participation. Data of two subjects were excluded due to strong movement artifacts, leaving nine subjects for final analysis.

Experimental task

Subjects performed two sessions of an active auditory oddball paradigm [166-168], outside and inside the MR scanner, on the same day. Presentation software (Neurobehavioral Systems, Albany, USA) was used for task programming and stimulus delivery. Each section consisted of the presentation of two types of tones: A rare tone (1.4 kHz, duration 100 ms including 10 ms rise and fall times) and a frequent tone (1 kHz, duration 100 ms including 10 ms rise and fall times) that may be considered the auditory background pattern. The order of the tones was randomly assigned, with two consecutive rare tones always being separated by at least two frequent tones. The overall frequency of appearance was 90% for frequent and 10% for rare tones. This distribution criterion had to be fulfilled for all subsets of 20 tones. The inter-stimulus interval (ISI) was 1 s with jittering of ± 250 ms. For each section a

total of 600 tones were presented over 15 minutes. Tone stimuli were presented via headphones, and subjects wore ear plugs as a safety requirement during MR measurements. All subjects participated in an MR test session to become acquainted to the MR environment prior to the actual experiment. To adjust loudness of the auditory stimuli, a preparation scan was performed during which subjects had to repeatedly decide whether or not they perceived the tones as loud as the fMRI scanner sound. This resulted in a defined level of subjectively identical loudness of tones and scanner noise. For the final experiment, tones were delivered 3 dB louder for better perception (within an absolute range of 80 – 85 dB). Subjects were instructed to keep the eyes open in order to reduce EEG alpha activity, and to press a button with their right index finger as fast and accurately as possible every time they detected a rare tone.

MRI data acquisition

In the simultaneous EEG/MRI experiments, each subject was positioned inside the MR scanner in a supine position with the head carefully immobilized to minimize movement artifacts. Experiments were performed on a 1.5 Tesla clinical scanner (Signa Echospeed, General Electric, Milwaukee, Wisconsin, USA) using an 8-channel headcoil. Functional T2*-weighted echoplanar images (EPI) of the whole head (342 volumes) were obtained with 25 slices and an image matrix size 64 × 64 (single shot EPI, TR = 2 s, TE = 40 ms, resolution of 3.44 × 3.44 × 4 mm^3, FOV = 22 × 22 cm^2). Slice orientation was parallel to the anterior/posterior commissure.

EEG acquisition and preprocessing

EEG acquisition was performed at a sampling rate of 5 kHz using an MR-compatible system (Brain Products, EasyCap, Herrsching-Breitbrunn, Germany) with 19 electrodes positioned according to the 10-20 system referenced against FCz. In addition, EMG, EOG and ECG were acquired and used for artifact correction. All precautions to guarantee a safe recording of the electrophysiological signals during image acquisition were taken [39]. EEG preprocessing was performed using Brain Vision Analyzer software 1.05 (Brain Products, Gilching, Germany). Correction of MRI related EEG artifact was performed by subtraction of an adaptive template based on artifact averages of eight consecutive MRI volumes. Independent component analysis was applied for removal of ECG and EOG artifacts. Components with strong ECG and EOG related time courses were visually identified and removed. Data were resampled to 250 Hz, re-referenced against linked mastoids and filtered (0.1 Hz to 30 Hz) (see **Chapter 1** for more details about EEG preprocessing). Similar to Benár et al. [152], an additional filter to decrease the power of the EEG alpha band was applied. For this purpose, a high frequency cut-off of 10 Hz was used, mainly reducing alpha components in the range 10-12 Hz, but retaining the lower frequency range containing the individual ERPs. Finally, the EEG was segmented according to each tone stimulus, using a time window of 200 ms prior to tone onset to 800 ms after tone onset (-200 ms to +800 ms), DC detrended and corrected for different baseline levels by subtracting the average amplitude between -200 ms and 0 ms. All further analyses were restricted to the three central EEG derivations Fz, Cz and Pz as most commonly selected for ERP studies [142;145;166;169;170].

Recurrence Quantification Analysis

The state of a system, e.g. atmospheric, biologic and physiologic systems, can change in time. Due to the importance of such alterations for human life, several research groups focus their effort on finding ways to describe and, of course, predict the dynamics of these fluctuations.

The numbers of variable needed to describe a system depends on how complex it is (each variable represents one dimension of its phase space). When real systems are analyzed, usually not all variables (and states) necessary to fully describe it can be measured. Takens's theorem [171] demonstrated that it is possible to reconstruct a picture that contains the same topological information of the multidimensional system behaviour using only one variable. In this theorem, the multi-dimensional state vector $\vec{x}$ that describes the system trajectory in an *m*-dimensional space can be constructed from a one-dimensional time series u_i:

$$\vec{x}_i = (u_i, u_{i+d}, ..., u_{i+(m-1)d}), \quad (3.1)$$

where d is the time delay and m is the embedding dimension. m should be greater than two times the original dimension of the system to the theorem be validated.

In 1987, Eckmann et al. [172] proposed a visual tool called recurrence plot (RP) to graphically depict temporally correlated linear and non-linear information of time series. The RP construction uses **Equation (3.1)** to create the states of the system, and visualizes those states that recur in time. The RP can be graphically represented by a binary $N \times N$ matrix with black and white dots representing two states being close or distant to each other at a given threshold (ε). Thus, the RP matrix is defined as:

$$\mathrm{R}_{i,j} = \Theta\left(\varepsilon - \left\|\vec{x}_i - \vec{x}_j\right\|\right), \quad (3.2)$$

$\Theta(y)$ is the Heaviside function: $\Theta(y)=0$ (white dot in the RP) if $y<0$, and $\Theta(y)=1$ otherwise (black dot in RP); $i,j=1,\ldots,N$, with N being the number of states and $\|\ \|$ being a matrix norm that measures the distance between two vectors. In the present work, the Euclidian norm was used. Therefore, the dynamic information of the system is eventually contained in the structure of the RP. As an example, a random system shows just isolated black dots in the RP, as system recurrence is random. A sinusoid fluctuation, on the other hand, shows periodic diagonal lines in the RP, the distance of which relates to the basic frequency of the system (**Figure 3.2**).

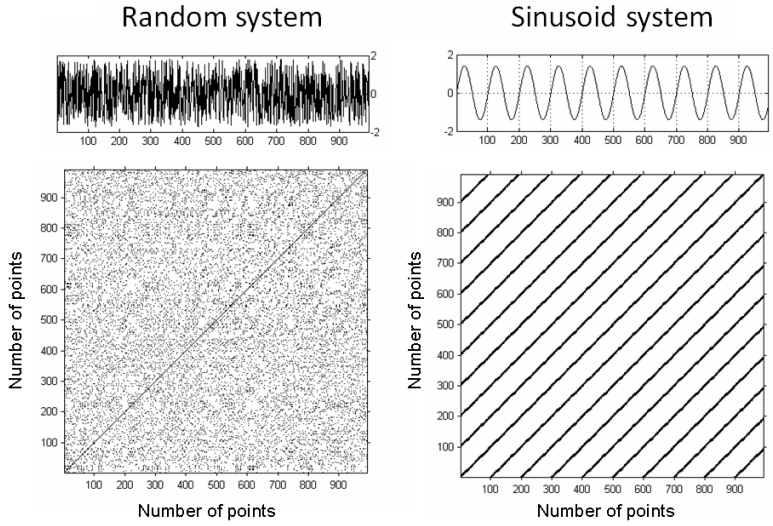

Figure 3.2. Time series (top row) and recurrence plot (bottom row) of a random (left) system and a sinusoid (right). Settings were: $m=4$, $d=3$ and 10 % of fixed amount of nearest neighbors. The main diagonal in both RP represents the degree of auto-recurrence, i.e. the comparison of each state with itself.

The choice of the distance threshold ε is crucial. If ε is too small, few recurrence points will be found and information about the dynamic of the system will be lost. If ε is too high, many neighbours will be falsely classified as recurrent, resulting in a lot of artifacts in the RP. In the present study, each state vector $\vec{x}$ has

the same percentage of neighbours (10 %). The $\vec{x}_i$ neighbours are defined as $\vec{x}_j$ contained in a sphere centred in $\vec{x}_i$ (fixed amount of nearest neighbours- FAN). By this a different ε is attributed to each point to achieve a constant recurrence density [173].

RP is a useful method to visualize dynamic behaviour, but depending on the complexity of the system, additional quantification of the RP is needed. For this reason, Zbilut and Webber [159] introduced a quantification scheme of the recurrence points in a RP as a whole (percentage of the RP showing recurrent points) and of specific segment lines in the RP (diagonal lines: $\mathrm{R}_{i+k,j+k}=1$, $k=1,\ldots l$ and l is the diagonal line length). Marwan and co-workers introduced measures based on vertical lines ($\mathrm{R}_{i,j+k}=1, k=1,\ldots v$, v is the vertical line length) and showed that these measures are capable to detect chaos-chaos transitions in physiological data [174].

In the present work, RQA was performed using the Matlab (R2008b version, the MathWorks, Inc., USA) and the CRP toolbox version 5.5 (http://www.agnld.uni-potsdam.de/~marwan/toolbox). The RQA variables analyzed in this study are defined in **Table 3.1**, matching also the CRP toolbox manual version 5.15, release 28.

The choice of the embedding parameters *dimension* and *delay* is also critically influencing the RQA results. Common methods for their identification are the false nearest neighbours method for the dimension (m), as proposed by Kennel et al. [175], and the mutual information approach for the delay (d) as suggested by Frazer and Swinney [176] for non-biological time series. However, it is still unclear if these approaches are also valid for biological systems. Consequently, RQA using different combinations of m and d was applied to screen how the power of RQA variables to discriminate tone types depends on these parameters (**Figure 3.3**).

3.1. RQA variables

Variables based on diagonal lines		Variables based on vertical lines	
Determinism (DET)	$\mathrm{DET} = \frac{\sum_{l=l_{\min}}^{N} lP^{\varepsilon}(l)}{\sum_{i,j}^{N} R_{i,j}^{m,\varepsilon}}$ $P^{\varepsilon}(l) = \{l_i, i = 1 \ldots N_l\}$ is the frequency distribution of diagonal structures with lengths l, N_l in the total number of diagonal lines and $l_{\min} = 2$ the defined minimum length of the diagonal structure.	Laminarity (LAM)	$\mathrm{LAM} = \frac{\sum_{v=v_{\min}}^{N} vP^{\varepsilon}(v)}{\sum_{v=1}^{N} vP^{\varepsilon}(v)}$ $P^{\varepsilon}(v) = \{v_i, i = 1 \ldots N_v\}$ is the frequency distribution of vertical structures with lengths v, N_v in the total number of diagonal lines and $v_{\min} = 2$, the defined minimum length of the vertical structure.
Maximal diagonal line (MaxL)	$MaxL = \max(l_i; i = 1 \ldots N_l)$	Trapping time (TT)	$\mathrm{TT} = \frac{\sum_{v=v_{\min}}^{N} vP^{\varepsilon}(v)}{\sum_{v=\min}^{N} P^{\varepsilon}(v)}$
Average diagonal line (AvgL)	$\mathrm{AvgL} = \frac{\sum_{l=l_{\min}}^{N_l} lP^{\varepsilon}(l)}{\sum_{l=l_{\min}}^{N_l} P^{\varepsilon}(l)}$	Maximal length of vertical structures (MaxV)	$MaxV = \max(v_i; i = 1 \ldots N_v)$

Table 3.1. RQA variables definition as described in the manual of the CRP toolbox, Version 5.15, Release 28.

The number of state vectors created from a time series is given by $w-(m-1)d$, with w being window size, i.e. e number of points used from the one-dimensional time series. In the present work, the window size was 100 points, as described below. m and d combinations were limited to values that produced at least 50 states (**Figure 3.3**).

The respective range of the RQA variable *maximum diagonal line* (MaxL), *average diagonal line* (AvgL), *trapping time* (TT) and *maximum vertical line* (MaxV)

depends on the number of the analysed states. In order to be able to compare RQA values obtained with different m and d, the original values were divided by $w-(m-1)d$.

Definition of ERPs and RQA time windows

The P200 and P300 were defined as maximum EEG amplitude between 160 - 252 ms and 260 - 460 ms, respectively [144;145;148;166]. N100 was defined as the minimum peak in the time window 50 - 156 ms [153].

A topographic map of the grand average of the ERP of the difference between rare and frequent tones (time window: 0 ms to 800 ms after tone presentation) was generated using the triangulation and linear interpolation algorithms as implemented in the Brain Vision Analyzer version 1.5. A topographic map of the ERP difference between frequent tones immediately preceding rare tones ($frequent_{before}$) and frequent tones immediately following rare tones ($frequent_{after}$) was also generated.

While the analysis of ERP components using amplitude averages is rather standardized, it was a priori unknown which time window would deliver the most sensitive RQA measurements. The window size was chosen based upon a tradeoff between temporal resolution and reliability of the estimate. A large window results in good estimates but low resolution, while a small window results in good resolution but poorer estimates. Therefore, three different time windows for RQA each of which comprised 100 sample points (W1: 84 – 484 ms, W2: 204 – 604 ms, and W3: 324 – 724 ms) were chosen for analysis. These broader time windows cover a total of about 800 ms after tones and allow testing of high values of m and d and still having good estimates.

Each ERP amplitude and RQA variable was identified for all trials as described above and then compared between rare and frequent tones (Figure 3.3). To control for any bias in the analysis possibly introduced by the discrepancy between the specific temporal windows for ERP amplitude detection and the ones chosen for RQA, the mean amplitude and the mean absolute amplitude of the full temporal windows W1, W2, W3 were also analyzed for their potential to differentiate between tone types.

Statistical analysis

First, the six RQA variables (**Table 3.1**) and the nine amplitude based ones were explored, including ERP, mean and mean absolute amplitude (amplitude analysis - AA) with regard to their potential to discriminate between frequent and rare tones and focusing on data recorded without concurrent MRI acquisition. As the resulting RQA and AA measures cover different absolute ranges, these measures were subjected to a z transformation ($z = (x - \mu)/\sigma$); x, μ and σ are the raw value, mean and standard deviation of all trials, respectively) to allow for comparison across different measures. Transformed measures were then used to calculate Cohen's *d* as effect size measure for the difference between rare and frequent tones for each subject. Statistical inference at the group level was then estimated by one sample t-tests against zero for the respective measures. This allowed to control if effects shown the same sign across subjects. For each of the two methods (RQA versus AA), the variables with highest mean effect size (see results) was used for the further analyses. To compare RQA with AA, a paired t-test between the two optimal measures was performed (**Figure 3.3**).

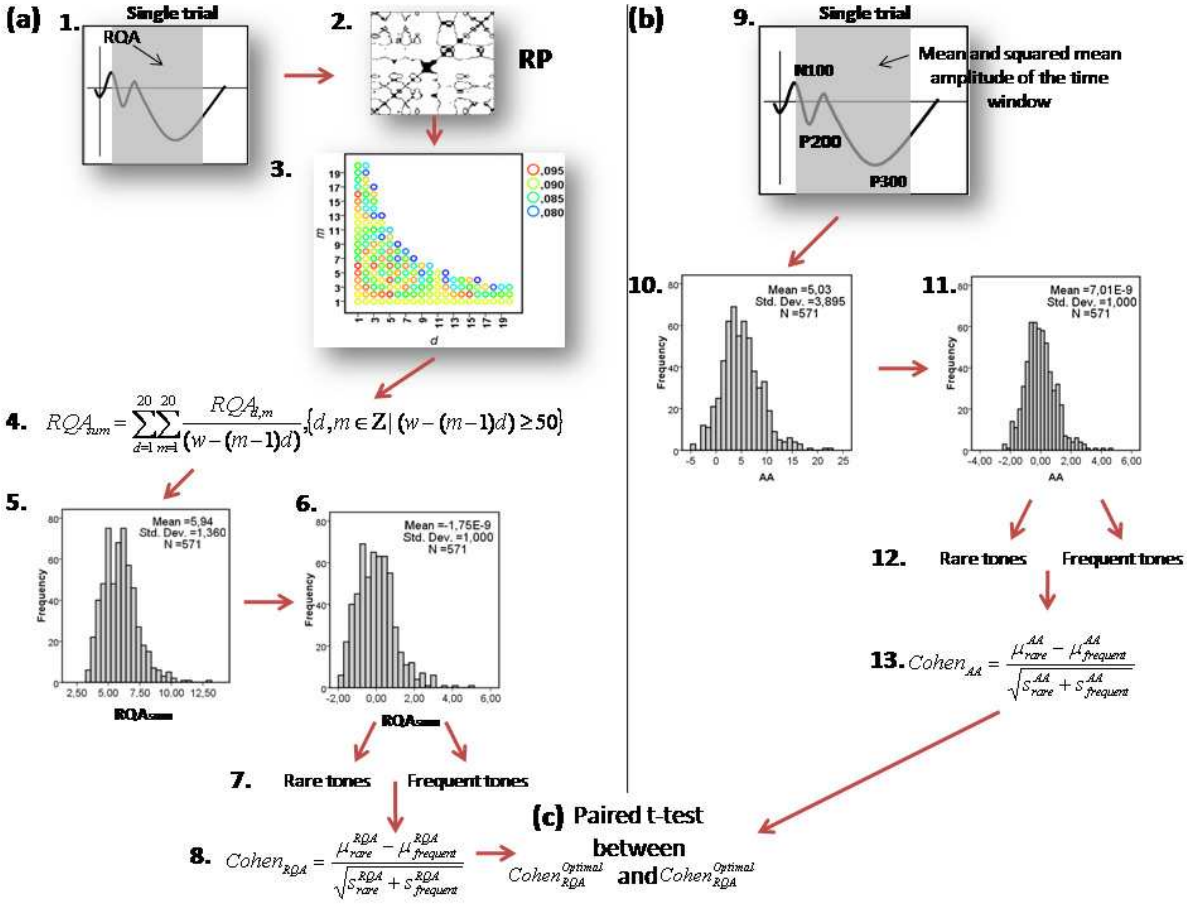

Figure 3.3. RQA and AA pipeline. (a) RQA procedure: (a.1) for each single trial three time windows were chosen to apply RQA (W1: 84 – 484 ms, W2: 204 – 604 ms, and W3: 324 – 724 ms). (a.2) RPs are created and the RQA variables are quantified (Table 3.1). (a.3) the procedure in (a.2) is repeated for several values of m and d. (a.4) All values found in procedure (a.3) are summed following the present equation (RQA_{sum}). All the previous steps are repeated for each trial (rare and frequent tones). Step (a.5) exemplifies a histogram graph of all trials for one RQA_{sum} variable. (a.6) These RQA_{sum} values are z-transformed. (a.7) the trials are grouped in rare and frequent tones. (a.8) Cohen effect sizes are calculated. μ_{rare}^{RQA} and $\mu_{frequent}^{RQA}$ are the mean of the RQA_{sum} values for all rare and frequent tones respectively. $s_i^{RQA} = (n_i - 1)\left(\left(s_i^{RQA}\right)^2 \Big/ (n_{rare} + n_{frequent})\right)$, where s_i^{RQA} is the SD of the RQA_{sum} values, i = rare or frequent and n_{rare} and $n_{frequent}$ are the total number of rare and frequent trials, respectively. Steps (a.1) to (a.8) are repeated for each subject and EEG channels (Fz, Cz, Pz). (b) AA analysis: (b.9) P300, P200, N100, mean and squared mean amplitudes (W1, W2, W3) are indentified for each trail. Note that for reporting ERPs, positive deflections are showing downward maxima, while negative deflections are upward. (b.10) exemplifies a histogram graph of all trials for one AA variable. (b.11) These AA values are z-transformed. (b.12) the trials are grouped in rare and frequent tones. (b.13) Cohen effect sizes are calculated. μ_{rare}^{AA} and

$\mu_{frequent}^{AA}$ are the mean of the AA values for all rare and frequent tones respectively. $s_i^{AA} = (n_i - 1)\left({(s_i^{AA})^2} \Big/ {(n_{rare} + n_{frequent})} \right)$, where s_i^{AA} is the SD of the AA values, i = rare or frequent and n_{rare} and $n_{frequent}$ are the total number of rare and frequent trials respectively Steps (b.9) to (b.13) are repeated for each subject and EEG channels (Fz, Cz, Pz). (c) For each method (RQA and AA), the variable with higher mean Cohen effect size between subjects was chosen as optimal variables. The methods were cross-tested by a paired t-test between the Cohen effect sizes of these optimal variables ($Cohen_{RQA}^{Optimal}$ and $Cohen_{AA}^{Optimal}$ for RQA and AA respectively).

Additionally, it was assumed that both amplitude and RQA measures show a high degree of temporal auto-correlation over the course of an experiment. This auto-correlation is in part caused by subject-specific features such as head geometry and skin conductance properties that lead to higher within-subject similarity of trials compared with between-subject similarity. Second, it is caused by slow amplitude fluctuations or slow changes of non-linear patterns that - across several trials – may be induced by fluctuations of the brain's general functional state, e.g. reflecting alterations in vigilance or attention [145;148-151]. To account for this auto-correlation over the experiment and to optimize the sensitivity of both methods, a second analysis was performed in which frequent or rare tones were not pooled all together. Instead, pairs of rare tones and the preceding or following frequent tone were grouped together. For the 'optimal' variables identified in the previous step (**Figure 3.3**), the difference of these consecutive tones per trial was calculated and difference values gained for RQA (Δ_{RQA}) and the amplitude analysis (Δ_{AA}). The temporal order to calculate the difference values between tones was 'previous minus the following trial'. For both methods, these difference values were entered into one-factorial repeated measures ANOVA (factor *trial* with *T* levels, where *T* is the number of trials). Here, the significant changes over the experiment (*trial* factor) were not in the focus, but the

significance of the deviation of all differences from zero represented by the intercept. Importantly, this approach allowed for a trial-wise comparison across methods by performing an across method subtraction (Δ_{RQA}-Δ_{AA}) and testing the resulting difference values against zero in a repeated measures ANOVA, again testing the intercept. If the intercept factor had a significant effect and the estimated means of the factor *trial* showed to be positive or negative, this would represent a superiority of RQA or AA method, respectively.

Results

Explorative analysis of ERP amplitude and RQA variables

First, the RQA (**Table 3.1**) and AA variables (N100, P200, P300, mean amplitudes and absolute mean amplitudes of time windows W1, W2, W3) derived from the central electrodes (Fz, Cz and Pz) were investigated. This investigation was based on the dataset obtained outside the MR environment, focussing on Cohen's *d* as effect size measure in the comparison of frequent and rare tones.

Figure 3.5 shows the grand average of the ERPs in response to frequent and rare tones (left column), and the spatial representation of the difference between both time series as topographical map (mid column, left image). As expected, P300 amplitudes were higher (more positive deflection) for rare tones. The highest amplitude difference between rare and frequent ERP grand averages was found in posterior brain areas.

For the AA measures, highest mean effect size value was found for the P300 time window (0.90 ± 0.47) in Pz channel (**Figure 3.4a**).

As mentioned, RQA variables are highly dependent on the embedding parameters m and d. This dependency showed a huge inter- and intra-subject variability (see **Figure 3.6**). Thus, to avoid a suboptimal choice of m and d, a sum score based on all combinations of $1 \leq m \leq 20$ and $1 \leq d \leq 20$ was used (**Figure 3.3**, **(a.3)**).

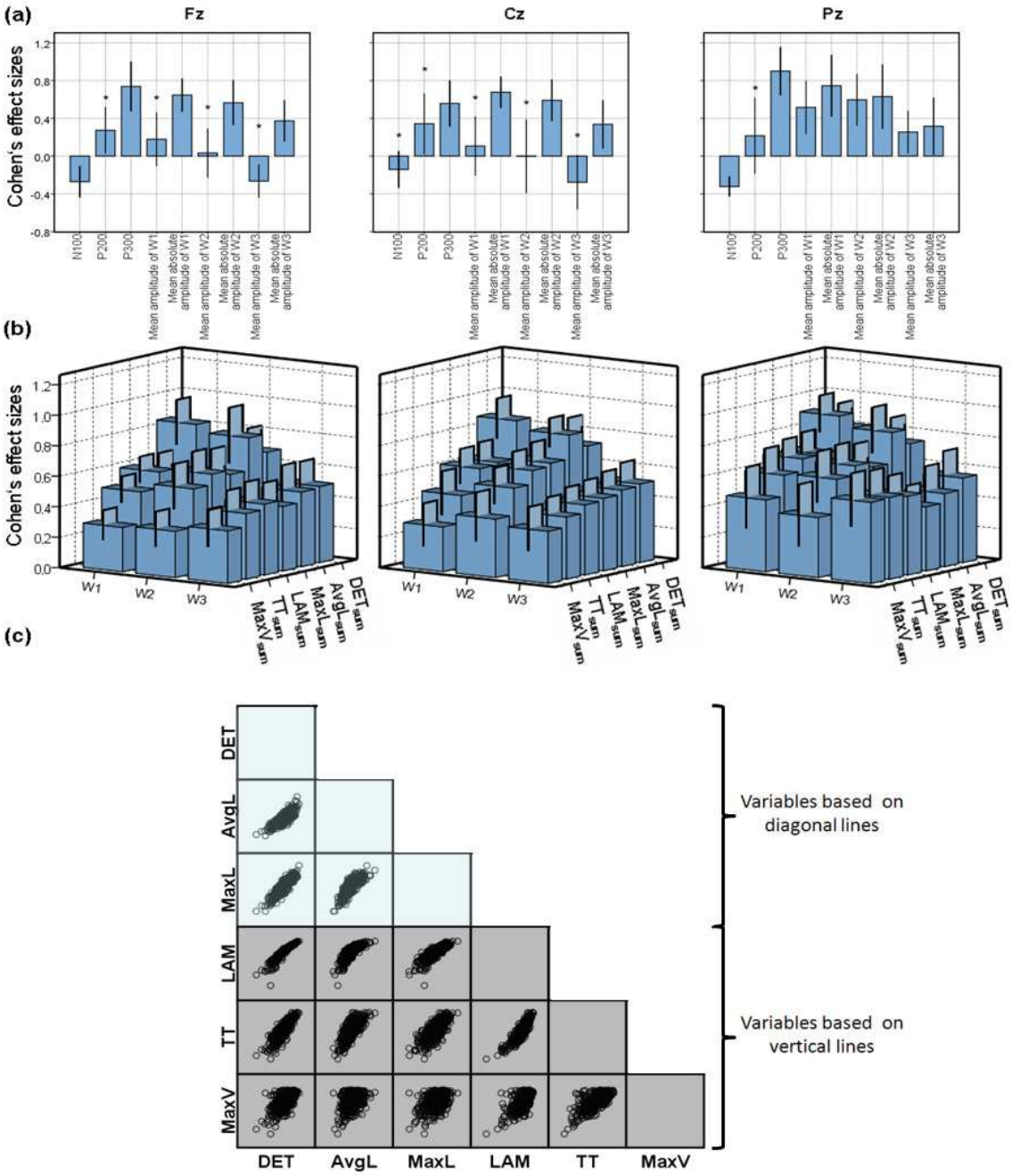

Figure 3.4 Differentiation power of AA and RQA group analysis for undistorted EEG recordings.

(a) Effect sizes of the group mean amplitude and 95% confidence interval for N100, P200, P300 (bars 1-3) as well as mean and mean absolute amplitudes (bars 4-9), results are depicted separately for electrodes Fz, Cz and Pz. Note the nominally highest average effect for the P300 amplitude in channel Pz. * indicates not significant group effect ($p>0.05$). (b) Effect sizes of RQA variables for all midline electrodes and time windows W1, W2, W3. Superiority of AvgL in time windows W1 for all electrode positions can be seen. (c) Strong cross-correlation was noted between the six selected RQA variables ($r>0.377$, $p<0.01$).

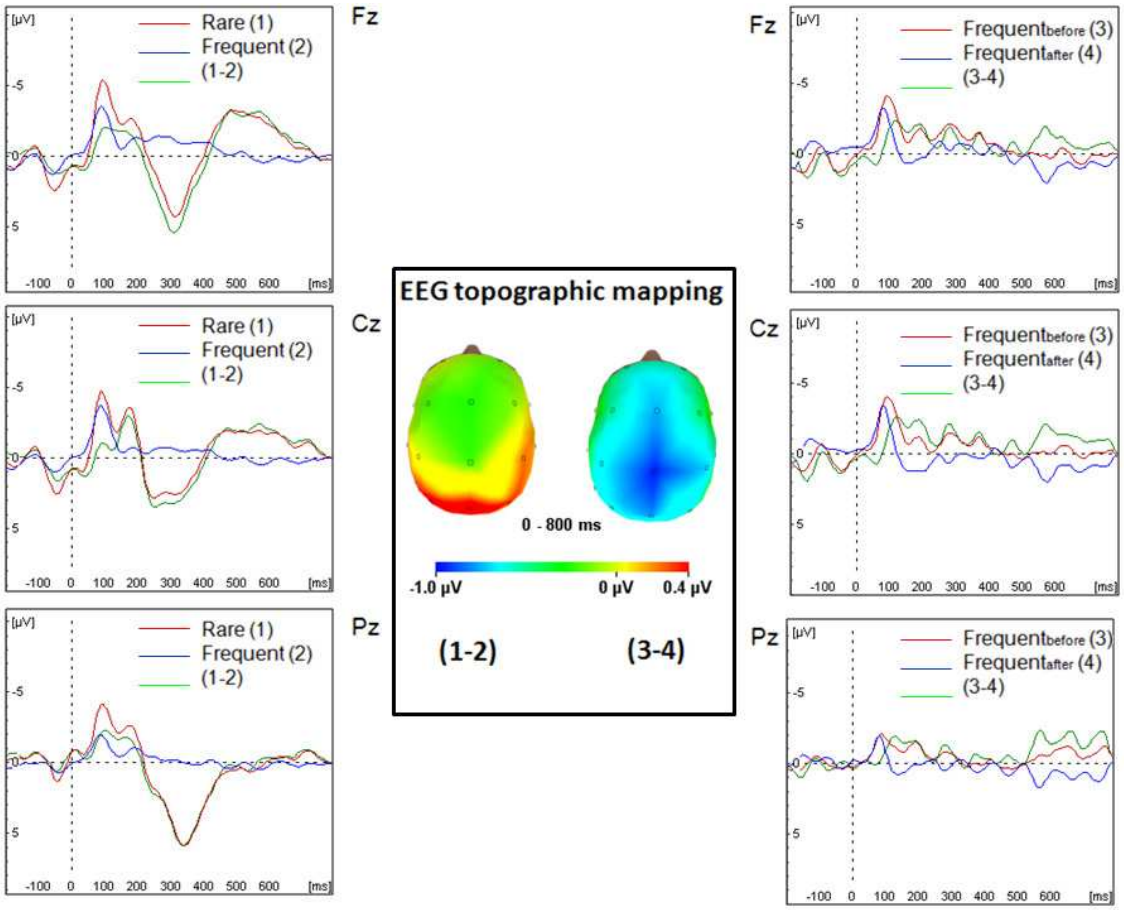

Figure 3.5. Topography of ERP grand averages (data acquired outside the MR). ***Left column:*** **Grand averages of rare tones (1), frequent tones (2) and the difference between them (1-2).** ***Right column:*** **Grand averages of frequent$_{before}$(3), frequent$_{after}$ (4) and the difference between them (3-4).** ***Middle column:*** **EEG topographic mapping of (1-2) and (3-4).**

This analysis approach prevents overfitting of the specific experiment by selecting a fixed set of embedding parameters. The alternative approach - optimizing m and d separately for each subject – may hamper interindividual comparison, as e.g. in group studies.

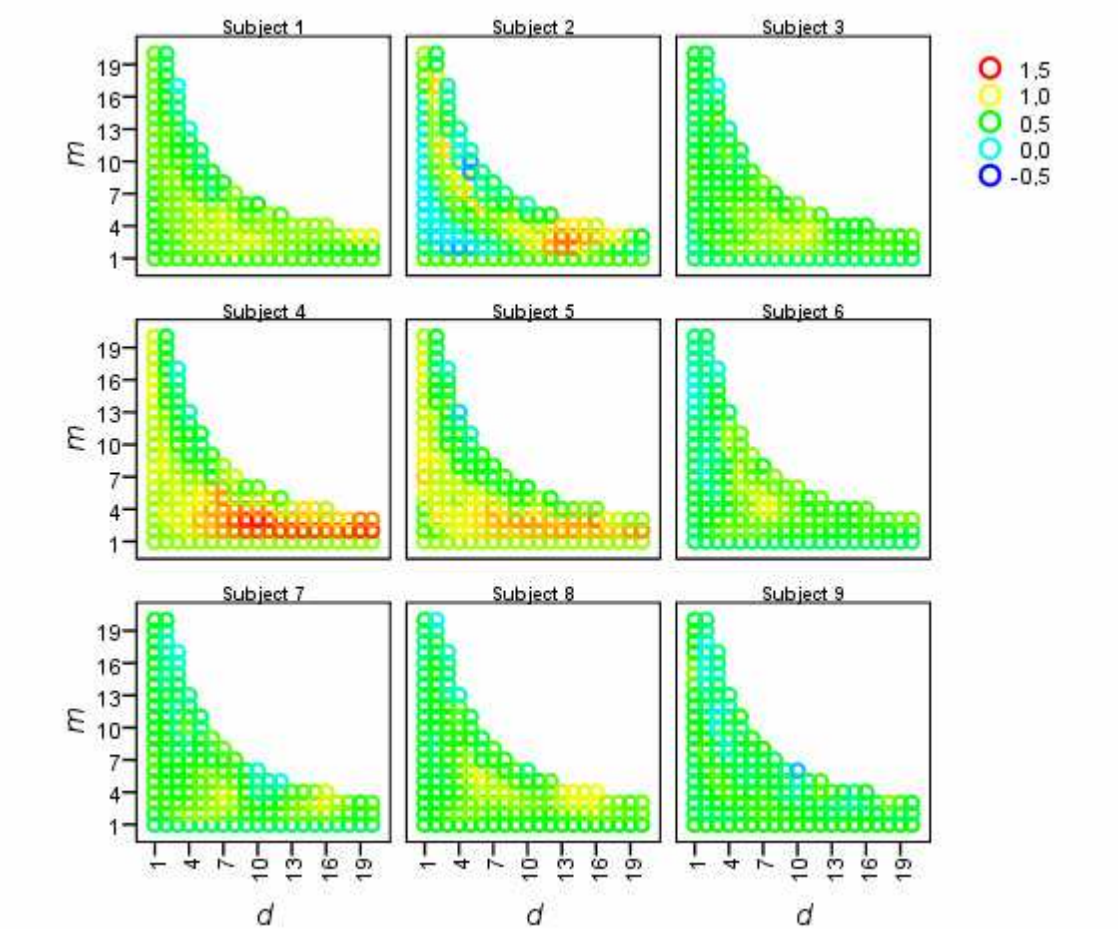

Figure 3.6. Cohen's effect sizes for comparison of frequent and rare tones using RQA measure AvgL. Effect sizes for different embedding parameters m and d were calculated for each subject on the basis of undistorted EEG data (Pz electrode) and are depicted as color-code. While considerable inter-subject variance of the effect sizes and their distribution across m and d were seen, the range of m between about 2 and 5 provided effect sizes >0.5 across subjects.

Using the sum scores (**Figure 3.3**, **(a.4)**), $AvgL_{sum}$ measured in W1 of Pz showed highest mean effect sizes (0.91 ± 0.22) for separation of rare and frequent tones (**Figure 3.4**). Therefore, the electrode Pz and time window W1 was used for further analyses.

RQA variables are highly correlated among each other (**Figure. 3.4c**), suggesting that the results of different values of m and d may have validity also for RQA variables other than AvgL. As mentioned above, it was not possible to identify a

single m and d pair which would allow for optimized tone differentiation in all subjects. However, for AvgL highest effect sizes for tone discrimination were generally obtained for 2 ≤ m ≤ 5 and 5 ≤ d ≤ 20. Given that the comparison between $AvgL_{sum}$ calculated with 1 ≤ m ≤ 20 and 1 ≤ d ≤ 2 or 2 ≤ m ≤ 5 and 5 ≤ d ≤ 20 showed significant results (t(8) = 5.04, p = 0.001, paired t-test), further steps of the analyses were restricted to 2 ≤ m ≤ 5 and 5 ≤ d ≤ 20 and the reported RQA results were based on the following variable and embedding parameters (**Figure 3.6**):

$$AvgL_{sum} = \sum_{d=5}^{20}\sum_{m=2}^{5}\frac{AvgL_{d,m}}{(w-(m-1)d)}, \{d, m \in \mathrm{Z} \mid (w-(m-1)d) \geq 50\} \quad (3.3)$$

To compare between the classical ERP amplitude analysis and the RQA, P300 and **Equation (3.3)** for time window W1, both measured in Pz were used. The power to distinguish between rare and frequent tones for data recorded with and without concurrent MRI acquisition was estimated.

Cross-methods comparison of differentiation between rare and frequent tones (EEG recordings outside the scanner)

At the group level, both P300 (0.90 ± 0.47, t(8) = 5.79, p <0.0001) and $AvgL_{sum}$ (0.91 ± 0.22, t(8) = 12.38, p < 0.0001) showed similarly high effect sizes with lower variance across subjects seen for $AvgL_{sum}$. Effect size of $AvgL_{sum}$ were higher than those of P300 in six out of nine subjects (**Table 3.2**), yet, formal pair-wise comparison between the methods yielded no significant difference (paired t-test, t(8) = 0.58, p = 0.58).

3.2. Effect sizes for AvgL and P300 gained from undistorted EEG recordings

Subject	$AvgL_{sum}$	P300
1	1.01	0.79
2	1.08	0.47
3	0.84	0.62
4	1.25	0.47
5	1.09	1.95
6	0.80	0.65
7	0.70	1.22
8	0.89	0.10
9	0.54	0.94

Table 3.2. Cohen's effect size (rare vs. frequent tones) for P300 (channel Pz) and $AvgL_{sum}$ (channel Pz; time window W1) for each individual subject.

Cross-methods comparison of differentiation between subtypes of frequent tones (EEG recordings outside the scanner)

As stated above, the occurrence of a rare tone interrupting the continuous series of frequent tones may lead to changes in neural responsiveness, e.g. by increasing the subject's arousal. Therefore, differences across the AA and RQA methods were calculated for corresponding frequent trials flanking a rare tone. Statistical inference was calculated comparing all such pairwise differences against zero by using repeated measures ANOVA. Of a typical series of trials ($frequent_{before}$ - rare - $frequent_{after}$), i) rare tones with respect to the preceding frequent tone ($frequent_{before}$/rare), ii) rare tones with respect to the following frequent tone

(rare/frequent$_{after}$), iii) frequent tones flanking a rare tone (frequent$_{before}$/frequent$_{after}$) were compared.

For both P300 and AvgL$_{sum}$ strong differences for tone pairs (i) and (ii) were detected (**Table 3.3**), yet, both analytical methods were not significantly different from each other ($F(1,8) = 0.99$, $p = 0.350$, and $F(1,8) = 1.08$, $p = 0.330$ for (i) and (ii), respectively). In contrary, only AvgL$_{sum}$ but not P300 was effective in distinguishing between frequent$_{before}$ and frequent$_{after}$ tones (pair (iii)) (**Table 3b**).

The ERP grand averages of the difference between frequent$_{before}$ and frequent$_{after}$ showed a different topographic distribution (**Figure 3.5**, right column) compared with the frequent/rare comparison (**Fig 3.5**, left column) with similar absolute amplitudes in all midline electrode positions (Fz, Cz, Pz).

For this reason, the comparison of pair (iii) was extended to all midline EEG channels (**Table 3.3b**). Also in the additional channels (Fz and Cz), P300 could not provide significant distinction for pairs of type (iii), whereas AvgL$_{sum}$ provided a significant distinction with the largest effect in Cz ($\Delta_{AvgLsum} = 0.31 \pm 0.09$), in accordance with the topographical map (see **Figure 3.5**, mid column, and **Table 3.b**).

3.3. Comparison of trialwise difference values (undistorted EEG recordings)

Test of difference against zero (intercept)				
	P300		**AvgL$_{sum}$**	
	F	**p**	**F**	**p**
Frequent$_{before}$/rare	Pz (31.60)	Pz (<0.0005)	Pz (101.18)	Pz (<0.0005)
Rare/frequent$_{after}$	Pz (25.63)	Pz (0.001)	Pz (80.36)	Pz (<0.0005)

Table 3.3a. ANOVA repeated measures of the frequent$_{before}$/rare and rare/frequent$_{after}$ transitions in electrode Pz. P-values of the intercept term are given, denoting significant deviation from zero (df1=1 and df2=8).

	Intercept							
	P300		**$AvgL_{sum}$**		**Mean amplitude in W1**		**Mean absolute amplitude in W1**	
$Frequent_{before}/frequent_{after}$	**F**	**p**	**F**	**p**	**F**	**p**	**F**	**p**
	Fz (0.01)	Fz (0.718)	Fz (3.60)	Fz (0.094)	Fz (10.90)	Fz (0.011)	Fz (0.02)	Fz (0.891)
	Cz (0.000)	Cz (0.999)	Cz (11.33)	Cz (0.010)	Cz (13.28)	Cz (0.007)	Cz (1.17)	Cz (0.311)
	Pz (1.16)	Pz (0.313)	Pz (6.71)	Pz (0.032)	Pz (2.87)	Pz (0.130)	Pz (2.90)	Pz (0.127)

Table 3.3b. Undistorted EEG recordings. ANOVA repeated measures of the $frequent_{before}/frequent_{after}$ transitions using the P300, $AvgL_{sum}$, mean and mean absolute amplitude of W1 (df1=1 and df2=8).

The grand average of the ERPs pointed out that amplitude differences between $frequent_{before}$ and $frequent_{after}$ were largest in a temporal window between 100 ms and 200 ms, which is covered by the time window W1 (used for $AvgL_{sum}$), however, not by the time window used for P300 detection. Thus, to avoid an overly influence of different temporal windows analysed, the amplitude based analyses (mean and mean absolute) of pairs of type (iii) for W1 were repeated (**Table 3.3b**). This analysis revealed that the mean amplitude but not mean absolute amplitude of W1 distinguished between subtypes of frequent tones, with the highest F-value in Cz ($\Delta_{\text{mean amplitude of W1}}$= -0.36 ± 0.10). Formally, the difference across AA and RQA yielded a significant result (F(1,8) = 27.63, p=0.001). However, in the case of a positive deflection in the electrophysiological data (as observed in W1), the difference of amplitudes was *negative*, whereas the differences of $AvgL_{sum}$ were *positive*, which may result in an artificial finding on the superiority of RQA. When considering this difference of $AvgL_{sum}$ with respect to the negative numerical sign of the deflection (by

simply inverting the $AvgL_{sum}$ Δ values), methods were not statistically different ($F(1,8) = 0.103$, $p = 0.757$).

Cross-methods comparison of differentiation between rare and frequent tones (EEG recordings inside the scanner)

MR image acquisition will introduce systematic noise in the simultaneous measured EEG recordings. For the analysis of EEG data recorded inside the scanner, the same channel (Pz) and measures (P300 versus $AvgL_{sum}$ of W1 [**Equation (3.3)**]) were employed as for the analysis of EEG data obtained outside the scanner. Again, both methods discriminated between rare and frequent tones with medium to large effect sizes (P300: 0.68 ± 0.20, $t(8) = 3.42$, $p < 0.0005$; $AvgL_{sum}$ 0.62 ± 0.11, $t(8) = 5.65$, $p < 0.0005$) (**Table 3.4**). $AvgL_{sum}$ showed higher effect sizes in three of nine subjects, but the methods were not significantly different in a paired comparison of their effect sizes ($t(8)= 0.37$ $p = 0.723$).

3.4. Effect sizes for AvgL and P300 derived from EEG recordings during an fMRI scan

Subject	$AvgL_{sum}$	P300
1	0.52	-0.16
2	0.28	0.32
3	0.50	0.49
4	0.90	0.09
5	1.02	1.73
6	0.26	0.62
7	0.66	0.96
8	0.30	0.73
9	1.12	1.34

Table 3.4. Cohen's effect sizes (rare vs. frequent) for P300 (channel Pz) and $AvgL_{sum}$ (channel Pz, W1) for all subjects.

Cross-methods comparison of differentiation between subtypes of frequent tones (EEG recordings inside the scanner)

Under the unfavourable EEG recording conditions during an MRI acquisition, repeated measures ANOVA again revealed significant results for pairs of type (i) and (ii) for both P300 and $AvgL_{sum}$ (**Table 3.5a**). For neither pair type, however, differences between methods were significant ($F(1,8) = 0.00$, $p = 0.987$ and $F(1,8) = 0.28$, $p = 0.612$, respectively). For the pair type (iii), in accordance with the analysis of the data recorded without concurrent MRI acquisition, $AvgL_{sum}$ and mean amplitude of W1 and Cz were tested (**Table 3.5b**). Both measures distinguished between $frequent_{before}$ and $frequent_{after}$ tones ($\Delta_{\text{mean amplitude of W1}} = -0.12 \pm 0.05$ and $\Delta_{AvgLsum} = 0.22 \pm 0.07$). Yet, neither method was superior when compared under consideration of the aforementioned insensitivity of RQA towards numerical amplitude signature ($F(1,8) = 1.01$, $p = 0.344$).

3.5. Comparison of trialwise difference values (EEG recordings during an fMRI scan)

	Intercept			
	P300		**$AvgL_{sum}$**	
	F	**p**	**F**	**p**
$Frequent_{before}$/rare	11.88	0.009	33.22	<0.0005
Rare/$frequent_{after}$	13.31	0.007	47.00	<0.0005

Table 3.5a. ANOVA Repeated measures of the $frequent_{before}$/rare, rare/$frequent_{after}$ transitions in electrode Pz. P-value of the intercept term is given, denoting significant deviation from zero (d1=1, d2=8).

	Intercept			
	$AvgL_{sum}$		**Mean amplitude of W1**	
$Frequent_{before}/frequent_{after}$	**F**	**p**	**F**	**p**
	Cz (9.16)	Cz (0.016)	Cz (6.80)	Cz (0.031)

Table 3.5b. ANOVA repeated measures of the $frequent_{before}/frequent_{after}$, transitions using the $AvgL_{sum}$, mean amplitude of W1 (df1=1 and df2=8).

Correlation between EEG amplitude based measures and $AvgL_{sum}$

Linear correlations between P300 and $AvgL_{sum}$ (**Figure 3.7a**) were weakly positive (maximum r^2 = 0.30) and significant for all subjects ($p < 0.01$). The correlation between the mean amplitude of the ERP signal in W1 and $AvgL_{sum}$ was extremely low ($r^2 < 0.04$), with only one individual subject showing a significant correlation ($r^2 = 0.032$, $p<0.01$). However, as mentioned above, $AvgL_{sum}$ can just be a positive number while the mean amplitude may also show negative values. When mean absolute amplitudes are used to avoid spanning of the variance by negative amplitude values, correlations were more strongly positive and again significant for all subjects ($p < 0.01$) (**Figure 3.7b**).

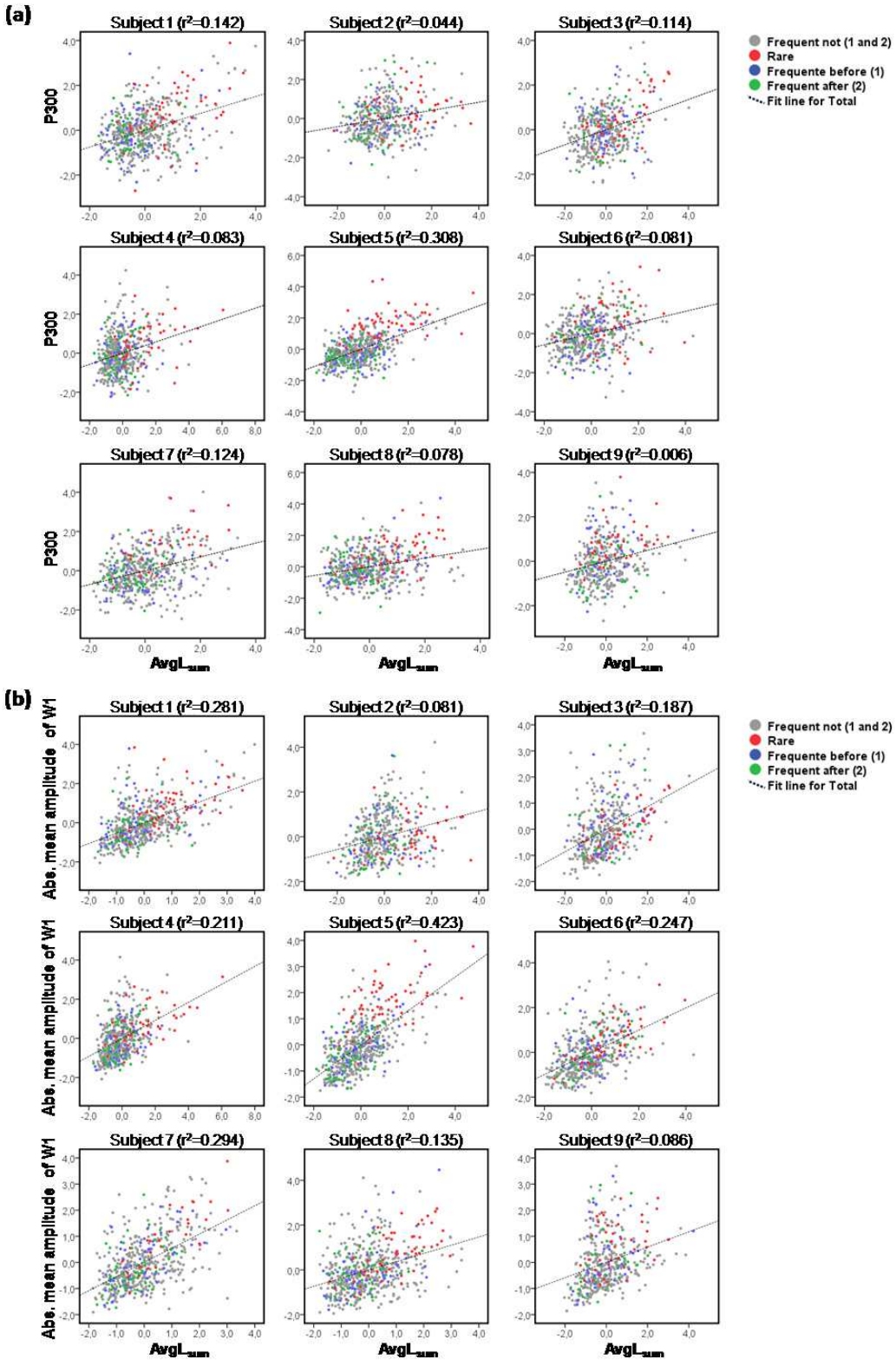

Figure 3.7. Single trial correlation between $AvgL_{sum}$ and AA measures. (a) Weak positive correlations (r^2 between 0.044 and 0.308) between P300 amplitude (μV) and $AvgL_{sum}$ were found. (b) Similarly, the use of the same time window (W1) for RQA and AA resulted in weak correlations between $AvgL_{sum}$ and the mean absolute amplitude (r^2 between 0.040 and 0.449).

Discussion

In this study, RQA was applied to analyze EEG recorded during a classical auditory oddball experiment. Its power to distinguish between different tone types was compared to amplitude based analysis. Furthermore, the robustness of RQA towards unfavourable EEG recording conditions as typically found during simultaneous recordings of EEG and MRI was investigated. In brief, the main findings were: (1) RQA could robustly detect differences in the non-linear signal structure between rare and frequent tones. (2) This discrimination ability was maintained for the EEG recorded with concurrent MRI acquisition. (3) Compared with amplitude based analysis, no statistically significant difference was found regarding the ability to distinguish between tone types. 4) Linear correlations between the two methods across trials were low to medium, supporting that RQA may extract ERP features that are different from simple amplitude characteristics.

Previous attempts of ERP single trial characterization

A number of alternative approaches have been used in literature to address the problem of single trial ERP characterization before: Bénar et al. [152] tracked trial-by-trial amplitude changes of the EEG response recorded during an oddball paradigm. Both at the single subject level and for an fMRI group analysis, the authors found that ERP amplitudes explained a significant amount of variability of the fMRI BOLD response. Mantini et al. [157] used the EEG to measure P300 amplitude variability across trials. Other than Bénar et al. [152], they compared the individual tone trials with an average-based P300 template of the rare tones and forwarded this comparative value to fMRI analysis. They reported that such modelling of the trial-by-trial variability correlates with dorsal and ventral attention networks, providing

conceptual validation that trial-by-trial variability indeed carries important information on the current cognitive state of a subject, e.g. with respect to attention. Demiralp et. al. [177] described a wavelet based method to characterize single trials of an oddball experiment. In their analysis, a selected wavelet coefficient correlated with the EEG delta frequency power was defined as a classifier to group ERPs into P300 or non-P300 trials. They found that the formation of a P300 response was more robustly predicted by the wavelet based classifier than the rare/frequent classification. By applying ICA to EEG single trials simultaneously recorded with fMRI, Debener et al. [153], reported that the EEG correlate of performance monitoring predicted the BOLD response in the anterior cingulate and adjacent medial prefrontal cortex. Bagshaw and Warbrick [155] compared wavelet based and ICA based denoising techniques, demonstrating that wavelet denoising (WD) was superior to ICA. Zouridakis et al. [156] proposed an iterative ICA (*i*ICA) to enhance specific components of single trials ERPs. Iyer and Zouridakis [154] showed that *i*ICA improves the detection of ERP components in single trials if compared with WD and classical averaging. However, one of the general problems of ICA is that components of true neuronal origin may falsely be dismissed, leading to an underestimation of the true inter-trial neuronal variability. One common criterion to select components is a minimum correlation between the component and the ERP average. As pointed out by Bagshaw and Warbrick [155], this procedure can also reduce the contribution of non- phase-locked activity. In this respect, RQA is more explorative as it is not based on any assumption on the structure of the response signal, including the assumptions that ERP activity is phase-locked. Previous reports applied RQA to detect minute changes in EEG event-related responses at the level of individual trials [164;165;178;179]. These studies,

however, lack formal statistical cross-methodological comparisons, for example with amplitude based ERP analyses.

Comparison of RQA and AA based on pooled trial responses

When trial responses were pooled during a complete auditory oddball experiment, both RQA (represented by AvgL) and AA (represented by the P300 amplitude) provided significant distinction between the two main types of tone trials. For both methods, this distinction proved significant even at the single subject level, and also when EEG recordings were distorted by fMRI related artifacts. When individual effect sizes of RQA and AA were compared against each other in a pairwise manner, no significant difference emerged. As would be expected, MR-scanner related distortions led to slight general decrease of effect sizes, however, again both methods performed equally well in differentiating tones. Given the overall power of the present analysis, the results do not support a generally higher sensitivity of RQA towards electrophysiological signal changes as induced by tone deviance in the auditory oddball paradigm.

While there is a huge amount of literature pinpointing the functional significance of specific ERP deflections, e.g. the P300 [145;147;148;166;167;169], the RQA method, still being in its infancy as applied on biosignals like EEG, does not provide an easily understandable neurophysiolocal correlate. In ERP studies, P300 is known to be particularly evoked by rare stimuli, with its amplitude increasing from midfrontal to midparietal brain areas [180;181]. When RQA was applied for signal analysis in a time window that included the P300 component, a spatial maximum of the RQA variable $AvgL_{sum}$ over parietal midline electrodes was observed, similar to the typical maximum observed in ERP studies.

AvgL, DET and MaxL are RQA variables all based on diagonal lines features of the RP. Not surprisingly, these variables showed high linear correlation with each other. Generally, diagonal lines in the RP represent similar sequential pattern of states at different time points, reflecting information on the system's divergence. AvgL in particular reflects the average duration of such a sequential pattern, and can thus be interpreted as the mean prediction time of the system [160]. In all subjects, $AvgL_{sum}$ was higher for rare tones than for frequent tones, suggesting a less divergent system in response to stimulus deviance compared with the frequent stimulus.

Comparison of RQA and AA based on comparisons of subsequent trials

Pooling all trials of a whole oddball experiment may lead to underestimation of differences between the analysis methods. Therefore, the analysis as presented here was expanded in two ways: first, focusing on subsequent pairs of trials, which may induce fluctuations in the cerebral response, for example, due to altered vigilance state or habituation; second, pairs of corresponding differential responses were compared across the analysis methods. While again demonstrating that both methods are capable to detect strong response changes induced by tone deviance, this comparison confirmed results of the analysis of pooled trials with no significant superiority of either method in terms of sensing tone deviance.

With respect to discrimination of sub-types of frequent tones ($frequent_{before}$ vs $frequent_{after}$), it was expected that the neuronal response may depend on the specific brain state prior to stimulus delivery. Analyzing the influence of the frequent tone position relative to the rare tone, Hirata and Lehmann [182] have previously reported that the absolute amplitude of the N100 deflection was stronger for frequent tones

preceding rare tones than for frequent tones *following* rare tones. Starr et al. [183] showed that this decrease of N100 after rare tone presentation was largest for the Cz electrode position. They suggested that this N100 decrease corresponds to memory updating processes required after disruption of a series of regular tones by a deviant tone.

The a priori hypothesis of the present work was that RQA could be more sensitive in detecting such brain state differences, potentially encoded in differences of signal regularity rather than amplitude averages. Based on the undistorted EEG recordings, mean amplitude of W1 but not P300 could distinguish between subtypes of frequent tones. In fact, amplitude values within the W1 time window were higher for $frequent_{after}$ compared with $frequent_{before}$ values. This indicates that the influence of the N100 response contained in W1 could have led to this result. To confirm this, the N100 of $frequent_{after}$ and $frequent_{before}$ trials was explicitly analyzed, showing significant difference into the expected direction ($F(1,8) = 5.45$, $p = 0.048$). Comparing N100 and mean amplitude of W1, no difference was seen in the trialwise comparison $frequent_{after}/frequent_{before}$ differences of both measures ($F(1,8) = 0.52$, $p = 0.490$). This result confirmed that previously reported N100 differences were mainly underlying the amplitude difference between $frequent_{after}$ and $frequent_{before}$ found for W1. In the other hand, RQA resulted in *higher* $AvgL_{sum}$ values for $frequent_{before}$ than $frequent_{after}$. When this difference in the sign of de signal was considered appropriately, RQA again was not significantly better than AA in differentiating $frequent_{before}$ and $frequent_{after.}$ Similar results of the comparison between subtypes of frequent tones were found for data recorded with concurrent MRI acquisition. The result pattern as a whole suggests that differentiation between the two states seems to depend rather on inclusion of a critical early time window around 100 - 200 ms

than on the different analysis methods. To define whether the extraction of features from a single trial provides a more valid surrogate of the response to the rare event, parallel independent measures of brain activation such as BOLD-fMRI are needed.

Influence of embedding parameters and other parameters on RQA performance

Following Taken's theorem [171], an embedding dimension higher than twice the dimension of the data set should be used in RQA. However, Iwanski and Bradley [184] showed that for certain low-dimensional systems, it is possible to obtain similar results without embedding the raw data. Thus, the choice of 'optimal' embedding parameters for a specific application is rather arbitrary. In the present study, a sum score of several m and d values was used. In doing so, the analysis was not restricted to a given set of m and *d*, but considered a broader range of possible embedding parameters, allowing for a more generalized evaluation of the RQA approach. Also, inter-subject variability which may be inherent to physiological data is minimized by such an approach. However, the noise may affect RQA if non-optimal embedding dimensions are chosen, leading to an underestimation of RQA performance [175]. In the EEG recordings, the currents induced by rapidly switching magnetic field gradients during the concurrent MRI acquisition introduce noise and likely change the complexity of the data structure. Therefore, using a range of multiple values of m and d may overemphasize such noise components. Hence, an analysis using only a single pair of m and d parameters optimized for the individual experiment is presented in the **Appendix A3**, **Table A3.1** shows the embedding parameters associated with the highest effect size per subject for optimal EEG recordings and for EEG recordings distorted by concurrent MRI. Even when

optimizing the RQA parameter for each subject, the results did not improve rare and frequent tones discrimination if compared with P300 amplitude analysis (paired t-test of individual effect sizes, t(8) = -0.77, p = 0.462 and t(8) =1.80, p = 0.311 for data with and without concurrent MRI acquisition, respectively). In a previous work, RQA was compared with ERP analysis, however in the context of a different stimulus paradigm. Schinkel et al. [164], when analysing the ERP response to semantic mismatch, showed that RQA could classify about 14% of the trials correctly while EEG succeeded in only 1.5%. However, no formal statistical comparison between the two methods has been provided, and EEG preprocessing seemed not to be optimized for ERP amplitude analysis.

In the present work, the focus of the RQA was set on optimizing the embedding parameters m and d, however, RQA performance depends on many additional factors such as $l_{\min}$, $v_{\min}$, threshold and norm used to define the distance between two states (see **Table 3.1**). Marwan et al [179] suggested that RQA based on order patterns, in comparison with FAN, would better reveal the P300 component. Preliminary analyses comparing the power of the RQA using FAN and using order pattern (not shown) revealed that results were better when RQA was performed using FAN. This leaded the present analysis to be based on FAN.

Correlation between EEG amplitude based measures and $AvgL_{sum}$

P300 amplitudes and $AvgL_{sum}$ were significantly positively correlated in all subjects (**Figure 3.7a**). While significance was mostly based on the large number of trials, the explained variance (r^2) was relatively low. This may point out that RQA extracts a type of information different from P300 amplitude based information. However, one needs to consider that RQA covers a much larger temporal window

(W1) than the window used for P300 extraction. Still, the correlation between mean amplitude of W1 and $AvgL_{sum}$ was extremely low (r^2<0.030). As a measure of temporal recurrence, $AvgL_{sum}$ is insensitive to the numerical sign of the signal, i.e. it does not differentiate positive and negative EEG deflections of the same amplitude and shape. Therefore, it is clear that the mean absolute amplitude of W1 and $AvgL_{sum}$ showed much higher correlation. This feature of RQA parameters is also reflected in the comparison between $frequent_{before}$ and $frequent_{after}$ tone types: Here, $AvgL_{sum}$ showed higher values for $frequent_{before}$ while N100 and mean amplitude of W1 showed higher values for $frequent_{after}$. In summary, according to the theoretical background of RQA, it may provide additional information on the electrophysiological response to an auditory oddball paradigm, however, further studies are required to determine the functional correlate of $AvgL_{sum}$ and also to ensure that $AvgL_{sum}$ is not just reflecting linear changes in signal amplitude. For example, this could be tested by exploiting experiments with variable tone probabilities, different inter-stimulus intervals and different tone frequencies and amplitudes, all known to modulate the electrophysiological response in ERP experiments.

Conclusions

In this study, a formal statistical comparison of the performance of RQA and classical amplitude based ERP analysis was provided. RQA provided a robust distinction between the two main types of trials in an auditory oddball experiment (frequent and rare tones), as well as between different subtypes of frequent tones. Minor signal corruption was observed in the presence of MRI artifacts, however, both analysis methods were affected to the same degree. Despite similar discrimination power, RQA may extract a qualitatively different type of information from the EEG

signal, as suggested by the theoretical concept of RQA. Hence, it still remained unclear if RQA should be preferred over ERP analysis, especially when considering the computational effort and the conceptual complexity of the method. Still, RQA may be used as a complementary tool in a single-trial analysis. While the physiological significance of ERP amplitudes has been studied in depth, a direct neuronal correlate of RQA parameters has not yet been defined. Particularly the comparison of combined fMRI/EEG data with variable tone probabilities, different inter-stimulus intervals and different tone frequencies and amplitudes may be useful to elucidate the different neural correlates of amplitude versus complexity measures such as provided by RQA.

CONCLUSION AND OUTLOOK

In this thesis, the potential of simultaneous EEG/fMRI is exploited with different methodological approaches. The basic principles and current state-of-the-art analysis methods of EEG and fMRI are outlined (**Chapter 1**). Such complementary data were used to address two major research questions: To investigate alterations in cerebral functional connectivity between the hippocampus and neocortex during wakefulness and different sleep stages (**Chapter 2**), and to evaluate the potential of recurrence quantification analysis to electrophysiological data (**Chapter 3**).

In **Chapter 2**, fMRI time-series of subregions of the hippocampal formation (HF) (cornu ammonis, dentate gyrus and subiculum) were extracted based on cytoarchitectonical probability maps. We observed sleep stage dependent changes in HF functional coupling. The HF was integrated to a variable extent in the default mode network (DMN) in wakefulness and light sleep stages, but not in slow wave sleep. The strongest functional connectivity between the HF and neocortex was observed in sleep stage 2 (compared with both slow wave sleep and wakefulness). We observed a strong interaction of sleep spindle occurrence and HF functional connectivity in sleep stage 2, with strongest HF/neocortical connectivity during spindles. Moreover, the cornu ammonis reveals strongest functional connectivity with the DMN during wakefulness, while the subiculum dominates connectivity to frontal brain regions during sleep stage 2. Increased connectivity between HF and neocortical regions in sleep stage 2 suggests an increased capacity for global information transfer, while connectivity in slow-wave sleep is reflecting a functional system optimal for segregated information (re-)processing. The present data may be relevant to differentiating sleep stage specific contributions to neural plasticity as proposed in models of sleep dependent memory consolidation.

In **Chapter 3**, the potential of recurrence quantification analysis (RQA) is evaluated with regards to improvements in the analysis of trial-by-trial-variability in event-related potential (ERP) experiments. For this propose, EEG data were acquired during an auditory oddball paradigm to compare the efficiency of RQA with amplitude based analysis of single trial ERPs. These methods were compared with regard to the power to distinguish between frequent and rare tones and to distinguish between subsequent trials. Further, the robustness of both methods was evaluated towards structured noise induced by simultaneous magnetic resonance imaging (MRI). RQA provided robust discrimination of rare and frequent tones and of subsequent trials based on their different signal structure. This discrimination ability was maintained when the EEG recordings were obtained in the MR scanner. In terms of power to discriminate between rare and frequent tones, RQA was not significantly superior to conventional amplitude analysis. Despite equal discrimination power, RQA measures were only weakly correlated with ERP amplitudes, suggesting that additional information on single trials may be extracted by RQA. Nevertheless, it still remains unclear if RQA is to be preferred over ERP analysis, especially when considering the computational effort and conceptual complexity of the method. Still, RQA has the potential of detecting small differences in response to identical tones when presented in a changed/altered context, i.e. dependent on their relative position to the last deviant tone. According to the present results, RQA may be used as an additional tool to obtain new insights in neurophysiological and neuroanatomical correlates of stimulus habituation and novelty processing even in combined trial-by-trial functional MRI/EEG experiments.

Nowadays, several different imaging approaches have been proposed as a tool to study metabolic, hemodynamic or electromagnetic functional activity. The

main focus of these methodologies is to identify the localization of the neuronal activity. However, the information of how the brain regions communicate with each other is also crucial to understand the functional organization of cortical regions. Therefore, we applied a seed analysis to quantify connectivity of the hippocampus with the neocortex during different sleep stages. In 2005, Eguiluz et al. [185] proposed a method to extract functional networks using fMRI and analyze them in the context of the current understanding of complex networks. In this method, the connectivity between brain regions is measured using a binary correlation matrix. In this way, a functional connectivity is established if the temporal correlation between two specific regions exceeds a positive threshold. Based on this matrix, statistical properties of the network as e.g. the efficiency and the 'cliqueness' can be calculated. Recently, this method was applied by our group to explore how physiological changes during sleep were reflected in functional connectivity and network properties [114]. This study leaded to insights about changes in consciousness in the descent to sleep and the capacity of the brain to integrate information across functional modules during sleep. Linear correlations are the most used measure of connectivity, however, it can miss an important part of functional dependence as coupling among brain regions should be considered nonlinear [186]. Therefore, one of the goals of my PhD studies was to evaluate the potential of the nonlinear method RQA to be applied to electrophysiological data and test the robustness of this method towards structured noise induced by simultaneous magnetic resonance imaging, since an important aim in neuroscience is to successfully combine fMRI and EEG recordings. In our analysis we applied RQA for three individual EEG channels, analysing changes in recurrence patterns and deterministic behaviour in data recorded during an oddball experiment. Indeed, we

also tried to apply RQA in sleep data, as well as in a modified oddball protocol with subjects just passively listening to tones. Although RQA lacked to show superiority in detecting changes in the EEG as compared with a linear amplitude based method, RQA likely provides different information, considering the weak correlation with linear based values. The recurrence plot may still be used to study generalized synchronization between channels to capture additional nonlinear changes in the neuronal networks. In 1995, Rulkov et al. [187] defined that a generalized synchronization exist "*when trajectories in the phase spaces of driving and response systems are connected by y(t) =* Ψ *(x(t)), two close states in the phase space of the response system correspond to two close states in the space of the driving system*". This could be simply calculated by the products of the recurrence plot of two different channels [188]. Linear and nonlinear changes of brain networks regarding different levels of arousal could therefore be investigated. A preliminary analysis suggested that this approach may be more powerful in detecting electrophysiological changes than the use of a single channel and also than synchronization by means of linear correlations. RQA could, therefore, still hold promise to examine the brain connectivity.

APPENDIX A2

A2.1. HF functional connectivity during wakefulness

		Brain Region	Brodmann areas, deep nuclei	Cluster size (voxel)	Peak voxel T-value	MNI coordinates		
1	L/C/R	(Posterior) cingulate, uncus, fusiform gyrus, precuneus, culmen, claustrum, thalamus, hippocampus, amygdala	R7,L20,23, 27-31,34-36,L37	7548	17.37	28	-28	-16
2	R	Inferior/middle temporal gyrus	21	322	10.93	50	2	-32
3	R	Middle/superior frontal gyrus	8	207	9.72	24	22	54
4	L/R	Anterior cingulate, medial frontal gyrus	10,32,L42	886	9.40	6	56	14
5	L	Angular gyrus	39	305	9.37	-44	-70	30
6	L	Middle/superior frontal gyrus	8	187	9.23	-22	28	52
7	R	Middle/superior temporal gyrus, angular gyrus, supramarginal gyrus	39	491	8.81	44	-64	28
8	L	Middle/superior temporal gyrus	21	298	8.25	-56	-14	-14

Table A2.1. Clusters resulting from second level random effects analysis (pFWE <10-6, extent > 150). Regions showing significant functional connectivity with all HF subregions are listed. Sorting is after T-values of the cluster peak voxel. Brodmann areas are identified for clusters covering > 3% of the respective area. Coordinates are given in MNI space. L/R/C denote the left/right hemisphere or central position, respectively.

A2.2. Sleep stage specific functional HF connectivity changes

		Brain Region	Brodmann areas, deep nuclei	Cluster size (voxel)	Peak voxel T-value	MNI coordinates		
			Wakefulness > S1					
1	L/R	Thalamus	Ventral anterior nucleus, medial dorsal nucleus	270	4.36	4	-18	8
			Wakefulness < S1					
1	R	Fusiform gyrus, culmen		291	5.08	44	-38	-24
2	L/C/R	Middle/superior occipital gyrus, cuneus	R17-R19	858	4.69	16	-82	30
3	L	Culmen		152	4.47	-22	-44	-18
4	R	Middle temporal gyrus	37,39	271	4.46	42	-68	8
5	L/C/R	Precuneus, paracentral lobule	5,L7	463	4.45	-4	54	64
6	L	Middle/superior temporal gyrus	41	99	4.11	-52	-28	2
			Wakefulness > S2					
			No suprathreshold cluster					
			Wakefulness < S2					
1	L	Transverse/middle/superior temporal gyrus, inferior frontal gyrus, insula, inferior parietal lobule	13,21,22,29,38, 40-42,44,45,47	2367	6.85	-64	-8	-4
2	L/C/R	Posterior cingulate, fusiform gyrus, inferior occipital gyrus, lingual gyrus, cuneus	17,18,L23,30	2564	6.81	8	-88	-8
3	R	Transverse/middle/superior temporal gyrus, postcentral gyrus	21,22,41-43,47	1221	5.40	68	-18	8
4	L	Precentral gyrus	1,3,4,6	381	5.12	-46	-6	56
5	L/C/R	Cingulate gyrus, paracentral lobule, medial frontal gyrus	23,R24,L31	293	4.68	6	-12	36

			Wakefulness > SWS					
1	L	Angular gyrus, supramarginal gyrus, inferior parietal lobule	39,40	659	5.55	-48	-70	30
2	R	Middle frontal gyrus		89	5.50	42	52	-6
3	R	Angular gyrus, supramarginal gyrus, inferior/superior parietal lobule	39,40	628	4.83	46	-66	28
4	L/R	Anterior cingulate, medial frontal gyrus	10,L32	744	4.77	10	48	-10
5	L	Inferior/medial frontal gyrus	25,47	119	4.64	-20	20	-20
6	L/C/R	(Posterior) cingulate, precuneus	L7,L23,L30,L31	300	4.10	-4	-52	24
7	L	Inferior/middle frontal gyrus	47	60	3.91	-32	32	-18
8	R	Inferior/middle frontal gyrus		43	3.84	36	34	-12
9	R	Inferior/middle/medial fronatl gyrus		39	3.77	22	24	-18
			Wakefulness < SWS					
			No suprathreshold cluster					
			S2 > SWS					
1	R	Transverse/middle/superior temporal gyrus, inferior frontal gyrus	21,22,29,41,47	727	5.30	66	-12	-6
2	L	Inferior/medial frontal gyrus	25,47	249	4.89	-28	24	-20
3	L	Transverse/superior temporal gyrus, inferior frontal gyrus	21,22,41-43,45,47	827	4.71	-58	-22	8
4	L/C/R	Posterior cingulate, lingual gyrus, cuneus	30	647	4.40	8	-88	-8

5	L/R	Orbital gyrus	11	263	4.39	8	52	-20
6	L/C	Precuneus	5,7	454	4.33	-4	-52	64
7	L/R	Superior/medial frontal gyrus	L9	197	4.27	-2	58	32
8	R	Pre-/postcentral gyrus	3,4	462	4.20	62	-10	30
		S2 < SWS						
		No suprathreshold cluster						

Table A2.2. Clusters resulting from second level random effects analysis ($p_{FWE,cluster}$<0.05, collection threshold p_{uncorr}<0.001). Regions showing significant functional connectivity with all HF subregions are listed. Sorting is after T-values of the cluster peak voxel. Brodmann areas are identified for clusters covering > 3% of the respective area. Coordinates are given in MNI space. L/R/C denote the left/right hemisphere or central position, respectively.

A2.3. Subregional HF functional connectivity per sleep stage.

		Brain Region	Brodmann areas, deep nuclei	Cluster size (voxel)	Peak voxel T-value	Peak voxel MNI coordinates		
			Wakefulness					
			CA					
1	R	Sub-gyral, uncus, fusiform gyrus, inferior temporal gyrus, extra-nuclear, lentiform nucleus, claustrum, caudate, hippocampus, amygdala, lateral globus pallidus, putamen	19-21,27,28,34-39	4151	12.30	32	-10	-20
2	L	Uncus, fusiform gyrus, middle occipital gyrus, culmen, extra-nuclear, lentiform nucleus, claustrum, caudate, hippocampus, amygdala, lateral globus pallidus, putamen	20,28,34-37	3063	11.91	-26	-10	-20
3	L	Inferior/middle temporal gyrus	21, 22	702	5.48	-58	-24	-10
4	L	Parahippocampal gyrus, thalamus	27	99	5.22	-14	-38	4
5	R	putamen		67	4.88	22	4	6
6	L	Inferior frontal gyrus	47	350	4.85	-30	34	-12
7	L/R	Thalamus	Medial/lateral dorsal nucleus, midline nucleus	196	4.60	-12	-12	18
8	L/C/R	Anterior cingulate	25	101	4.46	2	8	-8
9	R	Insula, claustrum	13	132	4.36	40	-10	16
10	L/C	Posterior cingulate	23,29,30,31	230	4.35	-4	-52	18
11	R	Superior parietal lobule		71	4.31	24	-48	58
12	C	Midbrain		47	4.31	-2	-26	-18
13	L/R	Anterior cingulate, medial frontal gyrus	32	330	4.29	0	58	6
14	R	Middle/superior temporal gyrus		56	4.25	70	-38	8

15	L	Superior frontal gyrus		74	4.12	-14	50	40
16	R	Precentral gyrus		64	4.12	56	0	30
17	R	Middle/superior temporal gyrus	39	69	4.10	52	-60	24
18	L	Angular gyrus	39	144	3.91	-40	-66	26
19	R	Inferior/middle frontal gyrus		53	3.78	38	36	-14
20	R	Middle temporal gyrus	21	67	3.76	66	-22	-10
			S1					
			CA					
1	L	Uncus, fusiform gyrus, culmen, hippocampus, amygdala, caudate tail, lateral globus pallidus, putamen	20,28,34-37	2463	12.31	-32	-14	-20
2	R	Sub-gyral, uncus, fusiform gyrus, inferior/middle temporal gyrus, culmen, claustrum, hippocampus, amygdala, caudate tail, lateral globus pallidus	20-22,28,34-38	4055	11.36	36	-16	-18
3	L	Inferior/middle/superior temporal gyrus	21,38	1120	4.89	-54	-26	0
4	R	Inferior/middle temporal gyrus	37,39	294	4.82	58	-66	-2
5	L/C	Precuneus, paracentral lobule	5	375	4.81	-4	-44	62
6	R	Middle/superior temporal gyrus	21,22	195	4.66	68	-36	0
			S2					
			CA					
1	L/C/R	Sub-gyral, uncus, fusiform gyrus, inferior occipital gyrus, inferior temporal gyrus, insula, lingual gyrus, middle/superior temporal gyrus, extra-nuclear, lentiform nucleus, claustrum, hippocampus,	13,19,20-22,28, 34-38,42	6066	10.62	26	-12	-16

		amygdala, caudate tail, putamen, lateral globus pallidus						
2	L	Sub-gyral, transverse temporal gyrus, uncus, fusiform gyrus, inferior occipital gyrus, inferior temporal gyrus, insula, lingual gyrus, middle occipital gyrus, middle temporal gyrus, culmen, claustrum, hippocampus, amygdala, caudate tail, lateral globus pallidus, putamen	19-22,28,34-38,41, 42	5796	10.56	-34	-12	-22
3	L	Lingual gyrus	17	193	5.38	-6	-92	-8
4	L	Superior temporal gyrus, supramarginal gyrus, inferior parietal lobule	13,40	415	4.99	-54	-46	20
5	L	Inferior frontal gyrus	47	280	4.9	-40	28	-14
6	R	Lingual gyrus		145	4.31	12	-82	-16
7	R	Claustrum, lentiform nucleus		174	4.26	-24	16	2
8	L	Precentral gyrus		201	4.18	-60	0	32
		DG						
1	R	Inferior temporal gyrus		76	4.72	52	-24	24
2	R	Thalamus, hippocampus	27	165	7.57	22	-36	4
3	L	Thalamus, hippocampus	27	130	7.10	-24	-36	0
		SUB						
1	L/R	Anterior cingulate, superior/medial frontal gyrus	9,10,32	1892	4.69	8	40	8
2	L	Middle/superior frontal gyrus		247	3.91	-30	40	20
		SW						

			CA					
1	R	Sub-gyral, uncus, fusiform gyrus, middle/superior/inferior temporal gyrus, hippocampus, amygdala, caudate tail	20,21,28,34-36,38	2834	11.15	34	-18	-16
2	L	Sub-gyral, uncus, fusiform gyrus, inferior temporal gyrus, middle/superior temporal gyrus, hippocampus, amygdala, caudate, lateral globus pallidus	20- 22,28,34-37	3162	10.99	-26	-10	-22
3	L	Superior/inferior frontal lobe	38	138	4.80	-44	24	-18
			DG					
1	R	Thalamus	27	111	5.51	26	-32	0
2	L/C/R	Posterior cingulate, cuneus, precuneus	18,31	486	5.46	-20	-68	14
			SUB					
1	R	Parahippocampal gyrus	28,35	241	4.78	28	-8	-32
2	R	Superior/medial frontal gyrus		127	4.31	14	38	46
3	L	Pre-/postcentral gyrus	2-4	279	4.24	-34	-28	54
4	R	Middle/superior frontal gyrus	6	142	3.97	26	8	60

Table A2.3. Clusters resulting from second level random effects analysis ($p_{FWE,cluster}<0.05$, collection threshold $p_{uncorr}<0.001$). Regions showing significant stronger functional connectivity with the specified HF subregions as compared to the other two subregions are listed (cornu ammonis, CA; dentate gyrus, DG; subiculum, SUB). Sorting is after T-values of the cluster peak voxel. Brodmann areas are identified for clusters covering > 3% of the respective area. Coordinates are given in MNI space. L/R/C denote the left/right hemisphere or central position, respectively.

A2.4 Activity related to fast sleep spindles (14 - 16 Hz)

		Brain Region	Brodmann areas, deep nuclei	Cluster size (voxel)	Peak voxel T-value	MNI coordinates		
1	L/C/R	Cingulate, posterior/anterior cingulate, precuneus, paracentral lobule, postcentral gyrus, superior/medial frontal gyrus	5-7,10,23,24,29, 31,32,42	5588	4.89	10	26	28
2	R	Transverse/superior temporal gyrus, insula	13,22,41,42	569	4.77	58	-20	10
3	L/C/R	Lingual gyrus, cuneus	17,18	925	4.71	14	-98	0
4	L	Pre-/post-central gyrus	2-4	440	4.66	-30	-28	64
5	R	Superior frontal gyrus	9	345	4.50	26	44	46
6	L	Transverse temporal gyrus*	41	103	4.12	-44	-30	10
7	R	Thalamus		195	4.10	6	-8	4
8	R	Postcentral gyrus	3-5	225	3.86	32	-32	62
9	L	Supramarginal gyrus*		116	3.79	-54	-46	30

Table A2.4. Clusters resulting from second level random effects analysis ($p_{FWE,cluster} < 0.05$, collection threshold $p_{uncorr} < 0.001$). Sorting is after T-values of the cluster peak voxel. Brodmann areas are identified for clusters covering > 3% of the respective area. Coordinates are given in MNI space. L/C/R denotes left/central/right clusters. (*) marks two clusters which do not reach statistical significance, but only trend values $p_{FWE,cluster} < 0.1$. L/R/C denote the left/right hemisphere or central position, respectively.

A2.5. Activity related to the interaction effect of *Spindle* × *SUB*

		Brain Region	Brodmann areas, deep nuclei	Cluster size (voxel)	Peak voxel T-value	MNI coordinates		
1	L/C/R	(Posterior) cingulate, Subcallosal gyrus, sub-gyral, transverse/inferior/middle/ superior temporal gyrus, uncus, fusiform gyrus, insula, lingual gyrus, pre-/post-central gyrus, paracentral lobule, inferior/middle/medial frontal gyrus, inferior/superior parietal lobule, precuneus, culmen, thalamus, extra-nuclear, lentiform, claustrum, hippocampus, amygdala, putamen	1-7,9,13,19,20-24, 28-47	21386	14.15	32	-22	-22
2	L	Transverse/middle/superior temporal gyrus, insula, pre-/post-central gyrus, inferior frontal gyrus, inferior parietal lobule, extra-nuclear, claustrum, putamen	6,9,13,22,29,38, 41-45,47	5279	11.86	-56	2 -6	
3	L	Thalamus, hippocampus, amygdala	27,28,30,34-37	1288	9.56	-24	-20	-20
4	L/C	Inferior/middle occipital gyrus, cuneus	18	404	7.83	-24	-98	6
5	R	Inferior occipital gyrus		329	7.08	34	-76	-10
6	L	Superior frontal gyrus	8,9	518	6.40	-26	38	48
7	L/R	Anterior cingulate, medial frontal gyrus	10,32,42	897	6.24	2	48	12
8	R	Superior frontal gyrus	8,9	387	5.81	14	46	52

Table A2.5. Clusters resulting from second level random effects analysis ($p_{uncorr}<10^{-4}$, extent>150 voxel). Sorting is after T-values of the cluster peak voxel. Brodmann areas are identified for clusters covering > 3% of the respective area. Coordinates are given in MNI space. L/C/R denotes left/central/right clusters.

A2.6. Activity related to the interaction effect of *Spindle* × *FD*

		Brain Region	Brodmann areas, deep nuclei	Cluster size (voxel)	Peak voxel T-value	MNI coordinates		
1	L/R	Posterior cingulate, sub-gyral, transverse/inferior/middle/superior temporal gyrus, fusiform gyrus, inferior/middle occipital gyrus, insula, lingual gyrus, pre-/post-central gyrus, inferior/superior/medial frontal gyrus, cuneus, angular gyrus, inferior parietal lobule, paracentral lobule, declive, culmen, extra-nuclear, claustrum, thalamus, hippocampus	1-7,9,13,17-19, 21-24,27-31, 35-44	22287	14.59	-22	-34	-4
2	L/C	Inferior/middle occipital gyrus, Lingual gyrus, cuneus	17, 18, 19	1006	8.26	-22	-102	4
3	L	Fusiform gyrus	37	248	6.25	-44	-46	-22
4	L	Inferior temporal gyrus	37	188	5.42	-54	-74	4

Table A2.6. Clusters resulting from second level random effects analysis ($p_{uncorr}<10^{-4}$, extent>150 voxel). Sorting is after T-values of the cluster peak voxel. Brodmann areas are identified for clusters covering > 3% of the respective area. Coordinates are given in MNI space. L/C/R denotes left/central/right clusters.

A2.7. Activity related to the interaction effect of *Spindle* × *CA*

		Brain Region	Brodmann areas, deep nuclei	Cluster size (voxel)	Peak voxel T-value	MNI coordinates		
1	L	Fusiform gyrus, lingual gyrus, middle occipital gyrus, cuneus, hippocampus, amygdala	17-20,28,34-37	1581	8.97	-26	-28	-16
2	R	Uncus, fusiform gyrus, inferior temporal gyrus, culmen, hippocampus, amygdala	19-22,27,28,34-37	2803	8.42	22	-12	-24
3	L	Precentral gyrus	43	226	7.65	-58	0	28
4	L	Superior temporal gyrus	22	310	6.78	-46	-48	16
5	L	Superior temporal gyrus	22	418	6.31	-58	-2	-4
6	C	Paracentral lobule, medial frontal gyrus		186	6.23	4	-14	50
7	R	Middle temporal gyrus		232	5.97	36	-68	-2

Table A2.7. Clusters resulting from second level random effects analysis ($p_{uncorr}<10^{-4}$, extent>150 voxel). Sorting is after T-values of the cluster peak voxel. Brodmann areas are identified for clusters covering > 3% of the respective area. Coordinates are given in MNI space. L/C/R denotes left/central/right clusters.

APPENDIX A3

A3.1 Higher effect sizes found for each subject with optimized m and d values

	Undistorted EEG recordings			Distorted EEG recordings during an fMRI scan		
Subjects	***m***	***d***	**Effect size**	***m***	***d***	**Effect size**
1	3	10	1.03	5	8	0.68
2	3	14	1.28	11	3	0.63
3	4	11	0.97	5	12	0.70
4	3	10	1.48	4	9	0.88
5	3	16	1.26	2	10	1.19
6	4	7	0.98	7	6	0.78
7	3	16	1.03	3	7	0.76
8	3	16	1.00	5	8	0.52
9	3	18	0.77	5	7	1.08

Table A3.1a. Cohen's effect sizes (rare vs. frequent tones) for m and d individually optimized for each subject.

REFERENCES

[1] Dolan,R.J., Neuroimaging of Cognition: Past, Present, and Future. Neuron 60 (2008) 496-502.

[2] Buxton,R.B., Interpreting oxygenation-based neuroimaging signals: the importance and the challenge of understanding brain oxygen metabolism. Frontiers in Neuroenergetics 2 (2010) e8.

[3] Logothetis,N.K., Wandell,B.A., Interpreting the BOLD signal. Annual Review of Physiology 66 (2004) 735-769.

[4] Shibasaki,H., Human brain mapping: Hemodynamic response and electrophysiology. Clinical Neurophysiology 119 (2008) 731-743.

[5] Ritter,P., Villringer,A., Simultaneous EEG-fMRI. Neuroscience & Biobehavioral Reviews 30 (2006) 823-838.

[6] Bandettini,P.A., What's New in Neuroimaging Methods? Year in Cognitive Neuroscience 2009 1156 (2009) 260-293.

[7] Czisch,M., Wetter,T.C., Kaufmann,C., Pollmächer,T., Holsboer,F., Auer,D.P., Altered processing of acoustic stimuli during sleep: Reduced auditory activation and visual deactivation detected by a combined fMRI/EEG study. Neuroimage 16 (2002) 251-258.

[8] Laufs,H., Kleinschmidt,A., Beyerle,A., Eger,E., Salek-Haddadi,A., Preibisch,C., Krakow,K., EEG-correlated fMRI of human alpha activity. Neuroimage 19 (2003) 1463-1476.

[9] Czisch,M., Wehrle,R., Kaufmann,C., Wetter,T.C., Holsboer,F., Pollmächer,T., Auer,D.P., Functional MRI during sleep: BOLD signal decreases and

their electrophysiological correlates. European Journal of Neuroscience 20 (2004) 566-574.

[10] Kaufmann,C., Wehrle,R., Wetter,T.C., Holsboer,F., Auer,D.P., Pollmächer,T., Czisch,M., Brain activation and hypothalamic functional connectivity during human non-rapid eye movement sleep: an EEG/fMRI study. Brain 129 (2006) 655-667.

[11] Laufs,H., Holt,J.L., Elfont,R., Krams,M., Paul,J.S., Krakow,K., Kleinschmidt,A., Where the BOLD signal goes when alpha EEG leaves. Neuroimage 31 (2006) 1408-1418.

[12] Bloch,F., Hansen,W.W., Packard,M., Nuclear Induction. Physical Review 69 (1946) 127.

[13] Purcell,E.M., Torrey,H.C., Pound,R.V., Resonance Absorption by Nuclear Magnetic Moments in A Solid. Physical Review 69 (1946) 37-38.

[14] Lauterbur,P.C., Image Formation by Induced Local Interactions - Examples Employing Nuclear Magnetic-Resonance. Nature 242 (1973) 190-191.

[15] Haacke,E.M., Brown,R.W., Thompson,M.R. and Venkatesan,R., Magnetic resonance imaging: physical principles and sequence design, J. Wiley & Sons, New York, (1999).

[16] Ogawa,S., Lee,T.M., Magnetic resonance imaging of blood vessels at high fields: in vivo and in vitro measurements and image simulation. Magnetic Resonance in Medicine 16 (1990) 9-18.

[17] Ogawa,S., Lee,T.M., Nayak,A.S., Glynn,P., Oxygenation-sensitive contrast in magnetic resonance image of rodent brain at high magnetic fields. Magnetic Resonance in Medicine 14 (1990) 68-78.

[18] Herson R., Büchel C., Josephs O. and Friston K., The Slice-Timing Problem in Event-related fMRI. In: Human Brain Mapping Conference, (1999).

[19] van Strien N., MRI-tutorial: A neuroimaging repository (2009), Retrieved from http://www.mri-tutorial.com/index.php.

[20] MRIcro tutorial (2011), Retrieved from http://www.cabiatl.com/mricro/mricro/mritut.html#ViewingIMG.

[21] Hutton, C, fMRI analysis: preprocessing: coresgistration and spatial normalization (2-27-2009), Retrieved from http://www.fil.ion.ucl.ac.uk/spm/doc/mfd/2009/.

[22] Brodmann,K., Vergleichende Lokalisationslehre der Grosshirnrinde in ihren Prinzipien dargestellt auf Grund des Zellenbaues, Johann Ambrosius Barth Verlag, Leipzig, (1909).

[23] Brodman areas (8-7-2010), Retrieved from http://www.mrc-cbu.cam.ac.uk/people/jessica.grahn/neuroanatomy.html.

[24] Friston,K.J., Penny,W., Phillips,C., Kiebel,S., Hinton,G., Ashburner,J., Classical and Bayesian inference in neuroimaging: Theory. Neuroimage 16 (2002) 465-483.

[25] Friston,K., Holmes,A., Worsley,K., Poline,J., Frith,C., Frackowiak,R., Statistical parametric maps in functional imaging: A general linear approach. Human Brain Mapping 2 (1994) 189-210.

[26] Raichle,M.E., A Paradigm Shift in Functional Brain Imaging. Journal of Neuroscience 29 (2009) 12729-12734.

[27] McKeown,M.J., Makeig,S., Brown,G.G., Jung,T.P., Kindermann,S.S., Bell,A.J., Sejnowski,T.J., Analysis of fMRI data by blind separation into independent spatial components. Human Brain Mapping 6 (1998) 160-188.

[28] Reijneveld,J.C., Ponten,S.C., Berendse,H.W., Stam,C.J., The application of graph theoretical analysis to complex networks in the brain. Clinical Neurophysiology 118 (2007) 2317-2331.

[29] Bullmore,E., Sporns,O., Complex brain networks: graph theoretical analysis of structural and functional systems. Nature Reviews Neuroscience 10 (2009) 186-198.

[30] Berger,H., Über das Elektrenkephalogramm des Menschen. Archiv fur Psychiatrie und Nervenkrankheiten 87 (1929) 527-570.

[31] Holmes,G. and Khazipov,R., Basic Neurophysiology and the Cortical Basis of EEG. In: A.S.Blum, S.B.Rutkove (Eds.), The Clinical Neurophysiology Primer, Humana Press, (2007) 19-33.

[32] da Silva,F.L., EEG: Origin and Measurement. In: C.Mulert, L.Lemieux (Eds.), EEG-fMRI Physiological Basis, Technique, and Application, Springer, (2010) 20-35.

[33] Michel,C.M., Murray,M.M., Lantz,G.r., Gonzalez,S., Spinelli,L., Grave de Peralta,R., EEG source imaging. Clinical Neurophysiology 115 (2004) 2195-2222.

[34] User Tutorial: EEG Measurement Setup (8-14-2009), Retrieved from http://www.bci2000.org/wiki/index.php/User_Tutorial:EEG_Measurement_Setup.

[35] Easycap Products (1-25-2011), Retrieved from http://www.easycap.de/easycap/e/products/products.htm.

[36] Nakamura,M., Chen,Q., Sugi,T., Ikeda,A., Shibasaki,H., Technical quality evaluation of EEG recording based on electroencephalographers' knowledge. Medical Engineering & Physics 27 (2005) 93-100.

[37] Hennighausen,E., Heil,M., Rosler,F., A Correction Method for Dc Drift Artifacts. Electroencephalography and Clinical Neurophysiology 86 (1993) 199-204.

[38] Allen,P.J., EEG Instrumentation and Safety. In: C.Mulert, L.Lemieux (Eds.), EEG-fMRI Physiological Basis, Technique, and Application, Springer, (2010) 115-133.

[39] Lemieux,L., Allen,P.J., Franconi,F., Symms,M.R., Fish,D.R., Recording of EEG during fMRI experiments: Patient safety. Magnetic Resonance in Medicine 38 (1997) 943-952.

[40] Roth,B.J., Pascualleone,A., Cohen,L.G., Hallett,M., The Heating of Metal-Electrodes During Rapid-Rate Magnetic Stimulation - A Possible Safety Hazard. Electroencephalography and Clinical Neurophysiology 85 (1992) 116-123.

[41] Stevens,T.K., Ives,J.R., Klassen,L.M., Bartha,R., MR compatibility of EEG scalp electrodes at 4 Tesla. Journal of Magnetic Resonance Imaging 25 (2007) 872-877.

[42] Mirsattari,S.M., Lee,D.H., Jones,D., Bihari,F., Ives,J.R., MRI compatible EEG electrode system for routine use in the epilepsy monitoring unit and intensive care unit. Clinical Neurophysiology 115 (2004) 2175-2180.

[43] Gutberlet, I, Did you know...? MR Correction, in Press Release (2007), Retrieved from http://www.brainproducts.com/pressrelease.php?tab=2&year=2007.

[44] Mandelkow,H., Halder,P., Boesiger,P., Brandeis,D., Synchronization facilitates removal of MRI artefacts from concurrent EEG recordings and increases usable bandwidth. Neuroimage 32 (2006) 1120-1126.

[45] Allen,P.J., Josephs,O., Turner,R., A method for removing imaging artifact from continuous EEG recorded during functional MRI. Neuroimage 12 (2000) 230-239.

[46] Ives,J.R., Warach,S., Schmitt,F., Edelman,R.R., Schomer,D.L., Monitoring the Patients Eeg During Echo-Planar Mri. Electroencephalography and Clinical Neurophysiology 87 (1993) 417-420.

[47] Allen,P.J., Polizzi,G., Krakow,K., Fish,D.R., Lemieux,L., Identification of EEG events in the MR scanner: The problem of pulse artifact and a method for its subtraction. Neuroimage 8 (1998) 229-239.

[48] Yan,W.X., Mullinger,K.J., Geirsdottir,G.B., Bowtell,R., Physical Modeling of Pulse Artefact Sources in Simultaneous EEG/fMRI. Human Brain Mapping 31 (2010) 604-620.

[49] Briselli,E., Garreffa,G., Bianchi,L., Bianciardi,M., Macaluso,E., Abbafati,M., Grazia Marciani,M., Maraviglia,B., An independent component analysis-based approach on ballistocardiogram artifact removing. Magnetic Resonance Imaging 24 (2006) 393-400.

[50] Czisch,M., Wehrle,R., Stiegler,A., Peters,H., Andrade,K., Holsboer,F., Samann,P.G., Acoustic Oddball during NREM Sleep: A Combined EEG/fMRI Study. Plos One 4 (2009) e6749.

[51] Cardoso,J.F., Blind signal separation: Statistical principles. Proceedings of the IEEE 86 (1998) 2009-2025.

[52] Dang-Vu,T.T., Desseilles,M., Petit,D., Mazza,S., Montplaisir,J., Maquet,P., Neuroimaging in sleep medicine. Sleep Medicine 8 (2007) 349-372.

[53] Staner,L., Comorbidity of insomnia and depression. Sleep Medicine Reviews 14 (2010) 35-46.

[54] Cohrs,S., Sleep Disturbances in Patients with Schizophrenia Impact and Effect of Antipsychotics. CNS Drugs 22 (2008) 939-962.

[55] Briones,B., Adams,N., Strauss,M., Rosenberg,C., Whalen,C., Carskadon,M., Roebuck,T., Winters,M., Redline,S., Relationship between sleepiness and general health status. Sleep 19 (1996) 583-588.

[56] Loomis,A.L., Harvey,E.N., Hobart,G.A., Cerebral states during sleep, as studied by human brain potentials. Journal of Experimental Psychology 21 (1937) 127-144.

[57] Rechtschaffen,A., Kales,A.A., A manual of standardized terminology, techniques and scoring system for sleep stages of human subjects. Washington D. C. , NIH publication no. 204 (1968).

[58] Oken,B.S., Salinsky,M.C., Elsas,S.M., Vigilance, alertness, or sustained attention: physiological basis and measurement. Clinical Neurophysiology 117 (2006) 1885-1901.

[59] Susmakova,K., Human Sleep and Sleep EEG. Measurement science review 4 (2004) 59-74.

[60] Yang,C.M., Han,H.Y., Yang,M.H., Su,W.C., Lane,T., What subjective experiences determine the perception of falling asleep during sleep onset period? Consciousness and Cognition 19 (2010) 1084-1092.

[61] Ogilvie,R.D., Simons,I.A., Kuderian,R.H., Macdonald,T., Rustenburg,J., Behavioral, Event-Related Potential, and EEG FFT Changes at Sleep Onset. Psychophysiology 28 (1991) 54-64.

[62] Jan,J.E., Reiter,R.J., Wasdell,M.B., Bax,M., The role of the thalamus in sleep, pineal melatonin production, and circadian rhythm sleep disorders. Journal of Pineal Research 46 (2009) 1-7.

[63] Czisch,M. and Wehrle,R., Sleep. In: C.Mulert, L.Lemieux (Eds.), EEG-fMRI Physiological Basis, Technique, and Application, Springer, (2010) 279-305.

[64] Schabus,M., Dang-Vu,T.T., Albouy,G., Balteau,E., Boly,M., Carrier,J., Darsaud,A., Degueldre,C., Desseilles,M., Gais,S., Phillips,C., Rauchs,G., Schnakers,C., Sterpenich,V., Vandewalle,G., Luxen,A., Maquet,P., Hemodynamic cerebral correlates of sleep spindles during human non-rapid eye movement sleep. Proceedings of the National Academy of Sciences of the United States of America 104 (2007) 13164-13169.

[65] Cote,K.A., Epps,T.M., Campbell,K.B., The role of the spindle in human information processing of high-intensity stimuli during sleep. Journal of Sleep Research 9 (2000) 19-26.

[66] Steriade,M., McCormick,D.A., Sejnowski,T.J., Thalamocortical oscillations in the sleeping and aroused brain. Science 262 (1993) 679-685.

[67] Bryant,P.A., Trinder,J., Curtis,N., Sick and tired: Does sleep have a vital role in the immune system? Nature Reviews Immunology 4 (2004) 457-467.

[68] Maquet,P., Sleep function(s) and cerebral metabolism. Behavioural Brain Research 69 (2007) 75-83.

[69] Vassalli,A., Dijk,D.J., Sleep function: current questions and new approaches. European Journal of Neuroscience 29 (2009) 1830-1841.

[70] Axmacher,N., Draguhn,A., Elger,C.E., Fell,J., Memory processes during sleep: beyond the standard consolidation theory. Cellular and Molecular Life Sciences 66 (2009) 2285-2297.

[71] Born,J., Rasch,B., Gais,S., Sleep to remember. Neuroscientist 12 (2006) 410-424.

[72] Walker,M.P., The role of sleep in cognition and emotion. Annals of the New York Academy of Sciences 1156 (2009) 168-197.

[73] Rasch,B., Buchel,C., Gais,S., Born,J., Odor cues during slow-wave sleep prompt declarative memory consolidation. Science 315 (2007) 1426-1429.

[74] Sutherland,G.R., McNaughton,B., Memory trace reactivation in hippocampal and neocortical neuronal ensembles. Current Opinion in Neurobiology 10 (2000) 180-186.

[75] Diekelmann,S., Born,J., The memory function of sleep. Nature Reviews Neuroscience 11 (2010) 114-126.

[76] Walker,M.P., Stickgold,R., Sleep-dependent learning and memory consolidation. Neuron 44 (2004) 121-133.

[77] Wagner,U., Gais,S., Born,J., Emotional memory formation is enhanced across sleep intervals with high amounts of rapid eye movement sleep. Learning & Memory 8 (2001) 112-119.

[78] Plihal,W., Born,J., Effects of early and late nocturnal sleep on priming and spatial memory. Psychophysiology 36 (1999) 571-582.

[79] Plihal,W., Born,J., Effects of early and late nocturnal sleep on declarative and procedural memory. Journal of Cognitive Neuroscience 9 (1997) 534-547.

[80] Fogel,S.M., Smith,C.T., Cote,K.A., Dissociable learning-dependent changes in REM and non-REM sleep in declarative and procedural memory systems. Behavioural Brain Research 180 (2007) 48-61.

[81] Rauchs,G., Bertran,F., Guillery-Girard,B., Desgranges,B., Kerrouche,N., Denise,P., Foret,J., Eustache,F., Consolidation of strictly episodic memories mainly requires rapid eye movement sleep. Sleep 27 (2004) 395-401.

[82] Gais,S., Plihal,W., Wagner,U., Born,J., Early sleep triggers memory for early visual discrimination skills. Nature Neuroscience 3 (2000) 1335-1339.

[83] Rasch,B., Pommer,J., Diekelmann,S., Born,J., Pharmacological REM sleep suppression paradoxically improves rather than impairs skill memory. Nature Neuroscience 12 (2009) 396-397.

[84] Smith,C., Macneill,C., Impaired Motor Memory for A Pursuit Rotor Task Following Stage-2 Sleep Loss in College-Students. Journal of Sleep Research 3 (1994) 206-213.

[85] Molle,M., Marshall,L., Gais,S., Born,J., Learning increases human electroencephalographic coherence during subsequent slow sleep oscillations. Proceedings of the National Academy of Sciences of the United States of America 101 (2004) 13963-13968.

[86] Schabus,M., Gruber,G., Parapatics,S., Sauter,C., Klosch,G., Anderer,P., Klimesch,W., Saletu,B., Zeitlhofer,J., Sleep spindles and their significance for declarative memory consolidation. Sleep 27 (2004) 1479-1485.

[87] Molle,M., Born,J., Hippocampus Whispering in Deep Sleep to Prefrontal Cortex - For Good Memories? Neuron 61 (2009) 496-498.

[88] Durrant,S., Lewis,P.A., Memory Consolidation: Tracking Transfer with Functional Connectivity. Current Biology 19 (2009) R860-R862.

[89] Girardeau,G., Benchenane,K., Wiener,S.I., Buzsaki,G., Zugaro,M.B., Selective suppression of hippocampal ripples impairs spatial memory. Nature Neuroscience 12 (2009) 1222-1223.

[90] Hasselmo,M.E., McClelland,J.L., Neural models of memory. Current Opinion in Neurobiology 9 (1999) 184-188.

[91] Squire,L.R., Memory systems of the brain: a brief history and current perspective. Neurobiology of Learning and Memory 82 (2004) 171-177.

[92] Takashima,A., Nieuwenhuis,I.L., Jensen,O., Talamini,L.M., Rijpkema,M., Fernandez,G., Shift from hippocampal to neocortical centered retrieval network with consolidation. Journal of Neuroscience 29 (2009) 10087-10093.

[93] Clemens,Z., Molle,M., Eross,L., Barsi,P., Halasz,P., Born,J., Temporal coupling of parahippocampal ripples, sleep spindles and slow oscillations in humans. Brain 130 (2007) 2868-2878.

[94] Siapas,A.G., Wilson,M.A., Coordinated interactions between hippocampal ripples and cortical spindles during slow-wave sleep. Neuron 21 (1998) 1123-1128.

[95] O'Neill,J., Pleydell-Bouverie,B., Dupret,D., Csicsvari,J., Play it again: reactivation of waking experience and memory. Trends in Neurosciences 33 (2010) 220-229.

[96] Buckner,R.L., The role of the hippocampus in prediction and imagination. Annual Review of Psychology 61 (2010) 27-28.

[97] Amunts,K., Kedo,O., Kindler,M., Pieperhoff,P., Mohlberg,H., Shah,N.J., Habel,U., Schneider,F., Zilles,K., Cytoarchitectonic mapping of the human amygdala, hippocampal region and entorhinal cortex: intersubject variability and probability maps. Anatomy and Embryology (Berl) 210 (2005) 343-352.

[98] McNaughton,N., The role of the subiculum within the behavioural inhibition system. Behavioural Brain Research 174 (2006) 232-250.

[99] Levita,L., Muzzio,I.A., Role of the hippocampus in goal-oriented tasks requiring retrieval of spatial versus non-spatial information. Neurobiology of Learning and Memory 93 (2010) 581-588.

[100] Tejada,S., Gonzalez,J.J., Rial,R.V., Coenen,A.M.L., Gamundi,A., Esteban,S., Electroencephalogram Functional Connectivity Between Rat Hippocampus and Cortex After Pilocarpine Treatment. Neuroscience 165 (2010) 621-631.

[101] Witter,M.P., Connectivity of the Hippocampus. In: V.Cutsuridis, B.Graham, S.Cobb, I.Vida (Eds.), Hippocampal Microcircuits, Springer, New York, (2010) 5-26.

[102] Fox,M.D., Raichle,M.E., Spontaneous fluctuations in brain activity observed with functional magnetic resonance imaging. Nature Reviews Neurosciscience 8 (2007) 700-711.

[103] Jann,K., Kottlow,M., Dierks,T., Boesch,C., Koenig,T., Topographic Electrophysiological Signatures of fMRI Resting State Networks. Plos One 5 (2010) e12945.

[104] Buckner,R.L., Andrews-Hanna,J.R., Schacter,D.L., The brain's default network: anatomy, function, and relevance to disease. Annals of the New York Academy of Sciences 1124 (2008) 1-38.

[105] Vincent,J.L., Snyder,A.Z., Fox,M.D., Shannon,B.J., Andrews,J.R., Raichle,M.E., Buckner,R.L., Coherent spontaneous activity identifies a hippocampal-parietal memory network. Journal of Neurophysiology 96 (2006) 3517-3531.

[106] Larson-Prior,L.J., Zempel,J.M., Nolan,T.S., Prior,F.W., Snyder,A.Z., Raichle,M.E., Cortical network functional connectivity in the descent to sleep. Proceedings of the National Academy of Sciences of the United States of America 106 (2009) 4489-4494.

[107] Horovitz,S.G., Braun,A.R., Carr,W.S., Picchioni,D., Balkin,T.J., Fukunaga,M., Duyn,J.H., Decoupling of the brain's default mode network during deep sleep. Proceedings of the National Academy of Sciences of the United States of America 106 (2009) 11376-11381.

[108] Sämann,P.G., Wehrle,R., Spoormaker,V., Hoehn,D., Peters,H., Holsboer,F., Czisch,M., Development of the brain default mode network from wakefulness into slow wave sleep. Cerebral Cortex (2011) in press.

[109] Eickhoff,S.B., Stephan,K.E., Mohlberg,H., Grefkes,C., Fink,G.R., Amunts,K., Zilles,K., A new SPM toolbox for combining probabilistic cytoarchitectonic maps and functional imaging data. Neuroimage 25 (2005) 1325-1335.

[110] Brett,M., Anton,J.-L., Valabregue,R., Poline,J.-P., Region of interest analysis using an SPM toolbox. Presented at the 8th International Conference on Functional Mapping of the Human Brain, Sendai, Japan (2002).

[111] Hayasaka,S., Phan,K.L., Liberzon,I., Worsley,K.J., Nichols,T.E., Nonstationary cluster-size inference with random field and permutation methods. Neuroimage 22 (2004) 676-687.

[112] De Gennaro,L., Ferrara,M., Sleep spindles: an overview. Sleep Medicine Reviews 7 (2003) 423-440.

[113] Friston,K.J., Stephan,K.E., Lund,T.E., Morcom,A., Kiebel,S., Mixed-effects and fMRI studies. Neuroimage 24 (2005) 244-252.

[114] Spoormaker,V.I., Schroter,M.S., Gleiser,P.M., Andrade,K.C., Dresler,M., Wehrle,R., Sämann,P.G., Czisch,M., Development of a Large-Scale Functional Brain Network during Human Non-Rapid Eye Movement Sleep. Journal of Neuroscience 30 (2010) 11379-11387.

[115] Svoboda,E., McKinnon,M.C., Levine,B., The functional neuroanatomy of autobiographical memory: a meta-analysis. Neuropsychologia 44 (2006) 2189-2208.

[116] Wagner,A.D., Shannon,B.J., Kahn,I., Buckner,R.L., Parietal lobe contributions to episodic memory retrieval. Trends in Cognitive Sciences 9 (2005) 445-453.

[117] Burianova,H., McIntosh,A.R., Grady,C.L., A common functional brain network for autobiographical, episodic, and semantic memory retrieval. Neuroimage. 49 (2010) 865-874.

[118] Andrews-Hanna,J.R., Reidler,J.S., Sepulcre,J., Poulin,R., Buckner,R.L., Functional-anatomic fractionation of the brain's default network. Neuron 65 (2010) 550-562.

[119] Martuzzi,R., Ramani,R., Qiu,M., Rajeevan,N., Constable,R.T., Functional connectivity and alterations in baseline brain state in humans. Neuroimage. 49 (2010) 823-834.

[120] Gais,S., Born,J., Low acetylcholine during slow-wave sleep is critical for declarative memory consolidation. Proceedings of the National Academy of Sciences of the United States of America 101 (2004) 2140-2144.

[121] Peigneux,P., Laureys,S., Fuchs,S., Collette,F., Perrin,F., Reggers,J., Phillips,C., Degueldre,C., Del Fiore,G., Aerts,J., Luxen,A., Maquet,P., Are spatial

memories strengthened in the human hippocampus during slow wave sleep? Neuron 44 (2004) 535-545.

[122] Genzel,L., Dresler,M., Wehrle,R., Grozinger,M., Steiger,A., Slow wave sleep and REM sleep awakenings do not affect sleep dependent memory consolidation. Sleep 32 (2009) 302-310.

[123] Gais,S., Molle,M., Helms,K., Born,J., Learning-dependent increases in sleep spindle density. Journal of Neuroscience 22 (2002) 6830-6834.

[124] Nishida,M., Walker,M.P., Daytime naps, motor memory consolidation and regionally specific sleep spindles. Plos One 2 (2007) e341.

[125] Ribeiro,S., Gervasoni,D., Soares,E.S., Zhou,Y., Lin,S.C., Pantoja,J., Lavine,M., Nicolelis,M.A., Long-lasting novelty-induced neuronal reverberation during slow-wave sleep in multiple forebrain areas. PLoS Biology 2 (2004) e24.

[126] Payne,J.D., Kensinger,E.A., Sleep Leads to Changes in the Emotional Memory Trace: Evidence from fMRI. Journal of Cognitive Neuroscience (2010) epub ahead of print.

[127] Darsaud,A., Wagner,U., Balteau,E., Desseilles,M., Sterpenich,V., Vandewalle,G., Albouy,G., Dang-Vu,T., Collette,F., Boly,M., Schabus,M., Degueldre,C., Luxen,A., Maquet,P., Neural Precursors of Delayed Insight. Journal of Cognitive Neuroscience (2010) epub ahead of print.

[128] Darsaud,A., Dehon,H., Lahl,O., Sterpenich,V., Boly,M., Dang-Vu,T., Desseilles,M., Gais,S., Matarazzo,L., Peters,F., Schabus,M., Schmidt,C., Tinguely,G., Vandewalle,G., Luxen,A., Maquet,P., Collette,F., Does Sleep Promote False Memories? Journal of Cognitive Neuroscience 23 (2011) 26-40.

[129] Sterpenich,V., Albouy,G., Darsaud,A., Schmidt,C., Vandewalle,G., Dang Vu,T.T., Desseilles,M., Phillips,C., Degueldre,C., Balteau,E., Collette,F.,

Luxen,A., Maquet,P., Sleep promotes the neural reorganization of remote emotional memory. Journal of Neuroscience 29 (2009) 5143-5152.

[130] Rauchs,G., Orban,P., Schmidt,C., Albouy,G., Balteau,E., Degueldre,C., Schnackers,C., Sterpenich,V., Tinguely,G., Luxen,A., Maquet,P., Peigneux,P., Sleep modulates the neural substrates of both spatial and contextual memory consolidation. Plos One 3 (2008) e2949.

[131] Gais,S., Albouy,G., Boly,M., ng-Vu,T.T., Darsaud,A., Desseilles,M., Rauchs,G., Schabus,M., Sterpenich,V., Vandewalle,G., Maquet,P., Peigneux,P., Sleep transforms the cerebral trace of declarative memories. Proceedings of the National Academy of Sciences of the United States of America 104 (2007) 18778-18783.

[132] Wagner,T., Axmacher,N., Lehnertz,K., Elger,C.E., Fell,J., Sleep-dependent directional coupling between human neocortex and hippocampus. Cortex 46 (2010) 256-263.

[133] Sirota,A., Csicsvari,J., Buhl,D., Buzsaki,G., Communication between neocortex and hippocampus during sleep in rodents. Proceedings of the National Academy of Sciences of the United States of America 100 (2003) 2065-2069.

[134] Battaglia,F.P., Sutherland,G.R., McNaughton,B.L., Hippocampal sharp wave bursts coincide with neocortical "up-state" transitions. Learning & Memory 11 (2004) 697-704.

[135] Axmacher,N., Mormann,F., Fernandez,G., Elger,C.E., Fell,J., Memory formation by neuronal synchronization. Brain Research Reviews 52 (2006) 170-182.

[136] Schabus,M., Hoedlmoser,K., Pecherstorfer,T., Anderer,P., Gruber,G., Parapatics,S., Sauter,C., Kloesch,G., Klimesch,W., Saletu,B., Zeitlhofer,J.,

Interindividual sleep spindle differences and their relation to learning-related enhancements. Brain Research 1191 (2008) 127-135.

[137] Fogel,S.M., Smith,C.T., Learning-dependent changes in sleep spindles and Stage 2 sleep. Journal of Sleep Research 15 (2006) 250-255.

[138] Clemens,Z., Fabo,D., Halasz,P., Overnight verbal memory retention correlates with the number of sleep spindles. Neuroscience 132 (2005) 529-535.

[139] Herkenham,M., The connections of the nucleus reuniens thalami: evidence for a direct thalamo-hippocampal pathway in the rat. Journal of Comparative Neurology 177 (1978) 589-610.

[140] Wouterlood,F.G., Saldana,E., Witter,M.P., Projection from the nucleus reuniens thalami to the hippocampal region: light and electron microscopic tracing study in the rat with the anterograde tracer Phaseolus vulgaris-leucoagglutinin. Journal of Comparative Neurology 296 (1990) 179-203.

[141] Tononi,G., Cirelli,C., Sleep and synaptic homeostasis: a hypothesis. Brain Research Bulletin 62 (2003) 143-150.

[142] Dalbokova,D., Gille,H.G., Ullsperger,P., Amplitude Variations in P300 Component Due to Unpredictable Stepwise Change of Stimulus Probability. International Journal of Psychophysiology 10 (1990) 33-38.

[143] Polich,J., Alexander,J.E., Bauer,L.O., Kuperman,S., Morzorati,S., OConnor,S.J., Porjesz,B., Rohrbaugh,J., Begleiter,H., P300 topography of amplitude/latency correlations. Brain Topography 9 (1997) 275-282.

[144] Ma,Q.G., Wang,X.Y., Shu,L.C., Dai,S.Y., P300 and categorization in brand extension. Neuroscience Letters 431 (2008) 57-61.

[145] Polich,J., Updating p300: An integrative theory of P3a and P3b. Clinical Neurophysiology 118 (2007) 2128-2148.

[146] Rosburg,T., Boutros,N.N., Ford,J.M., Reduced auditory evoked potential component N100 in schizophrenia - A critical review. Psychiatry Research 161 (2008) 259-274.

[147] Mulert,C., Seifert,C., Leicht,G., Kirsch,V., Ertl,M., Karch,S., Moosmann,M., Lutz,J., Moller,H.J., Hegerl,U., Pogarell,O., Jager,L., Single-trial coupling of EEG and fMRI reveals the involvement of early anterior cingulate cortex activation in effortful decision making. Neuroimage 42 (2008) 158-168.

[148] Crowley,K.E., Colrain,I.M., A review of the evidence for P2 being an independent component process: age, sleep and modality. Clinical Neurophysiology 115 (2004) 732-744.

[149] Acharya,R., Faust,O., Kannathal,N., Chua,T., Laxminarayan,S., Non-linear analysis of EEG signals at various sleep stages. Computer Methods and Programs in Biomedicine 80 (2005) 37-45.

[150] Ruby,P., Caclin,A., Boulet,S., Delpuech,C., Morlet,D., Odd sound processing in the sleeping brain. Journal of Cognitive Neuroscience 20 (2008) 296-311.

[151] Mander,B.A., Reid,K.J., Davuluri,V.K., Small,D.M., Parrish,T.B., Mesulam,M.M., Zee,P.C., Gitelman,D.R., Sleep deprivation alters functioning within the neural network underlying the covert orienting of attention. Brain Research 1217 (2008) 148-156.

[152] Benar,C.G., Schon,D., Grimault,S., Nazarian,B., Burle,B., Roth,M., Badier,J.M., Marquis,P., Liegeois-Chauvel,C., Anton,J.L., Single-trial analysis of oddball event-related potentials in simultaneous EEG-fMRI. Human Brain Mapping 28 (2007) 602-613.

[153] Debener,S., Ullsperger,M., Siegel,M., Fiehler,K., von Cramon,D.Y., Engel,A.K., Trial-by-trial coupling of concurrent electroencephalogram and functional magnetic resonance imaging identifies the dynamics of performance monitoring. Journal of Neuroscience 25 (2005) 11730-11737.

[154] Iyer,D., Zouridakis,G., Single-trial evoked potential estimation: Comparison between independent component analysis and wavelet denoising. Clinical Neurophysiology 118 (2007) 495-504.

[155] Bagshaw,A.P., Warbrick,T., Single trial variability of EEG and fMRI responses to visual stimuli. Neuroimage 38 (2007) 280-292.

[156] Zouridakis,G., Iyer,D., Diaz,J., Patidar,U., Estimation of individual evoked potential components using iterative independent component analysis. Physics in Medicine and Biology 52 (2007) 5353-5368.

[157] Mantini,D., Corbetta,M., Perrucci,M.G., Romani,G.L., Del Gratta,C., Large-scale brain networks account for sustained and transient activity during target detection. Neuroimage 44 (2009) 265-274.

[158] Mutihac,R., Mutihac,R.C., A comparative study of independent component analysis algorithms for electroencephalography. Romanian Reports in Physics 59 (2007) 831-860.

[159] Zbilut,J.P., Webber,C.L., Embeddings and Delays As Derived from Quantification of Recurrence Plots. Physics Letters A 171 (1992) 199-203.

[160] Marwan,N., Encounters With Neighbours-Current Development of Concepts Based on Recurrence Plots And Their Application. In: Fakuktät Mathematik Und Naturwissenschaften Universität Potsdam, (2003).

[161] Carrubba,S., Frilot,C., Chesson,A.L., Marino,A.A., Nonlinear EEG activation evoked by low-strength low-frequency magnetic fields. Neuroscience Letters 417 (2007) 212-216.

[162] Carrubba,S., Frilot,C., Chesson,A.L., Marino,A.A., Evidence of a nonlinear human magnetic sense. Neuroscience 144 (2007) 356-367.

[163] Carrubba,S., Frilot,C., Chesson,A.L., Webber,C.L., Zbilut,J.P., Marino,A.A., Magnetosensory evoked potentials: Consistent nonlinear phenomena. Neuroscience Research 60 (2008) 95-105.

[164] Schinkel,S., Marwan,N., Kurths,J., Brain signal analysis based on recurrences. Journal of Physiology (Paris) 103 (2009) 315-323.

[165] Marwan,N., Meinke,A., Extended recurrence plot analysis and its application to ERP data. International Journal of Bifurcation and Chaos 14 (2004) 761-771.

[166] Zenker,F., Barajas,J.J., Auditory P300 development from an active, passive and single-tone paradigms. International Journal of Psychophysiology 33 (1999) 99-111.

[167] Lindin,M., Zurron,M., Diaz,F., Changes in P300 amplitude during an active standard auditory oddball task. Biological Psychology 66 (2004) 153-167.

[168] Barry,R.J., Rushby,J.A., Smith,J.L., Clarke,A.R., Croft,R.J., Wallace,M.J., Brain dynamics in the active vs. passive auditory oddball task: Exploration of narrow-band EEG phase effects. Clinical Neurophysiology 118 (2007) 2234-2247.

[169] Polich,J., Attention, Probability, and Task Demands As Determinants of P300 Latency from Auditory-Stimuli. Electroencephalography and Clinical Neurophysiology 63 (1986) 251-259.

[170] Stevens,M.C., Laurens,K.R., Liddle,P.F., Kiehl,K.A., The hemodynamics of oddball processing during single-tone and two-tone target detection tasks. International Journal of Psychophysiology 60 (2006) 292-303.

[171] Takens,F., Detecting Strange Attractors in Turbulence. In: D.A.Rand, L.S.Young (Eds.), Lectures Notes in Mathematics, Vol. 898, Springer, Berlin, (1981) 366-381.

[172] Eckmann,J.P., Oliffson Kamphorst,S. and Ruelle,D., Recurrence Plots of Dynamical Systems. In: (1987), 973-977.

[173] Marwan,N., Romano,M.C., Thiel,M., Kurths,J., Recurrence plots for the analysis of complex systems. Physics Reports-Review Section of Physics Letters 438 (2007) 237-329.

[174] Marwan,N., Wessel,N., Meyerfeldt,U., Schirdewan,A., Kurths,J., Recurrence-plot-based measures of complexity and their application to heart-rate-variability data. Physical Review e 66 (2002) e026702.

[175] Kennel,M.B., Brown,R., Abarbanel,H.D.I., Determining Embedding Dimension for Phase-Space Reconstruction Using A Geometrical Construction. Physical Review A 45 (1992) 3403-3411.

[176] Fraser,A.M., Swinney,H.L., Independent Coordinates for Strange Attractors from Mutual Information. Physical Review A 33 (1986) 1134-1140.

[177] Demiralp,T., Ademoglu,A., Schurmann,M., Basar-Eroglu,C., Basar,E., Detection of P300 waves in single trials by the wavelet transform (WT). Brain and Language 66 (1999) 108-128.

[178] Schinkel,S., Marwan,N., Kurths,J., Order patterns recurrence plots in the analysis of ERP data. Cognitive Neurodynamics 1 (2007) 317-325.

[179] Marwan,N., Groth,A., Kurths,J., Quantification of Order Patterns Recurrence Plots of Event Related Potentials. Chaos and Complexity Letters 2 (2007) 301-314.

[180] Bennington,J.Y., Polich,J., Comparison of P300 from passive and active tasks for auditory and visual stimuli. International Journal of Psychophysiology 34 (1999) 171-177.

[181] Horovitz,S.G., Skudlarski,P., Gore,J.C., Correlations and dissociations between BOLD signal and P300 amplitude in an auditory oddball task: a parametric approach to combining fMRI and ERP. Magnetic Resonance Imaging 20 (2002) 319-325.

[182] Hirata,K., Lehmann,D., N1 and P2 of Frequent and Rate Event-Related Potentials Show Effects and After-Effects of the Attended Target in the Oddball-Paradigm. International Journal of Psychophysiology 9 (1990) 293-301.

[183] Starr,A., Aguinaldo,T., Roe,M., Michalewski,H.J., Sequential changes of auditory processing during target detection: Motor responding versus mental counting. Electromyography and Motor Control-Electroencephalography and Clinical Neurophysiology 105 (1997) 201-212.

[184] Iwanski,J.S., Bradley,E., Recurrence plots of experimental data: To embed or not to embed? Chaos 8 (1998) 861-871.

[185] Eguiluz,V.M., Chialvo,D.R., Cecchi,G.A., Baliki,M., Apkarian,A.V., Scale-free brain functional networks. Physical Review Letters 94 (2005).

[186] Friston,K.J., The labile brain. I. Neuronal transients and nonlinear coupling. Philosophical Transactions of the Royal Society B-Biological Sciences 355 (2000) 215-236.

[187] Rulkov,N.F., Sushchik,M.M., Tsimring,L.S., Abarbanel,H.D.I., Generalized Synchronization of Chaos in Directionally Coupled Chaotic Systems. Physical Review e 51 (1995) 980-994.

[188] Romano,M.C., Thiel,M., Kurths,J., von Bloh,W., Multivariate recurrence plots. Physics Letters A 330 (2004) 214-223.

ACKNOWLEDGEMENTS

I thank Prof. Stephan Paul for accepting me as a PhD student, for being kind, open and interested in my work.

I thank also Prof. J. Leo van Hemmen and Prof. Sibylle Ziegler, for being part of my examiner committee.

I consider myself lucky to always find the best people to work with/for, and this applies to the entire neuroimaging group.

I would like to particularly thank Michael Czisch, for being a superb advisor and knowing when to criticize and when to push me, for giving me the space and time to walk on my own feet, for supporting me and sometimes even believing in me more than myself. I am extremely grateful and I will always be.

Philipp Sämann for always knowing how the stretch my limits, for everything I learned and for giving your best to improve any work on the group.

Renate Wehrle, I thank you not just for all scientific advice and what I have learned from you but also for being so kind and friendly since the first day I arrived in Germany, for the care and help that I needed to feel more at home.

Victor Spoormaker, you are particularly gifted and add a lot to the group. I learned a lot with you and I thank you for that. Thank you also for your friendship, availability and support.

For the friendship, help, advice and making my stay here much more pleasant, I thank Sara Kiem, Roberto Goya-Maldonado and Barbara Grünecker.

For the “animals”, “zombies fans” and “memory gifted”, Sebastian Kaltwasser, Benedikt Bedenk, Martin Dresler and Boris-Nikolai Konrad, I thank you for making life even more interesting.

It has been also a pleasure to work with competent and welcoming technicians and technical assistants Rosa Schirmer, Reinhold Borschke, Elke Schreiter, Armin Mann, Stephanie Alam and Ines Eidner. Thank you for this background support.

I thank the director of the MPI, Prof. Florian Holsboer, for the opportunity to work in a so rich environment, with amazing researchers and structural facilities.

As important as the co-workers, my family was primordial in all my steps here and will always be in any step I will still give in my life.

To my mom, Maria Auxiliadora, for being so perfect and taking such good care of me, even from so far away. Thank you for calling me almost every day just to say good night and making sure I was fine. Thank you for being unconditionally by my side.

To my sisters, Fábia and Cybelle, who I miss a lot, thank you for cheering me up and always being there for me. I cannot forget to thank Bartolomeu Silva for making me laugh, for your friendship and being an excellent host.

To my father, J.M Andrade thank for the support and care.

I am especially grateful to my partner and friend, Danusa Colares, for delaying and leaving many things of your life to be here with me. It was really hard but you gave me strength and went through with me anyway. I love everything you are and everything you make me be. Thank you for being part of my life since I was twelve.

CONTRIBUTIONS

1. *Recurrence quantification analysis allows for single-trial stimulus differentiation in evoked potential studies.*

Andrade KC, Wehrle R, Spoormaker, VI, SämannPG, Czisch M.

Clinical Neurophysiology (under revision).

2. *Sleep spindles and hippocampal functional connectivity in human NREM sleep.*

Andrade KC, Spoormaker VI, Dresler M, Wehrle R, Holsboer F, Sämann PG, Czisch M.

The Journal of Neuroscience (under revision).

3. *The neural correlates of negative prediction error signaling in human fear conditioning.*

Spoormaker VI, Andrade KC, Schröter MS, Sturm A, Goya-Maldonado R, Sämann PG, Czisch M.

Neuroimage, 54(3):2250-6 (2011)

4. *The neural correlates and temporal sequence of the relationship between shock exposure, disturbed sleep and impaired consolidation of fear extinction.*

Spoormaker VI, Sturm A, Andrade KC, Schröter MS, Goya-Maldonado R, Holsboer F, Wetter TC, Sämann PG, Czisch M.

Journal of Psychiatric Research, 44(16):1121-8 (2010)

5. *Development of a Large-Scale Functional Brain Network during Human Non-Rapid Eye Movement Sleep.*

Spoormaker VI, Schroter MS, Gleiser PM, Andrade KC, Dresler M, Wehrle R, Sämann PG, Czisch M.

The Journal of Neuroscience, 30(34):11379-87 (2010)

6. *Acoustic oddball during NREM sleep: a combined EEG/fMRI study.*

Czisch M, Wehrle R, Stiegler A, Peters H, Andrade KC, Holsboer F, Sämann PG.

PLoS One 4(8):e6749 (2009)